University of Alberta

CMOS OPTICAL MICRO-RADIATOR VACUUM SENSOR

By

Yuan Ma ©

A thesis submitted to the Faculty of Graduate Studies and Research in partial fulfillment of the requirements for the degree of Doctor of Philosophy

Department of Electrical and Computer Engineering

Edmonton, Alberta

Fall 2002

National Library
of Canada

Acquisitions and
Bibliographic Services

395 Wellington Street
Ottawa ON K1A 0N4
Canada

Bibliothèque nationale
du Canada

Acquisitions et
services bibliographiques

395, rue Wellington
Ottawa ON K1A 0N4
Canada

Your file Votre référence

Our file Notre référence

The author has granted a non-exclusive licence allowing the National Library of Canada to reproduce, loan, distribute or sell copies of this thesis in microform, paper or electronic formats.

L'auteur a accordé une licence non exclusive permettant à la Bibliothèque nationale du Canada de reproduire, prêter, distribuer ou vendre des copies de cette thèse sous la forme de microfiche/film, de reproduction sur papier ou sur format électronique.

The author retains ownership of the copyright in this thesis. Neither the thesis nor substantial extracts from it may be printed or otherwise reproduced without the author's permission.

L'auteur conserve la propriété du droit d'auteur qui protège cette thèse. Ni la thèse ni des extraits substantiels de celle-ci ne doivent être imprimés ou autrement reproduits sans son autorisation.

0-612-81230-8

Canada

University of Alberta

Library Release Form

Name of Author: Yuan Ma

Title of Thesis: CMOS Optical Micro-Radiator Vacuum Sensor

Degree: Doctor of Philosophy

Year this Degree Granted: 2002

Permission is hereby granted to the University of Alberta Library to reproduce single copies of this thesis and to lend or sell such copies for private, scholarly or scientific research purposes only.

The author reserves all other publication and other rights in association with the copyright in the thesis, and except as herein before provided, neither the thesis nor any substantial portion thereof may be printed or otherwise reproduced in any material from whatever without the author's prior written permission.

Yuan Ma

40 Greatwood Cr.
Nepean, ON
Canada K2G 6T7

Date: 13 May, 2002

University of Alberta

Faculty of Graduate Studies and Research

The undersigned certify that they have read, and recommend to the Faculty of Graduate Studies and Research for acceptance, a thesis entitled *CMOS Optical Micro-Radiator Vacuum Sensor* submitted by *Yuan Ma* in partial fulfillment of the requirements for the degree of Doctor of Philosophy.

A. M. Robinson
Dr. A. M. Robinson

Ronald PW Law
Dr. R. P. W. Lawson

M Brett
Dr. M. Brett

Dr. C. Backhouse

Dr. F. Hegmann

T.H. (HJTT.)
Dr. T. Hubbard
Dalhousie University

Date: 13 May 2002

ABSTRACT

The purpose of this project is to develop a high sensitivity vacuum gas sensor using Complementary Metal Oxide Silicon (CMOS) micromachining technology.

A CMOS optical micro-radiator vacuum sensor has been designed, tested and calibrated. The package is comprised of a micromachined radiator and a photodetector. The measurement technique for this device involves an automated system.

MEMS technology helps to lower the power consumption of the device and minimizes the characteristic dimension of the system. Monitoring the radiation improves the sensitivity of measurement by several orders of magnitude compared to the conventional technique of measuring the resistance variation. A power-switching scheme has been introduced to increase the pressure measurement range and extend the lifetime of the device.

A three-mode CMOS photodetector has been designed and tested for the purpose of integration of the system. Output of the photodetector is proportional to the sensitive area of the device and varies linearly with the intensity of incident light.

An automated system has been demonstrated for pressure sensing with constant photodetector output. Calibration of the system has been performed by comparison with secondary standards. Experimental results showed a measurement range from 10^{-3} Pa to 10^{5} Pa and relative error is less than 8% compared with secondary standards.

Analytical and numerical modeling packages have been used to obtain the photodetector response with the pressure variation and temperature distribution of the device. Simulation results demonstrated a good agreement with experimental data.

ACKNOWLEDGEMENTS

I would like to express my sincere gratitude to my supervisors, Dr. A. M. Robinson and Dr. R. P. W. Lawson, for their continuous guidance, encouragement and patience throughout this research work, without whom this thesis would not be possible. Special appreciation should be extended to Dr. W. Allegretto, Dr. F. Vermeulen, Dr. M. Brett, Dr. C. Backhouse and Dr. F. Hegmann, for their enlightening discussions and help in various areas.

I gratefully acknowledge the assistance from R. Schmaus, G. Braybrook, S. Kennedy and K. Lui. K. Brown, D. Lu, S. Esteves, and M. Hu provided tremendous help, which is greatly appreciated.

I thank my husband Qiang for his understanding and support, my daughter Annie for bringing happiness into difficult times. Finally, my heartfelt gratitude goes to my parents. This thesis is dedicated to them.

CONTENTS

1 Introduction **1**

1.1 CMOS micromachining 1

1.2 Thermal conductivity gauge 2

1.3 Thermal radiation 5

1.4 Thesis overview 9

References 10

2 CMOS Micromachining and MEMS Design Packages **12**

2.1 A typical CMOS micromachining process 12

2.2 MEMS design packages 15

2.2.1 Mentor Graphics MEMS design kit 16

2.2.2 Cadence IC layout editor and Multi-User MEMS Processes (MUMPS) design kit for Cadence 17

2.2.3 MEMSCAP® MEMS Pro 17

References 19

3 CMOS Optical Micro-Radiator **21**

3.1 CMOS optical micro-radiator 21

3.2 Micro-radiator electro-thermal model 24

3.2.1 Conduction heat loss through the gas and through the supports 26

3.2.2 Convection heat loss 29

3.2.3 Radiation heat loss 30

3.2.4 Total heat loss 30

3.2.5 Thermal conductivity gauge useful range 33

References 35

4 Experiment Configuration and Measurement Sensitivity 37

4.1 Variable pressure chamber 37

4.2 Photodiode and point source of light 39

4.3 Digital constant power supply unit and data acquisition unit 44

4.3.1 Test of constant power supply unit 47

4.3.2 Test of experiment control unit 51

4.4 Measurement sensitivity 53

References 58

5 Device Characterization 59

5.1 Micro-radiator radiation measurement 59

5.1.1 Micro-radiator radiation response with input power 59

5.1.2 Micro-radiator radiation spectral analysis 61

5.1.3 Micro-radiator radiation spatial distribution 67

5.2 Reliability study of polysilicon 69

References 75

6 Vacuum Pressure Sensing and Power-Switching Scheme **76**

6.1 Micro-radiator radiation response with pressure 76

6.2 Power-Switching Scheme 81

6.3 Calibration by comparison 87

- 6.3.1 Calibration curves 87
- 6.3.2 System automation 89
- 6.3.3 Test results 91
- 6.3.4 Factors that affect the calibration 92

References 94

7 CMOS Photodetector Design **95**

7.1 P-N junction and photodiode 95

7.2 Phototransistor 100

7.3 Three-mode CMOS photodetector design 102

7.4 Test of three-mode CMOS photodetector 106

- 7.4.1 Test with a point light source 106
- 7.4.2 Test with a laser diode 106
- 7.5.3 Test with a micro-radiator 110

7.5 Noise in CMOS photodetector 112

7.6 Integration of the micro-radiator and photodetector 112

References 115

8 Numerical Modeling **116**

8.1 Model building 117

8.2 Temperature distribution analysis 118

8.3 Radiation calculation 123

References 124

9 Conclusions and Future Work **125**

9.1 Conclusions 125

9.2 Future work 126

9.2.1 Micro-radiator matrix design 126

9.2.2 Variation of the characteristic dimension of the system 127

9.2.3 Integration of the system 128

9.2.4 Gas analysis using micro-radiator pressure sensing system 128

References 128

Appendix A Micro-radiator electro-thermal model analysis **129**

Appendix B Experiment control system **131**

B.1 User interface 131

B.2 Experiment control system flow chart 133

B.3 Experiment control system program 135

Appendix C Automated pressure measurement system program **147**

Appendix D ANSYS input file **149**

List of Tables

5.1 Optical filters and lock-in amplifier output 63

6.1 J-K flip-flop truth table 82

6.2 Parameter table for Figure 6.4 83

6.3 Typical measurement results using calibration curve obtained from same device 91

7.1 Function table of three-mode photodetector 105

8.1 Tables of thermo-physical properties 118

List of Figures

1.1 Heat transfer regimes in a thermal conductivity gauge 3

1.2 Spectrum of electromagnetic radiation 7

1.3 Spectral blackbody emissive power 8

2.1 Cross-section of a wafer of a typical CMOS micromachining fabrication 13

2.2 Cross-section of a typical MEMS structure released with XeF_2 15

2.3 L-Edit user interface with a polysilicon resistor layout as an example 18

3.1 SEM picture of a serpentine-shaped polysilicon micro-radiator 22

3.2 Micro-radiator layout (A) and cross-sectional diagram (B) 24

3.3 Heat transfer related to the micro-radiator 25

3.4 A simplified micro-radiator structure 26

3.5 Average temperature of the micro-radiator versus the surrounding gas pressure operating at a power of 10 mW 32

3.6 Temperature variation of a typical thermal-conductivity gauge operating at constant power inputs of 10 mW and 50 mW 34

4.1 Experiment setup 38

4.2 Response data for silicon photodiode 13 DAS 011/C 39

4.3 Spherical wavefronts produced by a point source of light at O 41

4.4 Schematic of point source of light 42

4.5 Photodetector signal versus inverse distance squared of the light source 43

4.6 Variation of photodetector signal versus time operating with constant current at atmospheric pressure 45

4.7 Variation of photodetector signal versus time operating with constant voltage at atmospheric pressure 45

4.8 Photodetector signal (bottom) showing the radiation follows in a non-linear fashion the variation of the power supplied to the micro-radiator (top) 46

4.9 (a) Test of digital constant power supply unit with step function power output 49

4.9 (b) Test of digital constant power supply unit showing the "homing-in" procedure of the system 49

4.10 Test of constant power system operating at different powers 50

4.11 Magnified part of Figure 4.8 showing the details of photodetector and power signal 52

4.12 Extrapolated response of silicon photodetector 13 DAS 011/C 54

4.13 Comparison of the photodetector output with the total radiation and resistance of the micro-radiator as a function of temperature 55

4.14 Micro-radiator temperature and photodetector output versus pressure operating at input powers of 10 and 50 mW 57

5.1 Experiment setup for radiation measurement 60

5.2 Photodetector signal versus the micro-radiator input power ($\theta = 0$) 61

5.3 Apparatus used for radiation spectral analysis 62

5.4 Normalized spectral distribution of a micro-radiator with 50 mW input power. The points are measured values 64

5.5 Spectral emissive power analysis experiment setup 66

5.6 Spectral emissive power of the micro-radiator from 650 nm to 1200 nm 67

5.7 Normalized angular radiant intensity of a micro-radiator as a function of the incidence angle θ 68

5.8 (a) Voltage-current characteristics of micro-radiator for a current from 0 to 2 mA 69

5.8 (b) Voltage-current characteristics of micro-radiator for a current from 0 to 3 mA 70

5.9 (a) Resistance of micro-radiator as a function of input current from sweep 1,4,6 and 10 of Figure 5.8 (b) 73

5.9 (b) Resistance of micro-radiator as a function of power input 73

5.9 (c) Temperature versus input power curves for the first and last sweep 74

6.1 Photodetector signal versus pressure under a constant power of 10 mW 78

6.2 Analytical simulation compared with experimental results 79

6.3 Analytical simulation and experimental results showing photodetector signal versus pressure operating at constant powers of 10 and 20 mW 80

6.4 Photodetector signal versus pressure operating at different constant powers showing power-switching scheme 84

6.5 Conceptual diagram of power switching scheme 85

6.6 Relationship between parameter k and the applied power 85

6.7 Relationship between parameter B and the applied power 86

6.8 Power consumption of the micro-radiator versus the pressure with constant photodetector output of 1 and 3 μA 86

6.9 (a) A typical calibration curve with data below 33.5 mW being fitted onto a polynomial curve 88

6.9 (b) A typical calibration curve with data above 33.5 mW being fitted onto a polynomial curve 88

6.10 Flow-chart of the pressure measurement system 90

6.11 Photodetector signal versus pressure with different distance between micro-radiator and photodetector 92

6.12 Photodetector outputs for air and He 94

7.1 (a) An idealized model of the p-n junction without bias showing the neutral and depletion areas 97

7.1 (b) A schematic showing various current and particle flow components in the P-N diode at equilibrium 97

7.2 (a) Optical generation of carriers in a P-N junction 99

7.2 (b) P-N junction symbol 99

7.2 (c) I-V characteristics of an illuminated junction 99

7.3 Schematic of an n-p-n transistor showing hole and electron flow 101

7.4 Structure and equivalent circuits of the CMOS multi-mode photodetector 103

7.5 Structure and equivalent circuit of the three-mode photodetector 104

7.6 (a) Output of photodetector working in photodiode mode versus inverse distance squared of the light source 107

7.6 (b) Output of photodetector working in phototransistor mode versus inverse distance squared of the light source 107

7.7 Measured response of the CMOS photodetector operating in different modes 109

7.8 Comparison of CMOS photodetector output with two different sensitive areas in the ratio of 8.7:1 109

7.9 Output of CMOS photodetector working in phototransistor mode versus power input of micro-radiator 111

7.10 Output of CMOS photodetector working in phototransistor mode versus pressure 111

7.11 Integration of the photodetector and micro-radiator with flip-chip technique 113

7.12 The joined micro-radiator / photodetector pair is die-attached and wire-bonded to a DIP 114

7.13 Assembling of the photodetector and micro-radiator with two DIPs 115

8.1 Micro-radiator model built in ANSYS 117

8.2 Temperature distributions operating at a power of 15 mW at 10^{-3} Pa simulated with Allegretto's package 119

8.3 Temperature distributions operating at a power of 15 mW at 10^{-3} Pa simulated with ANSYS 119

8.4 Temperature distributions operating at a power of 15 mW at 10^{5} Pa simulated with Allegretto's package 121

8.5 Temperature distributions operating at a power of 15 mW at 10^{5} Pa simulated with ANSYS 121

8.6 Picture of burnt out micro-radiator showing the hottest point at the center of the platform at 10^{5} Pa 122

8.7 Picture of micro-radiator at 10^{-3} Pa showing the hottest point at two corners of the platform without supporting arms 122

8.8 Allegretto's simulated photodetector output compared with experimental data 123

9.1 Micro-radiator matrix (2^n x 2^m) design 127

B.1 Constant power supply unit user interface 132

B.2 Simplified flow-chart of the digital constant power supply unit and data acquisition unit 134

List of Symbols

α	accommodation coefficient
α_T, β_T	temperature coefficients of resistance
β	coefficient of thermal expansion
γ	ratio of specific heats C_p / C_v
ε	emissivity
η	coefficient to account for first order approximation
η_s	coefficient to account for the number of micro-radiator supports
θ	incident angle of light
κ	proportional constant to account for the photodetector-radiator geometry
λ	optical wavelength
λ_{mfp}	mean free path
μ	dynamic viscosity
ν	kinematic viscosity
ρ	mass density
σ	Stefan-Boltzmann constant
τ	time constant
ϕ	azimuth angle
χ	thermal diffusivity
a	molecular diameter
A	diode cross-sectional area
A_s	cross-section area of micro-radiator support
c_0	speed of light in vacuum
C_p	specific heat at constant pressure
C_v	specific heat at constant volume
d	characteristic dimension of micro-radiator
d_c	critical dimension defined as the ratio of surface area to perimeter
D	chamber diameter
e	length of micro-radiator support
E_b	emissive power of a blackbody
$E_{\lambda,b}$	spectral distribution of blackbody emission
g	acceleration of gravity
g_{op}	excess carrier generation rate in a photodiode
Gr	Grashof number
h	Planck constant
$h(\nu,p)$	convective heat-transfer coefficient
H	heat flow
I_0	constant current
I_d	photodetector output
I_{op}	photocurrent
J	light intensity
k	thermal conductivity
K	free molecule conductivity

k_0	Boltzmann constant
Kn	Knudsen's number
k_s	thermal conductivity of the support arm material
L_n	diffusion length of electron
L_p	diffusion length of hole
m	mass of gas molecule
p	pressure
P	power
Pr	Prandtl number
$\dot{Q}$	total heat loss
r, r'	radius of spherical wavefronts
R	resistance
R_0	room temperature resistance
Ra	Rayleigh number
s	distance from micro-radiator to silicon substrate
t	time
T	absolute temperature
T_0	room temperature
T_g	average temperature of the gas far from the micro-radiator
T_g'	average temperature of gas molecule arrival at the micro-radiator
T'	average temperature of gas molecule departure from the micro-radiator
T_s	temperature of silicon substrate
V_0	constant voltage
W	input power
W_{cm}	conduction heat loss through the gas
W_{cs}	conduction heat loss through the supports
W_r	radiation heat loss
W_v	convection heat loss
x, y	micro-radiator dimension

Chapter 1

Introduction

Micro-fabrication technologies are shrinking devices into micro- and nanometer scales [1-2]. Many interesting and potentially useful micro-electro-mechanical sensors and actuators have been produced by these technologies. Pressure sensors have been predicted to capture the lion's share of the micro-system market for some time [3-4]. In this project, a highly sensitive optical radiator vacuum sensor system has been designed, fabricated with Complementary Metal Oxide Silicon (CMOS) micromachining technology, and tested. Micromachining technology helps to lower the power consumption of the sensor to the 10 mW range. With a power-switching scheme introduced in this thesis, the optical sensor system is capable of measuring pressure from 10^5 Pa down to 10^{-3} Pa, with a sensitivity several orders of magnitude better than conventional Pirani type vacuum gauges. Background information related to this project includes CMOS micromachining, thermal conductivity pressure gauges and thermal radiation. A brief introduction on each part is given in this chapter. An overview of the whole thesis is given at the end of this chapter.

1.1 CMOS micromachining

Micromachining is also called MicroElectroMechanical Systems (MEMS) in North America and Micro-Systems Technology (MST) in Europe. MEMS refers to the micro-devices or systems that combine mechanical, electrical, magnetic, thermal and other physical phenomena to form precision systems. These systems can sense, control, and actuate on the micro-scale, and function individually or in arrays to generate effects on the macro-scale. Most micromachining fabrication technologies are borrowed from the microelectronics industry. The microelectronics fabrication process has the potential of producing large quantity micromachined systems at low cost. Post-processing steps of selective etching of silicon are added after the fabrication process in order to release microstructures, making them freestanding.

Over the past decades, CMOS integrated circuits have become a mainstream technology for VLSI system design. Parameswaran initiated CMOS micromachining in 1989 by implementing unconventional layout designs in standard CMOS Integrated Circuit (CMOSIC) technology without altering the process sequence [5]. A single post-processing etching step was introduced to release microstructures on a CMOS IC without affecting the circuitry formed on the chip. Compared to the other non-standard microfabrication methods, CMOS micromachining has the advantages of a high degree of reliability and repeatability because of well-defined CMOS IC process parameters.

Standard CMOS IC processes can be accessed by universities through the Canadian Microelectronics Corporation (CMC) in Canada, which provides a fruitful environment for CMOS micromachining research and development.

1.2 Thermal conductivity gauge

The thermal conductivity k of a substance is defined by

$$k = -H \Big/ \frac{dT}{ds} \tag{1.1}$$

in which H is the amount of heat flowing per unit area per second in the direction parallel to s, and dT / ds is the temperature gradient in this direction [6].

The thermal conductivity gauge is one of the most commonly used vacuum pressure gauges. The gauge depends on the loss of heat from a hot wire to its surroundings. The hot wire in a gaseous environment loses heat in four ways: (1) radiation, (2) conduction to supports, (3) conduction to the gas, and (4) convection.

The heat transfer regimes in a thermal conductivity gauge are illustrated in Figure 1.1 [7]. *Kn* is Knudsen's number, defined as the ratio of the mean free path λ_{mfp} of the gas molecules to the characteristic dimension *d* of the system, which is defined as the diameter of the hot wire here. The mean free path λ_{mfp} of the gas molecules is defined as the mean distance traveled by a gas molecule between collisions. In terms of the pressure p, λ_{mfp} can be expressed by [6]:

$$\lambda_{mfp} = \frac{k_0 T}{\sqrt{2}\pi a^2 p} \tag{1.2}$$

where $k_0 = 1.3805 \times 10^{-23}$ J/K is the Boltzmann constant, T is the absolute temperature, and a is the molecular diameter.

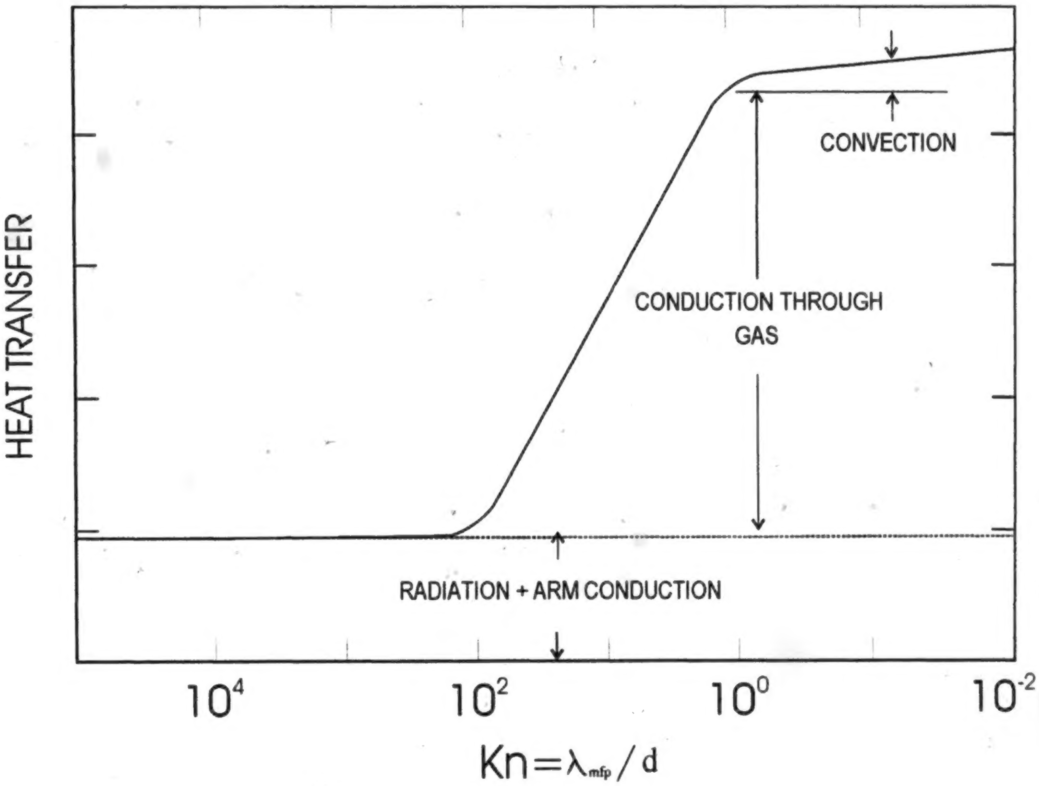

Figure 1.1 Heat transfer regimes in a thermal conductivity gauge

At high pressures where $Kn < 1$, the heat flow is independent of pressure except for a small convection effect. In the pressure range where $1 < Kn < 100$, the conduction heat loss from the hot filament to the molecules of surrounding gas dominates the heat transfer and is pressure dependent. It is this effect that is used to make a thermal-conductivity-based pressure gauge. In the lowest pressure region where $Kn > 10^2$, the heat flow is predominantly accounted for by radiation and conduction through the wire to the supports. If we assume the average temperature of the wire is kept constant at different pressures, radiation and conduction through the supports establish a constant background loss. The magnitude and stability of this background determine the lowest useful pressure of the gauge.

Two common types of thermal conductivity gauges are the thermocouple gauge and the Pirani gauge.

The thermocouple pressure gauge measures the temperature variation of a hot filament, as the pressure changes, by using a thermocouple. The Pirani gauge, on the other hand, measures the electrical resistance of the hot filament and calibrates this resistance change as a function of the gas pressure.

In recent years, some work has been reported on micromachined Pirani-type pressure sensors [8-10]. The principle of operation of these sensors is based on the resistance variation of a temperature-sensitive resistive element, e.g. polysilicon. As the pressure in the gauge tube increases, the thermal conduction of the gas surrounding the hot filament increases, and therefore the temperature of the filament tends to decrease. The electrical resistance of the filament varies with the temperature and is measured to reflect the pressure change. The resistance-temperature characteristics for a material at temperature T may be expressed by

$$R = R_0[1 + \alpha_T(T - T_0)] \tag{1.3}$$

where α_T is the temperature coefficient of resistance (TCR) and $\alpha_T \cong 1\times10^{-3}\ \mathrm{K}^{-1}$ for polysilicon. R_0 is the resistance at reference temperature T_0. The pressure measurement range of these sensors is from 10^{-1} Pa to 10^4 Pa [9].

In contrast to previous work, this project describes a micromachined thermal conductivity sensor based on the thermal radiation emitted from a thermally isolated polysilicon micro-radiator and the photodetector measurement. In the initial work done by Kleckner *et al.* [11], the authors claim that monitoring the radiation to measure gas pressure changes should be four times as sensitive as conventional Pirani gauge. In fact, the sensitivity of this method will be much better than that due to photodetector spectral response. This will be discussed in detail in Chapter 4.

1.3 Thermal radiation

Radiation is the emission of either particles or electromagnetic rays from a source [12]. It is usual to classify radiation according to its frequency or wavelength as a fundamental property. Figure 1.2 shows the spectrum of radiation from the highest energy cosmic ray particles (with shortest wavelength) down to the lowest energy radio waves (with longest wavelength).

The intermediate portion of the spectrum, which extends from approximately 10^{-7} m to 10^{-4} m, is termed thermal radiation and is pertinent to heat transfer. Thermal radiation includes a portion of the ultraviolet, all of the visible and the infrared. Visible radiation (normally called light) can be detected by the human eye, and has a wavelength from 400 nm to 700 nm.

When describing the radiation characteristics of real surfaces, it usually involves the concept of a blackbody. A blackbody is an ideal surface having the following properties [13]:

1. A blackbody absorbs all incident radiation, regardless of wavelength and direction.
2. For a prescribed temperature and wavelength, no surface can emit more energy than a blackbody.
3. Although the radiation emitted by a blackbody is a function of wavelength and temperature, it is independent of direction. This kind of emitter is usually called a diffuse emitter.

The spectral distribution of blackbody emission $E_{\lambda,b}$ refers to the power per unit area of the blackbody surface radiated in all directions per unit wavelength with units of W/(m^2-μm). It is a function of the absolute temperature and radiation wavelength of the blackbody. The emission $E_{\lambda,b}$ can be described by the Planck distribution [14]:

$$E_{\lambda,b}(\lambda,T) = \frac{2\pi h {c_0}^2}{\lambda^5 (e^{\frac{hc_0}{\lambda k_0 T}} - 1)} \tag{1.4}$$

where $h = 6.6256 \times 10^{-34}$ J·s and $k_0 = 1.3805 \times 10^{-23}$ J/K are the universal Planck and Boltzmann constants, respectively, $c_0 = 2.998 \times 10^8$ m/s is the speed of light in vacuum, T is the absolute temperature (K), and λ is the wavelength (μm). Planck distributions are plotted in Figure 1.3 for selected temperatures using MatLab.

The total emissive power of a blackbody, E_b, can be calculated by integrating equation (1.4) over the wavelength range from 0 to ∞. The result is called Stefan-Boltzmann law:

$$E_b = \sigma T^4 \tag{1.5}$$

in which σ is called the Stefan-Boltzmann constant, and has the numerical value

$$\sigma = 5.670 \times 10^{-8} W / m^2 \cdot K^4$$

Real surface emission differs from the Planck distribution. The ratio of the radiation emitted by a real surface to the radiation emitted by a blackbody at the same temperature is defined as the emissivity ε. Typical values of some commonly used materials can be found in engineering handbooks, e.g. CRC Handbook of Chemistry and Physics.

Usually the emissivity is a function of temperature and wavelength. However, the emissivity of silicon dioxide, the surface material of the micro-radiator studied in this project, is relatively constant with temperature and wavelength. Therefore, a constant value of 0.8 is used in this thesis for the simplicity of calculation [13].

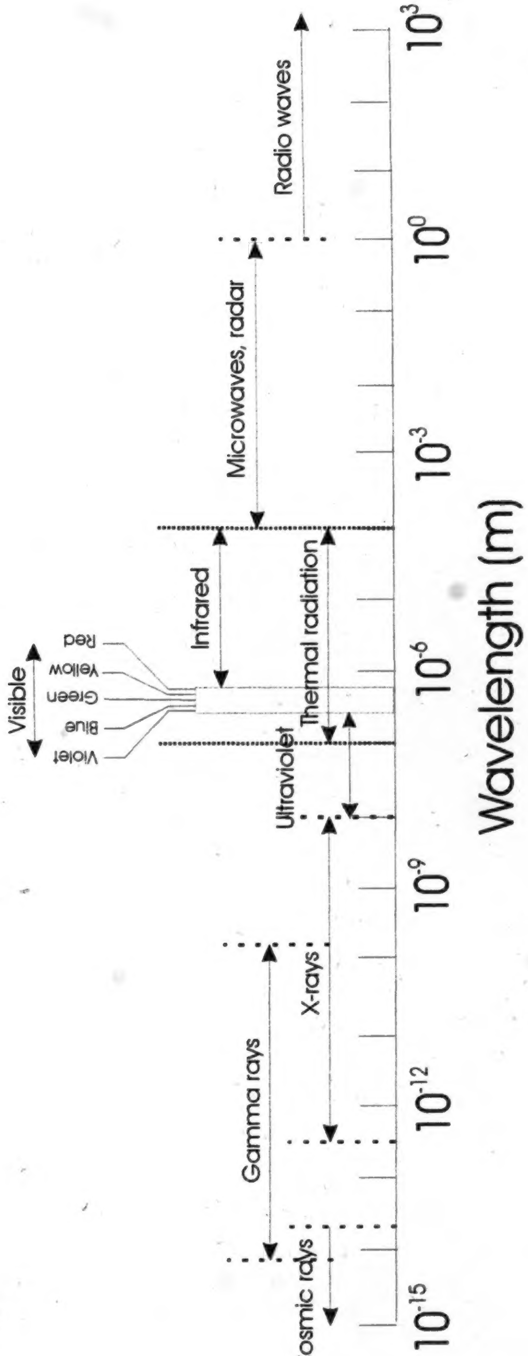

Figure 1.2 Spectrum of electromagnetic radiation

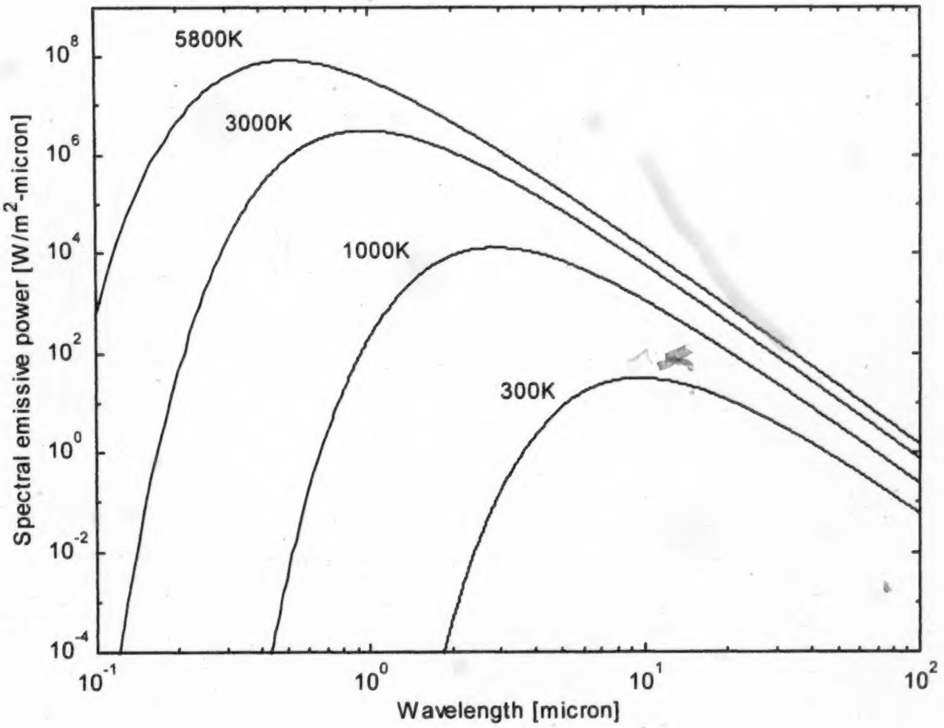

Figure 1.3 Spectral blackbody emissive power

1.4 Thesis overview

The purpose of this project is to develop a high sensitivity CMOS optical micro-radiator vacuum sensor with extended pressure measurement range.

MEMS design packages are introduced in Chapter 2. Several different design packages, including MEMS PRO V2.0™, Mentor Graphics and Cadence, are compared as the design tools for the MEMS devices.

The CMOS optical micro-radiator is introduced in Chapter 3. The post-processing technique for fabricated chips is provided. A micro-radiator electro-thermal model is discussed to illustrate the heat transfers of the system.

Chapter 4 describes the experimental configuration, which includes a digital constant power supply unit used to apply constant power to the micro-radiator regardless of the resistance variation and a data acquisition unit used to measure and record the magnitude of the radiation from the micro-radiator. Sensitivity of the radiation measurement is calculated in this chapter by considering the response of the photodetector at different micro-radiator temperatures when approximating the micro-radiator as a blackbody.

Device characterization is discussed in Chapter 5. This includes a micro-radiator radiation analysis and reliability study of polysilicon, which provides threshold conditions for operating the micro-radiator as a reliable pressure sensor.

The radiation from the micro-radiator is calibrated versus pressure in the range from 10^5 Pa down to 10^{-3} Pa in Chapter 6. A power-switching scheme used to increase the measurement sensitivity and lifetime of the device is also described. Automation of the measurement system with constant photodetector signal is introduced and realized in the chapter.

A three-mode CMOS photodetector design used for the integration of the system is introduced in Chapter 7. Fabricated photodetector design is calibrated at 670 nm in the power range from 0.01 mW to 10 mW.

Chapter 8 covers the numerical modeling of the device. Temperature distribution of the micro-radiator at 15 mW and photodetector output at different pressures at 10 mW is included. Simulation results are compared with experimental data.

Conclusions and future work are described in Chapter 9.

References:

[1] M. Gad-el-Hak (Editor), *The MEMS Handbook*, CRC Press, London, 2001.

[2] D. E. Koshland, "Engineering a small world, from atomic manipulation to microfabrication", Science, vol. 254, 1991, pp. 1300-1342.

[3] H. Kahn, M. de Boer, M. Judy, S. M. Spearing, "Materials Science of Microelectromechanical Systems (MEMS) Devices III", *MRS Symposium Proceedings*, vol. 657, Fall 2000.

[4] Sid Marshall, "Kona Conference raises four issues about commercialization of MEMS", SUSS report, Karl Suss America, Inc., Waterbury Center, VT 05677, USA, vol. 10, third/fourth quarter 1996, p. 4.

[5] M. Parameswaran, H. P. Baltes, Lj. Ristic, A. C. Dhaded and A. M. Robinson, "A new approach for the fabrication of micromechanical structures", *Sensors and Actuators*, 19, 1989, pp. 289-307.

[6] C. M. Van Atta, Vacuum Science and Engineering, McGraw-Hill Book Company, New York, 1965.

[7] J. F. O'Hanlon, *A User's Guide To Vacuum Technology, 2nd Edition*, John Wiley & Sons, Inc., New York, 1989.

[8] C. H. Mastrangelo and R. S. Muller, "Microfabricated thermal absolute-pressure sensor with on-chip digital front-end processor", *IEEE J. Solid-State Circuits*, Vol. 26, 1991, pp. 1998-2007.

[9] A. M. Robinson, P. Haswell, R. P. W. Lawson and M. Parameswaran, "A thermal conductivity microstructural pressure sensor fabricated in standard complementary metal-oxide semiconductor", *Rev. Sci. Instrum.*, Vol. 63, 1992, pp. 2026-2029.

[10] P. K. Weng and J. S. Shie, "Micro-Pirani vacuum gauge", *Rev. Sci. Instrum.*, Vol. 65, 1994, pp. 492-499.

5

[11] T. C. Kleckner, R. P. W. Lawson, and A. M. Robinson, "Constant power operation of incandescent micromachined polysilicon microresistors for use as vacuum pressure sensors", *J. Vac. Sci. Technol. A.*, Vol. 15(5), Sep/Oct 1997, pp. 2812-2815.

[12] J. W. Gardner, Microsensors – Principles and Applications, John Wiley & Sons, Inc., New York, 1995, p. 117.

[13] F. P. Incropera, D. P. DeWitt, *Introduction to Heat Transfer*, 3rd edition, John Wiley & Sons, Inc., New York, 1985, pp. 8-10.

[14] M. Planck, *The Theory of Heat Radiation*, Dover Publications, New York, 1959.

Chapter 2

CMOS Micromachining and MEMS Design Packages

CMOS micromachining is a combination of the standard CMOS process and silicon micromachining technology. First, the standard CMOS process is used to build a MEMS structure with electric circuitry on a silicon substrate. An opening is created on the substrate by making all the films absent in that region. Afterwards, isotropic or anisotropic etching is used to release the MEMS structure. In this chapter, a typical CMOS micromachining fabrication process is described to illustrate the general procedure of fabricating CMOS micromachined devices.

Since micromachining fabrication technologies are borrowed from the microelectronics industry, IC design packages are naturally used for MEMS design. In recent years, some design packages focusing on MEMS designing, e.g. MEMS Pro from MEMSCAP® Inc. (headquarters: St. Ismier, France and Oakland, CA, USA), have been developed. In this chapter, MEMS design strategies along with the MEMS design packages available to Canadian universities through the Canadian Microelectronics Corporation (CMC) are briefly introduced and compared on the basis of the criteria such as working environment, ease of use, etch simulation and design rule checking.

2.1 A typical CMOS micromachining process

Figure 2.1 shows a cross-section of a MEMS structure built with the Mitel 1.5 µm process and with all the layers present.

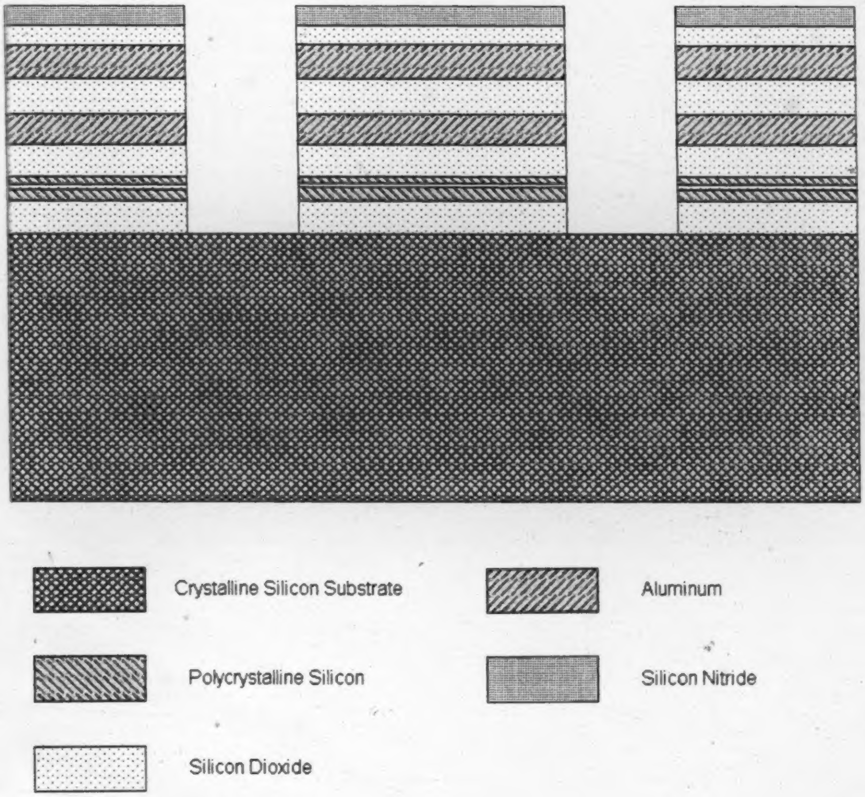

Figure 2.1 Cross-section of a wafer of a typical CMOS micromachining fabrication (not drawn to scale)

A typical Mitel 1.5 μm CMOS micromachining fabrication process may include the following steps.

- Highly conductive n+ doped layers are diffused over the n-type silicon wafer.
- A 0.9 μm field oxide layer may be used as a dielectric layer which electrically isolates the polysilicon structure from the crystalline substrate. It may also be used as structural material.
- After the field oxidation and gate oxidation (about 0.027 μm, not shown in Figure 2.1), two layers of low-stress, doped polysilicon are then deposited (about 0.32 μm and 0.25 μm thick, respectively) with a 0.02 μm oxide layer between. The polysilicon layers can also be used as electrically conductive layers.

- Then a 0.8 μm dielectric layer mainly composed of low-stress phosphosilicate glass (PSG) is deposited.
- Two 0.8 μm patterned aluminum layers are then used to form conducting layers and electrical interconnects. There is a 1.0 μm inter-dielectric oxide layer between two metal layers.
- Finally, two layers of passivation (0.5 μm oxide and 0.5 μm nitride) are deposited.

After the MEMS structures are fabricated, etching of the silicon substrate is used to release the structure from the substrate. There are two different types of etching: anisotropic and isotropic etching. Anisotropic etching is a process of preferential directional etching of material using liquid etchants like Ethylene Diamine Pyrocatechol (EDP) or Tetra Methyl Ammonium Hydroxide (TMAH). Isotropic etching refers to the etching of material regardless of crystallographic-orientation using an etchant such as Xenon difluoride.

Xenon difluoride has come into use as a replacement for anisotropic etchants EDP and TMAH recently [1-4] because of safety considerations. Xenon difluoride is a white solid at room temperature and pressure and sublimates at a pressure of about 500 Pa. Xenon difluoride vapor can etch silicon isotropically without external excitation and it has extremely high selectivity to many materials commonly used in MEMS.

The overall silicon/xenon difluoride reaction equation is given by:

$$2XeF_2 + Si \rightarrow 2Xe + SiF_4 \tag{2.1}$$

The reaction is exothermic and the main product SiF_4 is volatile at room temperature. It should be noted that moisture on the chip, which causes HF formation with exposure to XeF_2 gas, is a safety hazard to operating personnel and can also result in silicon dioxide etching.

Figure 2.2 is a schematic picture showing the CMOS micromachined structure in Figure 2.1 isotropically released from the substrate. The actual shape of the etched cavity and the roughness of the etched surfaces depend on the amount of undercutting, the ease of circulation of XeF_2, etc.

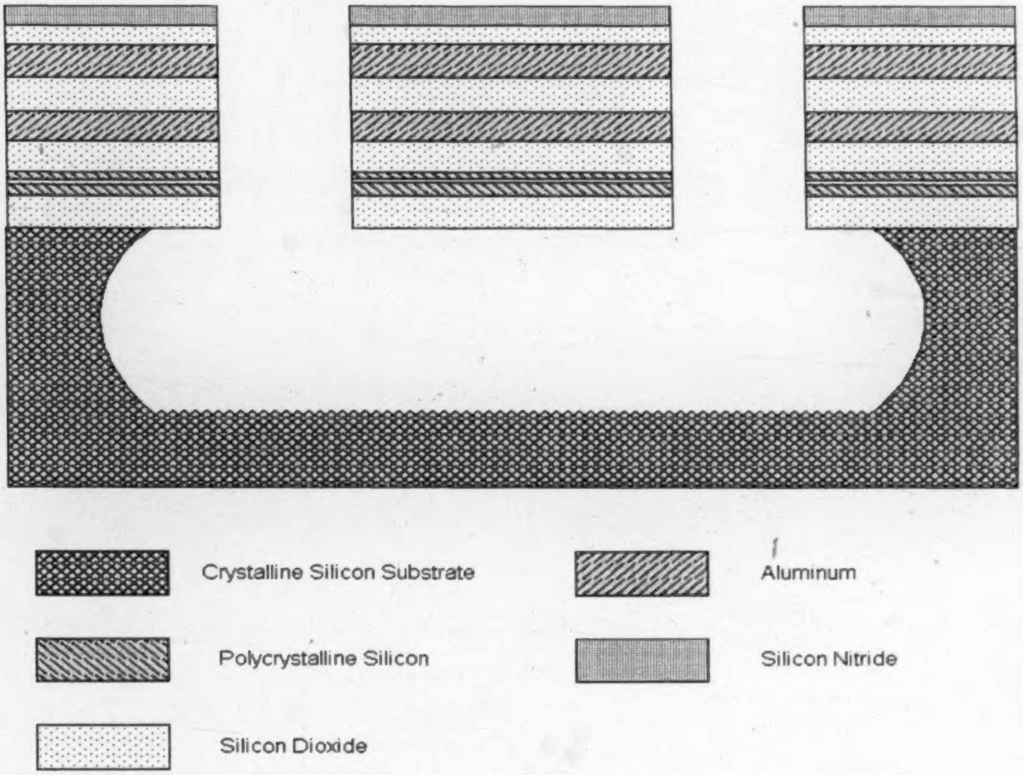

Figure 2.2 Cross-section of a typical MEMS structure released with XeF_2

2.2 MEMS design packages

There are two different MEMS design strategies: the system approach and the device approach. The system approach starts from a schematic, which uses symbols or hardware description language (HDL) models to build the system. The schematic is then simulated and mask layout is generated for fabrication. The device approach starts directly from a mask layout, which is a scaled layer-by-layer drawing of the MEMS structures. Different colors are used to represent different layers of the structure. Finite element analysis (FEA) software, such as ANSYS, can be used to simulate the device by transferring the mask information directly into the FEA software to build the model for simulation.

There is an increasing interest in hardware description languages recently because of the rapid increase in circuit complexities, an industry-wide desire for more formal (correct-by-design) engineering methods, and a general maturing of low-cost, more accessible HDL tools [5]. HDL models convert mechanical systems to equivalent electrical models. However, the HDL models are limited to systems that are simple enough to be described by closed-form equations. All the design related to this project used the device approach.

There are three software packages currently used in the universities for IC and MEMS design: Cadence, Mentor Graphics and MEMS Pro. The advantages and disadvantages of each of the software packages are discussed below from the design experience of the author.

2.2.1 Mentor Graphics MEMS design kit

A CMP® (Circuits Multi-Projects, Grenoble, France) / Mentor Graphics MEMS design-kit was used and evaluated for about one year under a contract with CMC [6].

The kit was installed on a Sun workstation running the Solaris operating system. Learning Mentor Graphics proved to be challenging, especially for new users who had no previous experience with Mentor Graphics and HDL modeling. The design kit provides a system design possibility using HDL simulation tools within the package. However, as mentioned above, it is only appropriate to MEMS structures simple enough to be described by a closed form equation, which then can be converted to its electrical "equivalent".

The package also has a cross-sectional viewer and an etch simulator. The cross-sectional viewer provides the user with a feel for the three dimensional representation of the object under design. The etch simulator gives the user a view of the released device after etching. However, the etch simulator gives reasonable predictions for simple structures, but not for more complex structures like the Cantilever-In-Cantilever [7]. The design rule checker provided with Mentor Graphics MEMS design kit proved to be adequate.

In general, the package is satisfactory for designing MEMS devices. It is neither significantly better nor worse than other MEMS design packages.

2.2.2 Cadence IC layout editor and Multi-User MEMS Processes (MUMPs) design kit

Cadence does not have a package for general MEMS design; the layout editor for IC design is used for mask design. Cadence uses the Solaris operating system. Design can only be implemented from the device approach.

The IC layout editor has many useful functions for object editing and learning to use it is relatively straightforward. It does not have any MEMS-related functionality like a cross-sectional viewer or etch simulator. However, Cadence has a Multi-User MEMS Processes (MUMPs) design kit available through CMC for surface micromachining design using the MUMPs technology of JDS Uniphase Inc. – MEMS Business Unit. The kit has a MUMPs device library, including some commonly used devices like comb drives, and electrostatic motors. Although the MUMPs technology is different to the CMOS technology, the design kit can be used for CMOS micromachining design by modifying its technology file. The design rule checker (DRC) of the kit needs improvement. Some parts of the layout with DRC violations turned out to be fine after fabrication; some parts without DRC violations did not work as expected afterwards.

In general, the layout editor of Cadence and the MUMPs design kit is satisfactory for MEMS and especially MUMPs design. The IC layout editor in Cadence is very convenient for mask design.

2.2.3 MEMSCAP® MEMS Pro

MEMS Pro is a full suite of tools for MEMS and IC design and layout. The package includes schematic entry for IC design, IC circuit simulation and waveform viewing, layout editing, design rule checking and MEMS libraries.

MEMS Pro runs on a PC with Windows 95, Windows 98, or Windows NT 4.0. It needs a Pentium processor or better and 150 MB of disk space.

The layout editor, L-Edit, is originally from Tanner Research, Inc. and is very efficient and easy to use for mask designing. Figure 2.3 shows the design interface of L-Edit with a serpentine-shaped polysilicon resistor as an example. The interface screen can be divided into three parts: the tool palettes on the top of the screen; the layer palette on the left of the screen and the work area, where the polysilicon resistor layout is drawn.

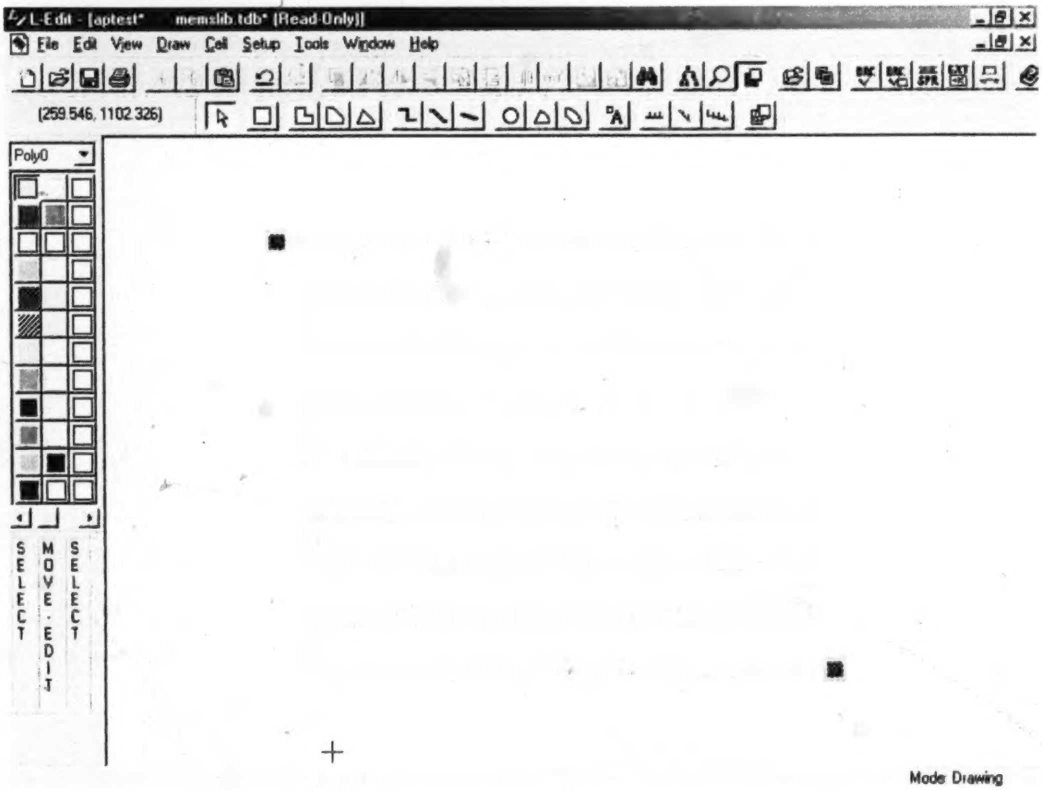

Figure 2.3 L-Edit user interface with a polysilicon resistor layout as an example

L-Edit provides standard shape selection, such as squares, circles and polygons. It also supports all-angle wire placement. The editing of shapes is easy with functionality such as stretch, rotate, flip and emerge. The design rule checker is also adequate.

Comparing the three packages introduced in this chapter, MEMS Pro has the advantage of ease of use and is amply equipped with the most features MEMS designer request. Its operating system is Windows. For designers with a preference for the Solaris operating system or designers with previous IC design experience, Cadence can be the best choice. It should be noted that both MEMS Pro and Cadence do not have an etch simulator by the time of writing this thesis. If the etching profile is critical to the design, a design package equipped with an etch simulator like the Mentor Graphics MEMS design kit will be necessary.

Both MEMS Pro and Cadence have been used in this project for the design and mask layout.

References:

[1] P. B. Chu, J. T. Chen, R. Yeh, G. Lin, J. C. Huang, B. A. Warneke, and K. S. J. Pister, "Controlled Pulse-Etching with Xenon Difluoride", *Ninth Int. Conf. Solid-State Sensors and Actuators (Transducers '97)*, Chicago, June 1997, pp. 665-668.

[2] R. Toda, K. Minami, and M. Esashi, "Thin Beam Bulk Micromachining Based on RIE and Xenon Difluoride Silicon Etching", *Ninth Int. Conf. Solid-State Sensors and Actuators (Transducers '97)*, Chicago, June 1997, pp. 671-674.

[3] F. I. Chang, R. Yeh, G. Lin, P. B. Chu, E. Hoffman, E. J. J. Kruglick, and K. S. J. Pister, "Gas-phase Silicon Micromachining with Xenon Difluoride", *Sym. on microelectronic structures and MEM devices for optical proc. and multimedia appl. (Proc. SPIE 2641)*, October 1995, pp. 117-128.

[4] I. W. T. Chan, K. B. Brown, R. P. W. Lawson, A. M. Robinson, Y. Ma and D. Strembicke, "Gas Phase Pulse Etching of Silicon for MEMS with Xenon Difluoride", IEEE Can. Conf. On Electrical and Computer Engineering, Edmonton, May 1999, pp. 1637-1641.

[5] D. Pellerin, D. Taylor, *VHDL Made Easy*, Prentice-Hall, Inc., London, 1997.

[6] Y. Ma and A. M. Robinson, "CMP/Mentor MEMS Design-kit Trial and Evaluation Report", Canadian Microelectronics Corporation, *Seminar on CMC's CAD support for MST*, Ottawa, January, 1998.

[7] B. Shen, CMOS Actuators, PhD Thesis, Department of Electrical Engineering, University of Alberta, Spring 1996.

Chapter 3

CMOS Optical Micro-Radiator

Incandescent filament light sources emit broadband radiation that extends from the visible wavelength to the infrared, which makes these sources very useful in optical signal generation. In recent years, miniature light sources have been fabricated utilizing micro-fabrication technologies [1-3]. In the sources described and used in these works, the filaments are electrically heated polycrystalline silicon bridges standing a few microns above a silicon substrate. The filaments are exposed to the atmosphere and thus are susceptible to rapid oxidation and contamination. In contrast to previous designs, our CMOS micromachined light source has a polycrystalline silicon filament embedded in layers of silicon dioxide and silicon nitride, which provides a degree of protection to these types of deterioration.

Design, post-processing and characterization of the CMOS optical micro-radiator are introduced in this chapter.

3.1 CMOS optical micro-radiator

Figure 3.1 shows a Scanning Electron Microscope (SEM) picture of a fabricated micro-radiator. A layer of serpentine-shaped polysilicon is embedded in a silicon dioxide platform. The polysilicon is employed as a resistor. The serpentine shape is chosen to increase the amount of heat generated on the micro-radiator platform and thus radiation emitted. Radiation aspects will be discussed in Chapter 4. Two supporting arms are used instead of the more commonly used four-arm configurations [4] in order to minimize the conduction heat loss through the arms. Because it is thermally isolated on its platform, modest currents are sufficient to heat the polysilicon to incandescence.

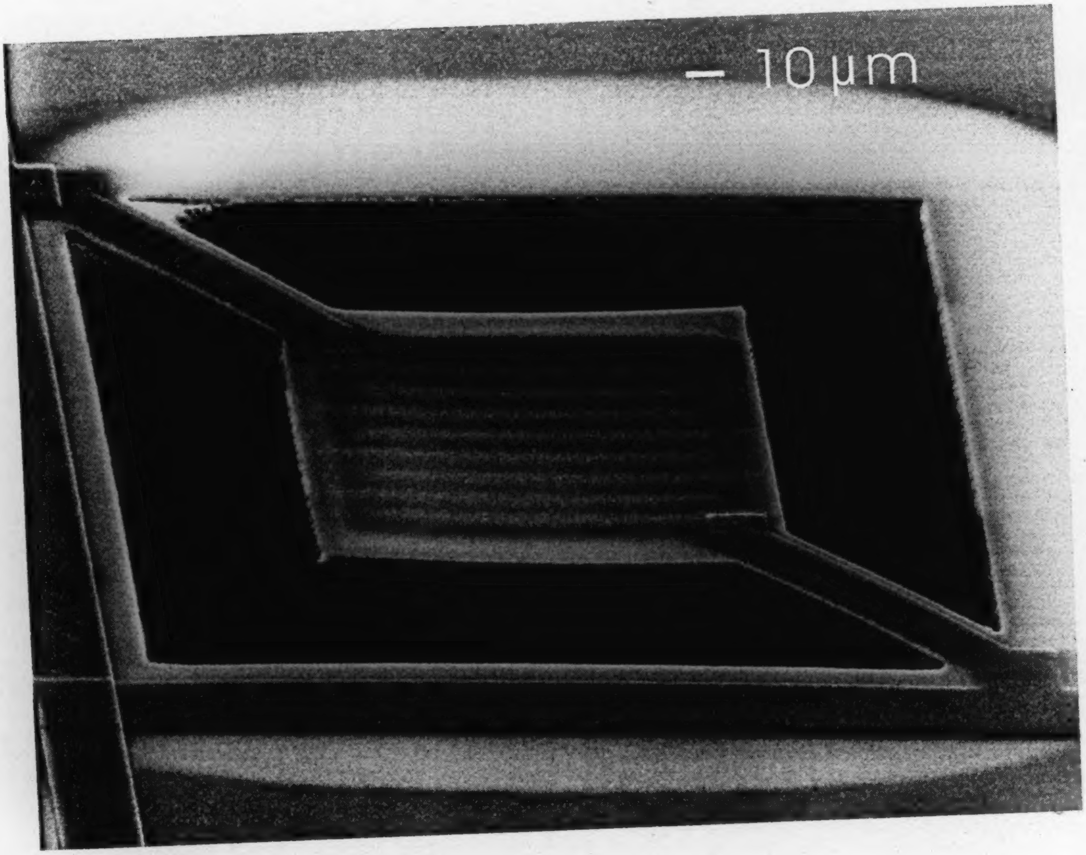

Figure 3.1 SEM picture of a serpentine-shaped polysilicon micro-radiator

The layout of the micro-radiator is shown in Figure 3.2 (A). The size of the platform is 120 μm × 120 μm. The width of the polysilicon is 5 μm and the total length is about 940 μm. Two arms suspend the platform and the length of each arm is 85 μm. Electrical power is supplied to the micro-radiator by the aluminum traces running through the arms. Polysilicon and aluminum are connected together in the regions called "contact".

A cross-sectional diagram of the micro-radiator platform along line CC' is shown in Figure 3.2 (B). The thickness of the platform is about 3.5 μm. At the bottom of the structure is a 0.9 μm field oxide layer, which is normally used to electrically isolate the polysilicon structure from the crystalline substrate. It is also widely used as structural material in MEMS. The field oxide layer may be etched a little during the fabrication and post-processing, which means a thickness smaller than 0.9 μm is possible. On top of the field oxide layer is a 0.32 μm layer of low-stress doped polysilicon. Then three layers of silicon dioxide are deposited to a total thickness of 2.3 μm. All thickness dimensions quoted here are specified by the CMOS manufacturer. The last layer deposited is a 0.5 μm layer of silicon nitride, which is used as a passivation layer in CMOS process. It has been suggested that the silicon nitride layer may be etched partly or totally during the etching process used to release the structure [5]. An follow-up experiment has been done to measure the etching rate of silicon nitride using XeF_2 as etchant [6]. A layer of 0.6 μm silicon nitride was patterned with photoresist to protect some surface area and etched with XeF_2 for 20 pulses. Then a profilometer was used to measure the thickness difference of the nitride layer between the protected and the etched areas. Experimental results indicated that the silicon nitride not protected was etched by XeF_2, but the thickness difference was very small and was not measurable by the profilometer.

A different configuration with polysilicon supporting arms instead of aluminum has also been designed. Heat loss through the arms decreases with this kind of configuration because of the smaller thermal conductivity of the polysilicon material compared with Al. Also, Ohmic heating of the polysilicon in the arms will tend to reduce the temperature gradient between the platform and the base of the arms at the substrate. Some experimental results obtained with this configuration are also presented in the following chapters.

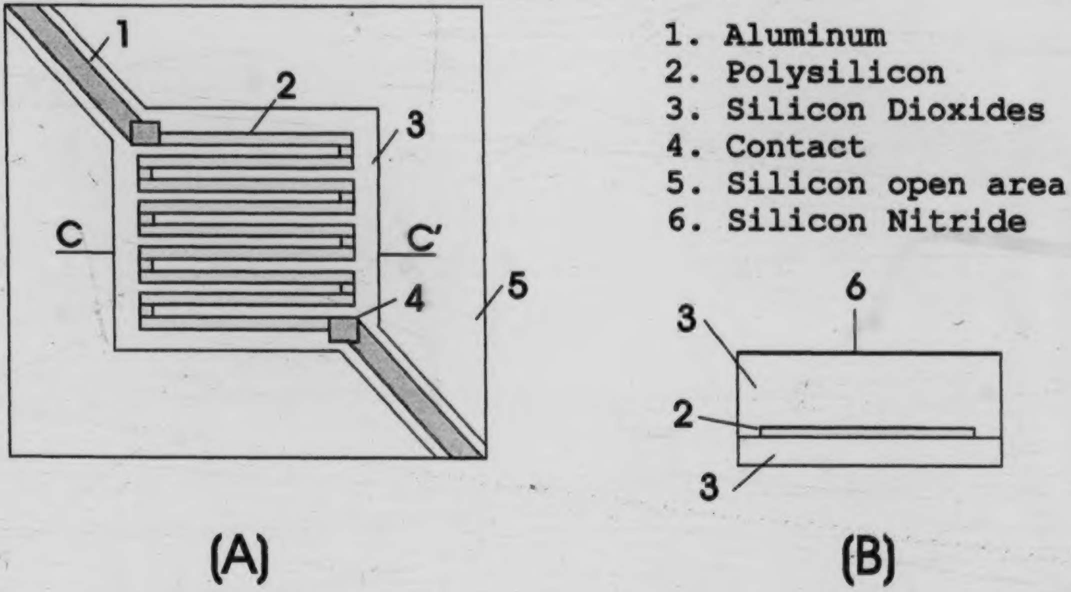

Figure 3.2 Micro-radiator layout (A) and cross-sectional diagram (B)

The micro-radiator is released by XeF_2. The XeF_2 etching system used to release the micro-radiators can be found in reference [7]. The etched pit as shown in Figure 3.1 is 85 μm in depth and the undercutting of the oxide layer due to the isotropic etching of silicon is about 50 μm on each side. The undercut is seen as the lighter colored regions extending from the edge of the square opening in the oxide layers in Figure 3.1.

3.2 Micro-radiator electro-thermal model

When electrical power W is supplied to the micro-radiator, it heats up. Because the micro-radiator platform is released and the presence of the air underneath the structure provides good thermal isolation, the temperature of the micro-radiator can be raised easily to several hundred degrees above the substrate temperature with a modest input power.

Three heat dissipation mechanisms occur for the power applied to the micro-radiator: conduction, convection and radiation. Figure 3.3 is a schematic representation showing the heat transfers related to the micro-radiator.

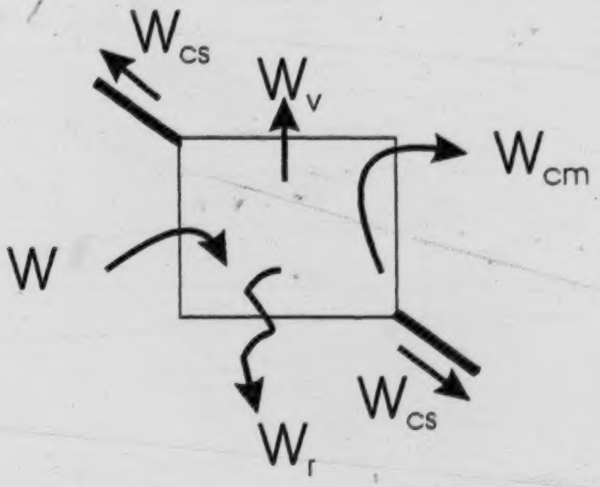

Figure 3.3 Heat transfers related to the micro-radiator

The micro-radiator temperature depends upon: (1) Rate of supply of electrical energy W; (2) Conduction heat loss through the gas W_{cm}, conduction heat losses from the micro-radiator platform via the support arms W_{cs}; (3) Convection heat loss W_v; (4) Radiation heat loss W_r.

Considering a simplified micro-radiator of width x, length y, and thickness z, suspended from the substrate by a distance s, as shown in Figure 3.4, the heat balance equation is given by

$$W - \dot{Q} = W - W_{cm} - W_{cs} - W_v - W_r = \rho cxyz\frac{\partial T}{\partial t} \tag{3.2.1}$$

in which, $\dot{Q}$ is the total heat loss from the platform, ρ is the mass density of the micro-radiator material, c is the specific heat and T is the average temperature of the micro-radiator.

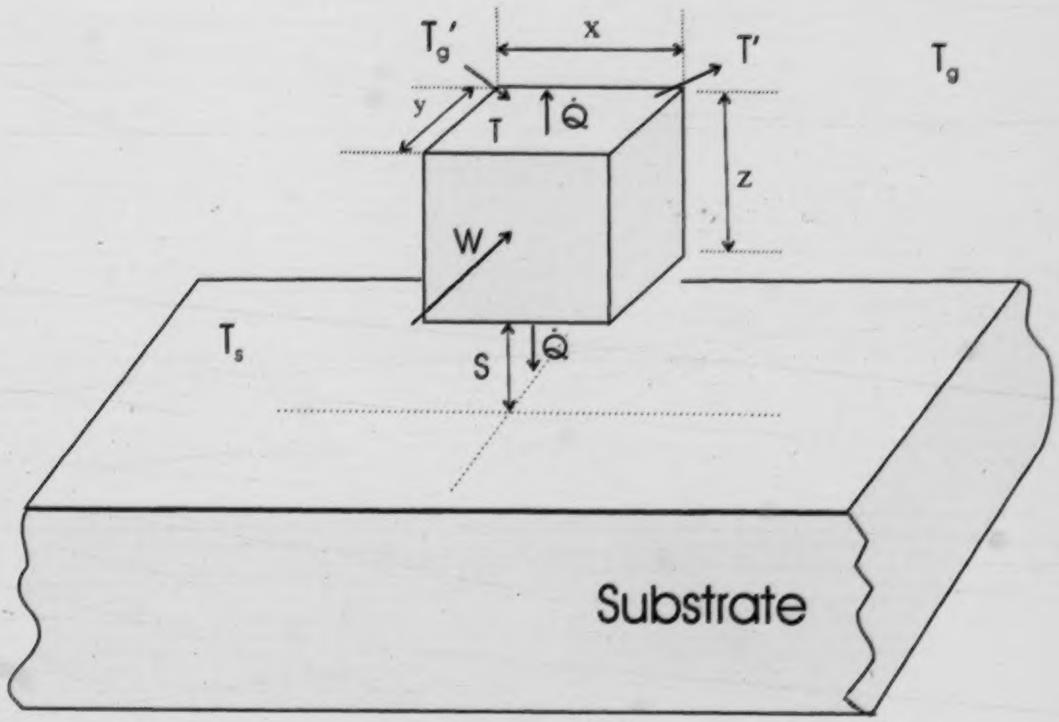

Figure 3.4 A simplified micro-radiator structure

3.2.1 Conduction heat loss through the gas and through the supports

The actual physical process of conduction heat loss through the free molecules of surrounding gas is very complex. If the gas molecules have average temperatures of T_g' and T' on arrival to, and departure from, the micro-radiator, respectively, as shown in Figure 3.4, the rate of energy transfer W_{cm} from the micro-radiator to the gas and to the substrate, is given by

$$W_{cm} = k_1 n(T' - T_g') = Kxy(T' - T_g')p \qquad (3.2.2)$$

where k_1, K are related constants, n is the number of molecules striking the micro-radiator per second, xy indicates the surface area of the micro-radiator as shown in Figure 3.4, and p is the gas pressure. W_{cm} is directly proportional to the pressure at any given gas temperature. Knudsen defined a constant α, called the accommodation coefficient, as [8]

$$\alpha = \frac{T' - T_g'}{T - T_g'} \tag{3.2.3}$$

where T, T_g' and T' are the temperatures of micro-radiator surface, the incident and the reflected molecules, respectively. Introducing this constant into equation (3.2.2) gives

$$W_{cm} = \alpha Kxy(T - T_g')p \tag{3.2.4}$$

K can be calculated from [9,10,11]

$$K = \frac{1}{4}\frac{\gamma+1}{\gamma-1}\sqrt{\frac{2k_0}{\pi m T_g}} \times 10^{-2} \tag{3.2.5}$$

where $\gamma = C_p/C_v$ is the ratio of the specific heats of the gas, k_0 is the Boltzmann constant, m is the mass of the gas molecule, and T_g the average temperature of the gas far from the micro-radiator. For air, $\gamma = 7/5$; $m = 28.98$ AMU.

T_g', the only unknown in equation (3.2.4), depends upon the gas mean free path λ_{mfp} and therefore upon the pressure. We assume the micro-radiator, with a platform dimension x by y, is placed in a chamber with diameter D and the distance from the bottom of the micro-radiator to the substrate, s, is always smaller than d, the larger one of x and y. There are four distinct conditions to consider in estimating T_g', (a) when $\lambda_{mfp} > D$, (b) when $d < \lambda_{mfp} < D$, (c) when $s < \lambda_{mfp} < d$, and (d) when $\lambda_{mfp} < s$. For (a), when $\lambda_{mfp} > D$, each molecule above the micro-radiator makes many collisions with the outer walls of the chamber and below the micro-radiator makes many collisions with the substrate and so is always in temperature equilibrium with the chamber wall and the substrate on striking the micro-radiator, making $T_g' = T_g$ or $T_g' = T_s$, the substrate temperature as shown in Figure 3.4. For (b), when $d < \lambda_{mfp} < D$, the molecules, although they may not reach the chamber wall, have many collisions with other molecules above the micro-radiator and have many collisions with the substrate below the micro-radiator between each collision with the micro-radiator. Therefore, $T_g' = T_s$ or $T_g' \approx T_g$. For (c), when $s < \lambda_{mfp} < d$, some molecules return to the micro-radiator before reaching equilibrium with the main body of the gas or the substrate, some reach the equilibrium with the substrate. T_g' is then very difficult to estimate because of the temperature gradient through the gas and the unknown percentage of collision with the substrate. For (d), when $\lambda_{mfp} < s$, most molecules return to the micro-radiator before reaching equilibrium with the main body of the gas and thus $T_g' > T_g$. The difference increases with increasing pressure.

A first order approximation that only considers the heat flow to the substrate at the base of the etched cavity may be calculated by

$$W_{cm} = \eta \alpha K x y \frac{(T - T_s)}{s} p \tag{3.2.6}$$

where K is the constant calculated in (3.2.5); α the accommodation coefficient; s the distance from the micro-radiator to the substrate. The factor η denotes the coefficient accounting for the first order approximation.

The equation for the heat conduction from the platform to the substrate via each support arm is averaged out along the whole arm for simplicity:

$$W_{cs} = n_s k_s A_s (T - T_s) / e \tag{3.2.7}$$

The factor n_s denotes the number of supporting arms, k_s is the thermal conductivity of the support arm material, A_s the cross-section area of the arm and e is the length of the arm.

3.2.2 Convection heat loss

Heat transition in a free convection boundary layer depends on the relative magnitude of the buoyancy and viscous forces in the gas. When natural convection occurs, all the convected heat is carried by the gas floating upward and eventually is carried away by the gas far above the device. The convection heat loss W_v is assumed to obey Newton's cooling law [12]

$$W_v = 2h(\upsilon, p)xy(T - T_g) \tag{3.2.8}$$

where $h(\upsilon,p)$ is the convective heat-transfer coefficient from the micro-radiator platform to the gas as a function of gas flow velocity υ and absolute pressure p. T_g is the temperature of the gas very far from the substrate.

It is customary to correlate the occurrence of natural convection in terms of the Rayleigh number, *Ra*. This number, characterizing the strength of the heat flow driving the turbulence, is defined as the product of the Prandtl and Grashof numbers *Pr* and *Gr* [13]:

$$\begin{aligned} Ra &= Gr \text{ x } Pr \\ &= \left(\frac{g\beta\rho^2 d_c{}^3 \Delta T}{\mu^2}\right)\left(\frac{\mu c_p}{k}\right) \\ &= \frac{g\beta d_c{}^3 \Delta T}{\nu\chi} \end{aligned} \tag{3.2.9}$$

where g is the acceleration due to gravity, β is the coefficient of thermal expansion of the air, ρ is the density of air, d_c the critical dimension of the structure defined as the ratio of the structure surface area to its perimeter, μ is the dynamic viscosity of air, C_p its specific heat at constant pressure, k its thermal conductivity, and χ its thermal diffusivity. The kinematic viscosity of air, ν, is a coefficient defined as the ratio of the dynamic viscosity of air μ to its density ρ. The relationship between thermal conductivity k and thermal diffusivity χ is given by $k = \rho c_p \chi$.

The Grashof number Gr is a measure of the ratio between buoyancy forces and viscous forces. The Prandtl number Pr measures the relative propensities of the fluid to diffuse momentum and heat.

In the case of our micro-radiator, $Gr \cong 7\times10^{-4}$ at atmospheric pressure and is even smaller at lower pressure, indicating that the buoyancy forces are minute compared with the viscous forces. The Prandtl number Pr is about 0.7 for air, so the Rayleigh number is about 5×10^{-4}. Usually the Rayleigh number needs to exceed 600 for convection to occur. The smallest Rayleigh number published is about 0.1 [13]. Therefore, it is resonable to assume that natural convection contributes virtually nothing to the cooling of the micro-radiator. Experimental results also proved the response of the micro-radiator to be independent of device orientation [14], which means the convection heat loss is negligible compared to other types of heat losses.

3.2.3 Radiation heat loss

The radiation heat losses can be approximated by

$$W_r = \varepsilon\sigma xy(T^4 - T_g^{\ 4}) + \varepsilon\sigma xy(T^4 - T_s^{\ 4}) \tag{3.2.10}$$

where ε is the emissivity of the micro-radiator material and σ is the Stefan-Boltzmann constant. T_g, as mentioned above, is the temperature of the gas and T_s is the temperature of the substrate. Here we assume that the upper face of the platform radiates to the gas while the bottom face radiates to the substrate. Radiation from the side faces of the platform is assumed small and is neglected here.

3.2.4 Total heat loss

If we assume $T_g \approx T_s$, W_{cm}, W_{cs} and W_r can be written as

$$W_{cm} = K_{CM}\alpha(T - T_g)p \tag{3.2.11}$$

$$W_{cs} = K_{CS}(T - T_g) \quad (3.2.12)$$

$$W_r = K_R(T^4 - T_g{}^4) \quad (3.2.13)$$

where K is defined as equation (3.2.5), K_{CM}, K_{CS} and K_R are equal to

$$K_{CM} = \eta Kxy / s \quad (3.2.14)$$

$$K_{CS} = n_s k_s A_s / e \quad (3.2.15)$$

$$K_R = 2\varepsilon\sigma xy \quad (3.2.16)$$

Therefore the heat balance equation of the micro-radiator can be written as:

$$W - K_{CM}\alpha(T - T_g)p - K_R(T^4 - T_g{}^4) - K_{CS}(T - T_g) = \rho cxyz\frac{\partial T}{\partial t} \quad (3.2.17)$$

It is very difficult to analytically solve the heat balance equation, equation (3.2.17), with each term included. A simple calculation that ignores the convection and radiation heat losses, has been done in reference [15]. The calculation shows the average temperature rise yields an exponential time variation

$$\Delta\overline{T}(t) \propto (1 - e^{(-t/\tau)}) \quad (3.2.18)$$

with a time constant τ that depends on the surrounding gas pressure. A measurement of the time constant shows τ is about 30 ms at 10^{-4} Torr and about 15 ms at one atmosphere [14].

An analytical solution for the average temperature of micro-radiator, T, is difficult to get from equation (3.2.17), but the relationship between T and the surrounding gas pressure p, can be plotted by solving p from equation (3.2.17) at equilibrium:

$$p = \left(W - K_R(T^4 - T_g{}^4) - K_{CS}(T - T_g)\right) / K_{CM}\alpha(T - T_g) \quad (3.2.19)$$

Figure 3.5 shows a curve of micro-radiator average temperature versus the surrounding gas pressure at equilibrium with an input power of 10 mW and a room temperature of 293 K. The curve was plotted using Matlab and the source code can be found in Appendix A. A series of temperatures from 273 K to 2000 K was used to calculate the corresponding equilibrium pressure using equation (3.2.19) and the results were plotted by temperature as a function of pressure. Please refer to Appendix A for details.

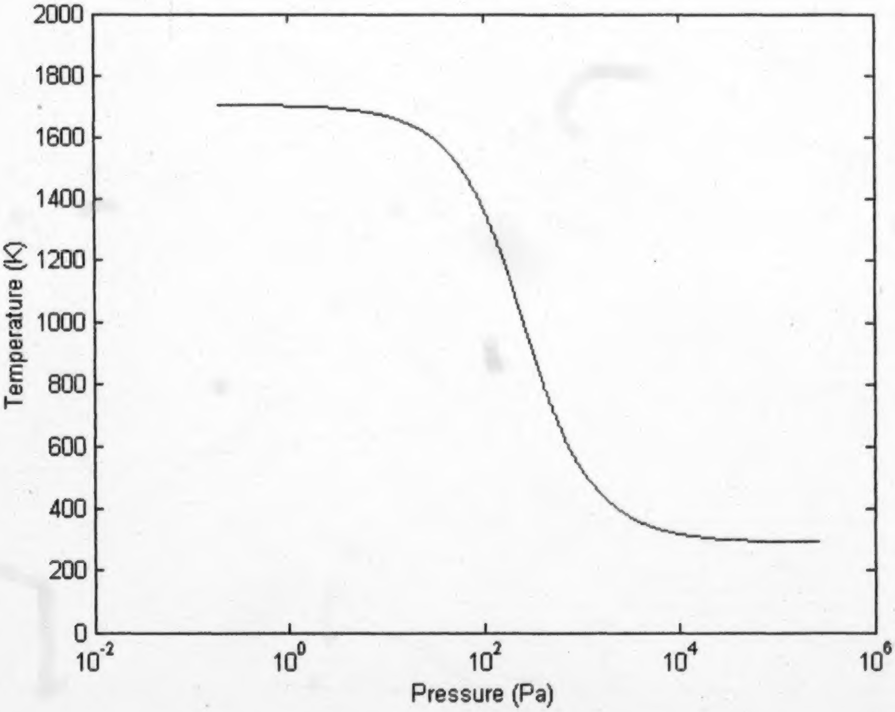

Figure 3.5 Average temperature of the micro-radiator versus the surrounding gas pressure operating at a power of 10 mW

Figure 3.5 demonstrates the typical shape for a thermal conductivity pressure gauge. In the middle part of the curve (pressure range from 10^1 Pa to 10^3 Pa), the gas conduction heat loss tends to dominate and the temperature of the micro-radiator is a strong function of the gas pressure. At high pressure, the thermal conductivity of the gas is independent of the pressure and therefore the temperature of the structure is almost constant as a function of pressure. At low pressure, the conduction heat loss through air becomes significantly smaller than the radiation and the conduction through the arms and the temperature becomes again independent of the pressure. The temperature simulated by the Matlab program in Figure 3.5 is lower than the temperature derived from measured resistance at high pressure and higher than the temperature derived at low pressure. The difference between the experimental data and the simulation results is due to the assumptions made in the theoretical model and considered acceptable in this project.

3.2.5 Thermal conductivity gauge useful range

Figure 3.6 shows temperature variations of a micro-radiator under two different power inputs W_1 and W_2, with $W_1 < W_2$. Temperature variations between points A and B on curve W_1 and A', B' on curve W_2 vary sharply with pressure and are regarded as the sensitive and useful ranges of the gauge.

The lowest useful pressures indicated as point A and A' are determined when the radiation W_r and conduction heat loss through the supports of the device W_{cs} equal the conduction through the gas W_{cm}. The upper pressure limit indicated by point B and B' are determined when the mean free path becomes comparable to the dimension of the micro-radiator and the distance between the micro-radiator to the substrate (Knudsen number $Kn \approx 1$), so that molecules departing from the radiator lose their thermal energy within a short distance. This forms a hot sheath of gas that inhibits further heat transport.

For the input powers of W_1 and W_2, the average temperature of micro-radiator at a certain pressure is higher with power W_2 than the temperature obtained with power W_1. Thus the radiation heat loss and conduction heat loss through the supports are higher and the conduction heat loss through the gas W_{cm} becomes comparable to W_r and W_{cs} (points A and A') at a higher pressure. The lowest useful pressure limit A on curve W_1 moves to a higher pressure point A' on curve W_2 as indicated in Figure 3.6.

The micro-radiator operating at power W_2 also heats up the surrounding air to a higher temperature than the one at power W_1. The mean free path of the surrounding gas under W_2 is therefore larger at a certain pressure because $\lambda_{mfp} \propto \frac{T}{p}$. The upper pressure limit B moves to a higher pressure B', where the mean free path becomes comparable to the characteristic dimension of the system again.

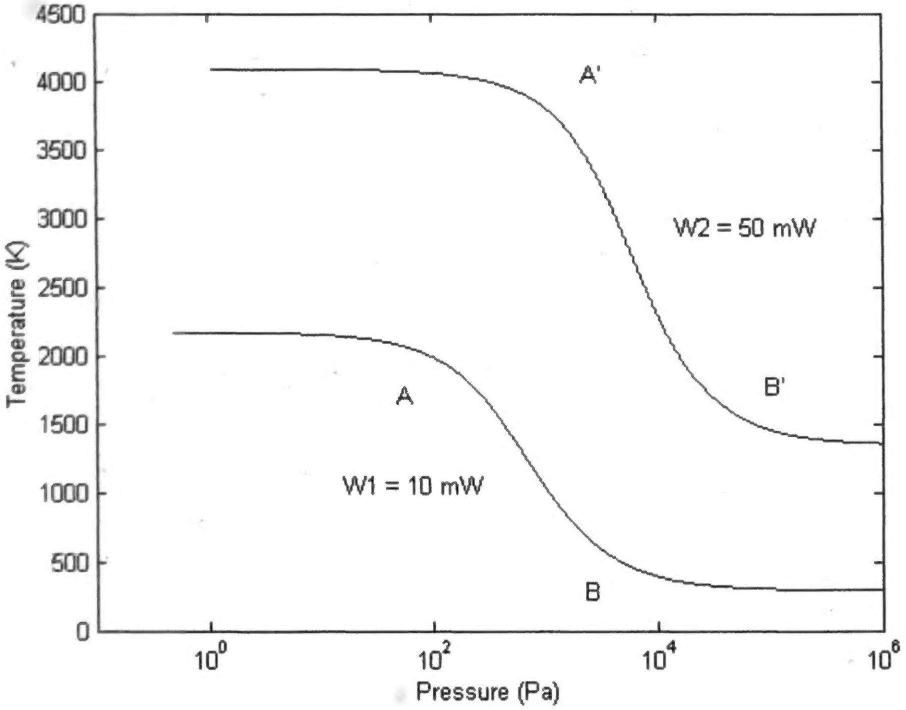

Figure 3.6 Temperature variation of a typical thermal-conductivity gauge operating at constant power inputs of 10 and 50 mW

Comparing the temperature variation curves under power W_1 and W_2 in Figure 3.6, we can see the sensitive pressure range shifts to the right when the input power increases. In the next chapter, we will see the spectral emission of the micro-radiator not only increasing in absolute magnitude, but also shifting more into the response region of the photodetector when the input power increases. This enables the sensitivity and pressure range of the gauge to be varied by manipulating the input power to the micro-radiator.

References:

[1] M. Tuma, K. King, L. Kim, R. Hansler, E. Jones and T. George, "MEMS incandescent light source", SPIE Proceeding, vol. 4139, August 2000.

[2] G. Lamb, M. Jhabvala, and A. Burgess, "Integrated-circuit broadband infrared sources", *NASA Tech. Briefs*, March 1989, p. 32.

[3] R. T. Howe and R. S. Muller, "Polycrystalline silicon micromechanical beams", Extended Abstract, Electrochemical Society Meeting, , Montreal, Canada, May 9-14, 1982, pp. 186-189.

[4] M. Parameswaran, A. M. Robinson, D. L. Blackburn, M. Gaitan and J. Geist, "Micromachined Thermal Radiation Emitter from a Commercial CMOS Process", IEEE Electron Device Letters, Vol. 12, no. 2, 1991, pp. 57-59.

[5] Sandra Esteves, "CMOS Micromachined Devices for Applications in Fluids", M.Sc. Thesis, Department of Electrical and Computer Engineering, University of Alberta, 2000.

[6] Private communication, Dr. A. M. Robinson, University of Alberta; M. Hu / D. Lu 's report, unpublished, February 2001.

[7] I. W. T. Chan, K. B. Brown, R. P. W. Lawson, A. M. Robinson, Y. Ma and D. Strembicke, "Gas Phase Pulse Etching of Silicon for MEMS with Xenon Difluoride", IEEE Can. Conf. Electrical and Computer Engineering, Edmonton, May 1999, pp. 1637-1641.

[8] M. Knudsen, Ann. Phys., Lpz., vol. 34, 1911, p. 593.

[9] J. M. Lafferty, Fundations of Vacuum Science and Technology, John Wiley & Sons, Inc., New York, 1998, p. 406.

[10] A. Bejan, *Convection Heat Transfer*, Wiley-Interscience, New York, 1984.

[11] H. Von Ubisch, "On the Conduction of Heat in Rarefied Gases and Its Manometric Application", Appl. Sci. Res., Vol. A2, 1951, pp. 364-430.

[12] C. H. Mastrangelo, *Thermal Applications of Microbridges*, Ph.D. Thesis, University of California, Berkeley, 1991, p.14.

[13] Private communication, J. Jones, *Cooling of a Circuit Element*, Simon Fraser University, School of Engineering Science Memo, June 5th, 1990.

[14] B. Shen, Z. Lai, A. M. Robinson and W. Allegretto, "Thermal response of CMOS-micromachined thermistor sensors under constant power and constant current excitation", *Rev. Sci. Instrum.* 65 (11), November 1994, pp. 3528-3534.

[15] B. Shen, CMOS Actuators, PhD Thesis, Department of Electrical Engineering, University of Alberta, Spring 1996.

Chapter 4

Experiment Configuration and Measurement Sensitivity

Figure 4.1 shows the experimental configuration in a diffusion-pumped bell jar working chamber. A 3 mm by 3 mm silicon loose die with a linear array of micro-radiators is mounted in a Dual In-line Package (DIP) with silver paint. Manual wire bonding was performed to provide electrical connection to the micro-radiators. The DIP is then put into the vacuum chamber with wires directly wrapped around the pins as shown in Figure 4.1. For testing in air, the DIP is put into a Zero Insertion Force (ZIF) socket which provides electrical connections from the DIP pins to the Experiment Control System. The zero insertion pressure feature of the socket allows easy insertion and removal without pin distortion. The radiation from the micro-radiator is measured by a photodetector. The experiment Control System consists of two parts: a digital constant power supply unit, which supplies constant power to the micro-radiator, and a data acquisition unit, which measures the output of the photodetector. Details of each part of the configuration will be given in the following sections.

4.1 Variable pressure chamber

The variable pressure chamber is a glass bell jar vacuum chamber. A diffusion pump along with a mechanical rotary pump controls the pressure of the system.

The chamber is first pumped down to 10^{-2} Torr by the rotary pump, then down to 10^{-5} Torr by the diffusion pump. The pumps are then isolated from the chamber and air is slowly bled into the bell jar. The controlled inflow rate is low enough to avoid forced convective cooling of the device.

Four pressure gauges measure the pressure of the chamber: Two Wallace & Tiernan diaphragm manometers (20 –700 torr, 0.5 – 20 torr), a Pirani gauge (0.01 – 0.5 torr), and a Bayard-Alpert ionization gauge (10^{-5} – 0.01 torr).

The micro-radiator is mounted in the chamber with the photodetector directly above. The distance between the micro-radiator and the photodetector is about 2.5 cm. Six feed-through connectors connect the micro-radiator and photodetector within the chamber to the outside equipment.

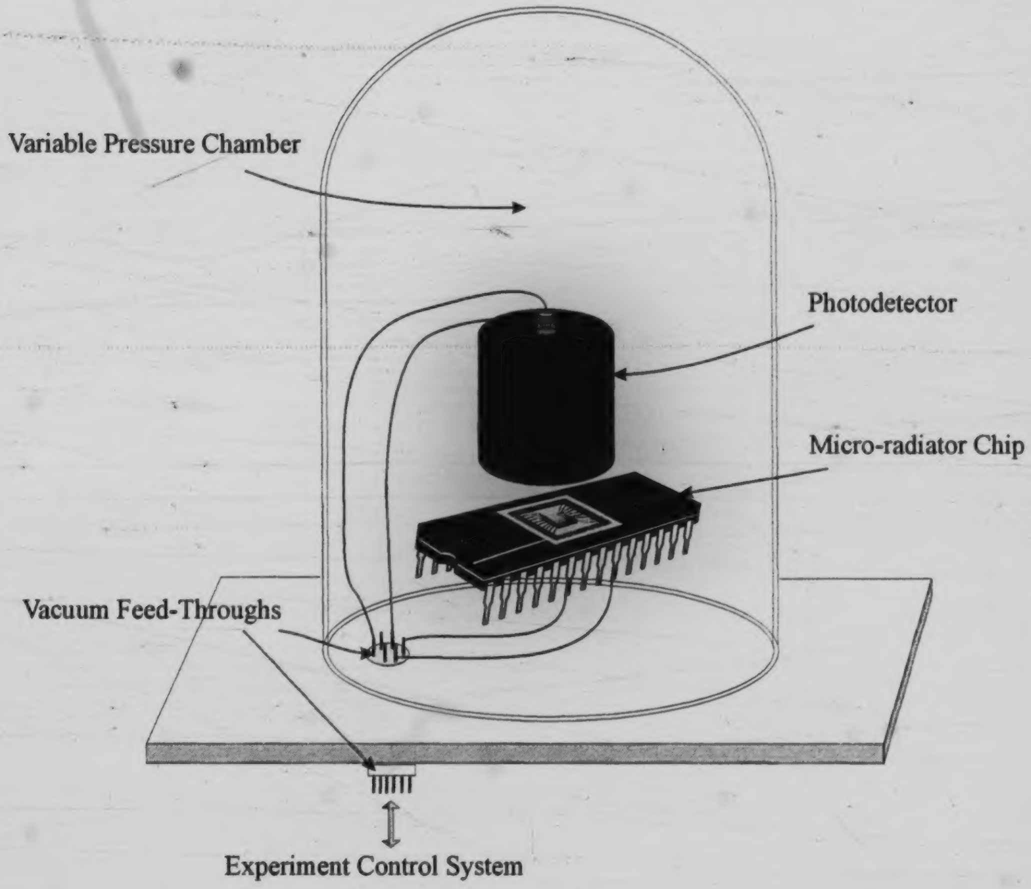

Figure 4.1 Experiment setup

4.2 Photodetector and point source of light

The photodetector used in the experiment is a silicon photodetector fabricated by Melles Griot, model: 13DAS 011/C, with an active area of 100 mm^2. Response from 400 nm to 1100 nm at 10 nm intervals of the photodetector provided by the manufacturer is shown in Figure 4.2. Responsitivity of the photodetector is defined as the ratio of the output current (in Amperes) from the detector to the intensity of incident light (in Watts). From Figure 4.2, we can see the photodetector is most sensitive at 985 nm. Response data below 400 nm and above 1100 nm are not available.

The photodetector signal is amplified by a large dynamic amplifier fabricated by Melles Griot (model 13 AMP 003) and can be directly read into the computer by an Hewlett Packard Instrument Basic interface card. The measured dark current of the photodetector is about 0.008 nA.

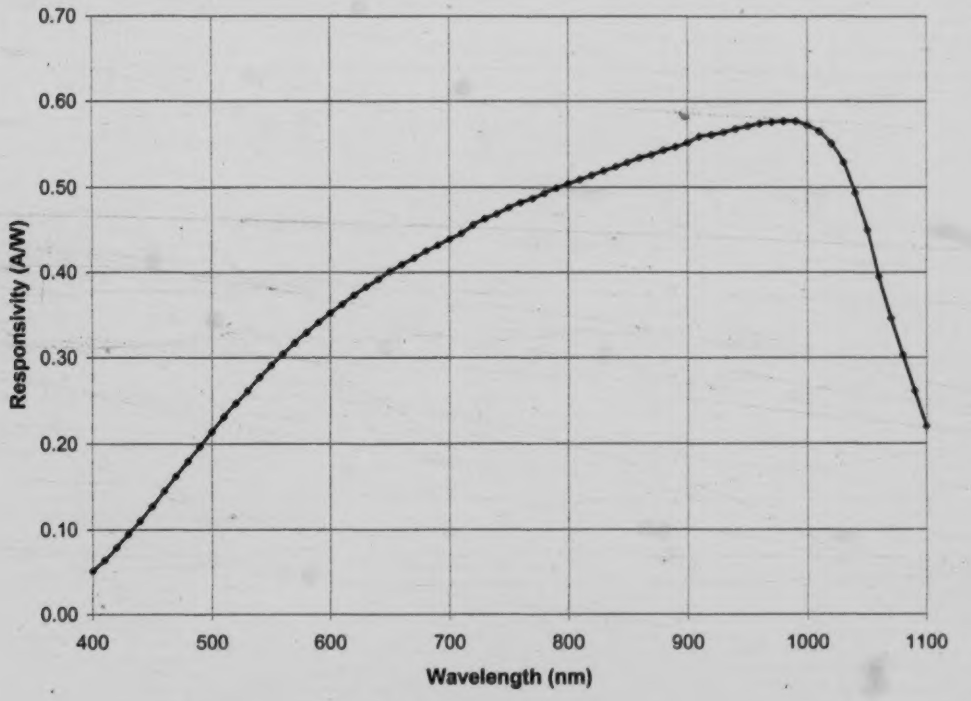

Figure 4.2 Response data for silicon photodiode 13 DAS 011/C

The relationship between the photodetector response and the intensity of light incident upon it was measured using a light bulb as a point source and varying the distance of the light source from the photodetector.

As we know, light is electromagnetic waves. The wavefronts of a point source of light are spherical surfaces and light intensity J represents the amount of energy per unit time per unit area transported across any surface oriented normally to the propagation direction. The total rate of flow of electromagnetic energy dU/dt across any such spherical surface of radius r may be obtained by integrating the intensity over the area of the spherical surface as shown in Figure 4.3:

$$\frac{dU}{dt} = \oint J da = 4\pi r^2 J \tag{4.2.1}$$

Since the total rate of flow of energy across any spherical surface is the same, for two surfaces of radii r and r' at which the intensity has the values of J and J', we have

$$\frac{J}{J'} = \frac{r'^2}{r^2} \tag{4.2.2}$$

Thus the intensity for a point source of light at any point is inversely proportional to the square of the distance from the point to the source

$$J = k'\frac{1}{r^2} \tag{4.2.3}$$

where k' is a constant that depends on the point source.

The point source constructed for the measurement is shown in Figure 4.4. A 12 V tungsten filament light bulb is used as the light source. A piece of frosted glass and several pieces of plain paper are put in front of the light bulb to diffuse the light completely to get a uniformly scattered light output. An iris is put in front of the frosted glass and set to its smallest size, which has a diameter of about 0.5 mm.

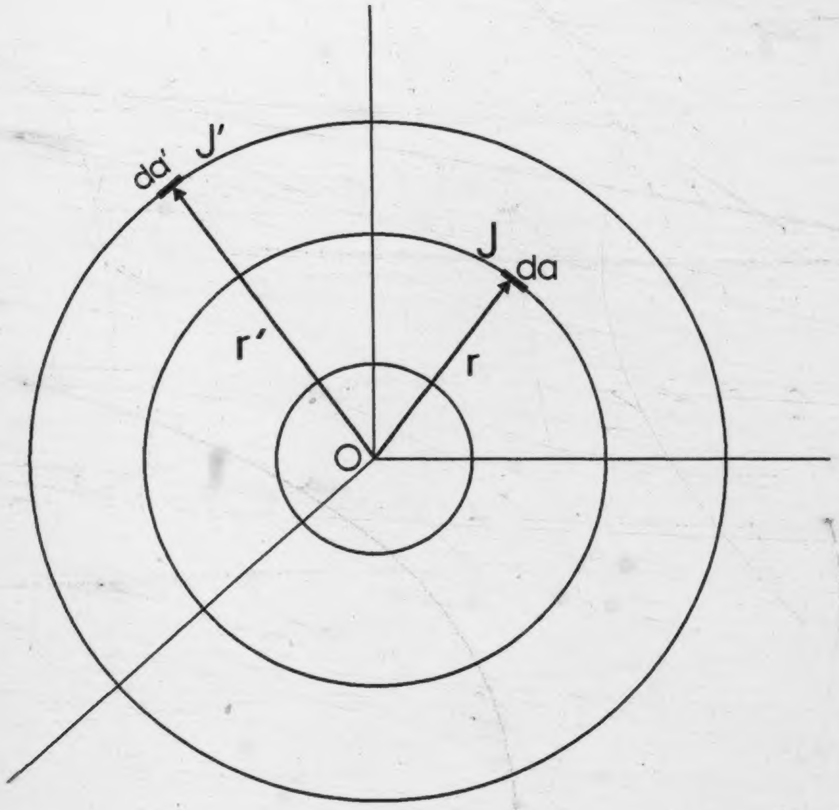

Figure 4.3 Spherical wavefronts produced by a point source of light at O

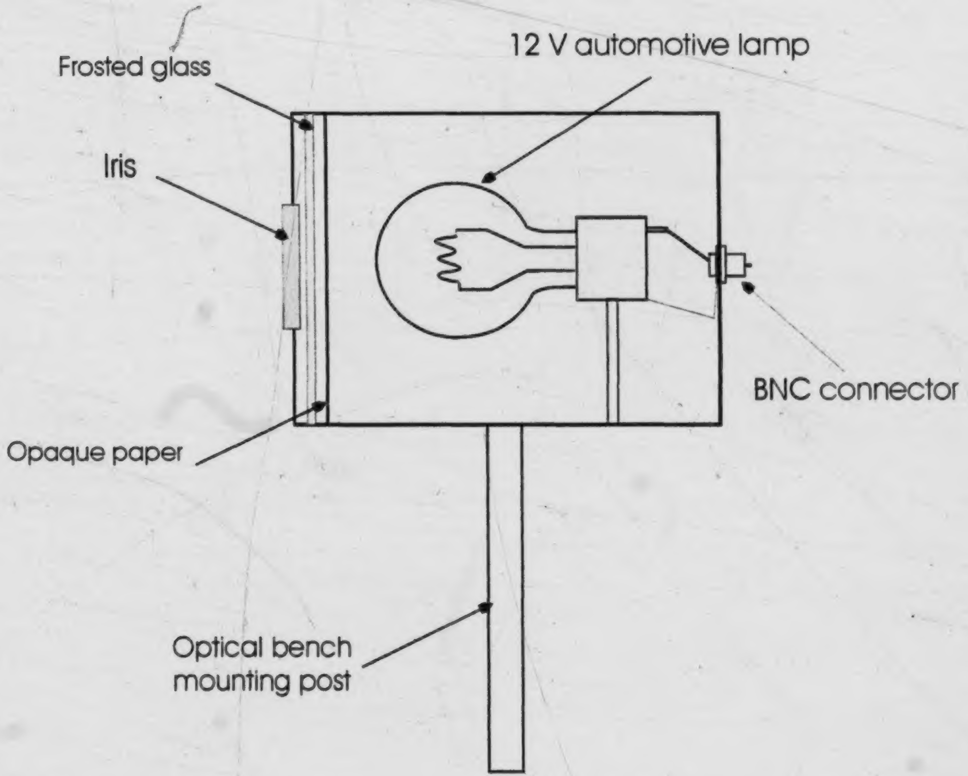

Figure 4.4 Schematic of point source of light

The photodetector response versus the inverse distance squared from the light source is shown in Figure 4.5. The photodetector signal is negative due to the characteristics of the photodetector, which will be discussed in detail in Chapter 7. In the following parts of the thesis, most of the photodetector output except the ones in Figure 4.8 and Figure 4.11 will be plotted in absolute value of the photodetector output current for the ease of understanding and data processing. The distance from the light source to the photodetector varies from 7.9 cm to about 50 cm. Experimental data are least square fitted onto a straight line and the equation of the line is shown on the graph.

From equation (4.2.3) and the experimentally fitted equation of Figure 4.5, we can see the photodetector signal at any point is linear with respect to the intensity of the light at that point:

$$I_d = k'J \tag{4.2.4}$$

where k' is a constant depending on the characteristics of the photodetector and the light source. If we assume the Melles Griot photodetector has a linear response to the intensity of the incident light, this experiment proves that the light source behaves as a point source of light. This light source will be used as a point source of light to test for linearity of the CMOS detector in Chapter 7.

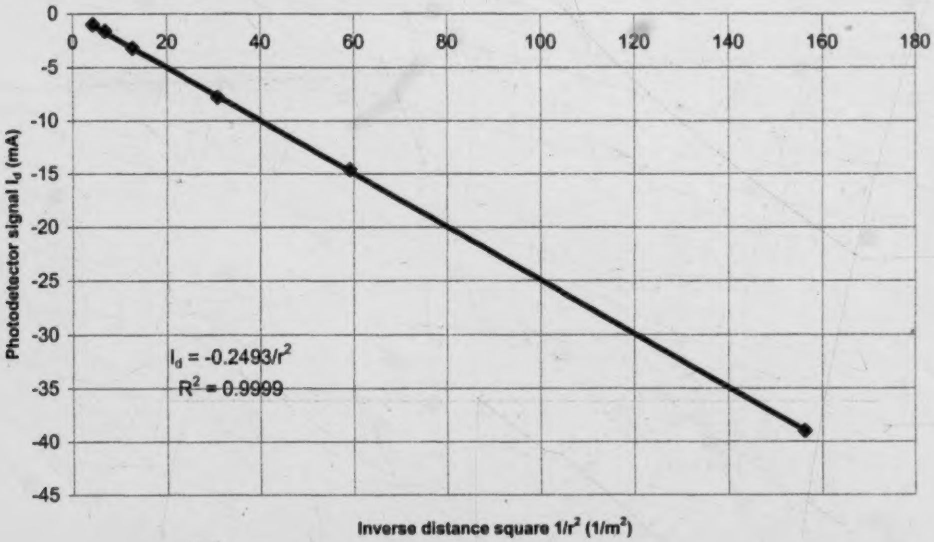

Figure 4.5 Photodetector signal versus inverse distance squared of the light source

4.3 Digital constant power supply unit and data acquisition unit

The mode of operation of the micro-radiator system is crucial to its successful functioning. The signal from the photodetector must be constant under constant operational conditions. This is especially critical for the measurement of radiation and its sensitive dependence on the emitter temperature. This section examines the three modes of operation of the emitter: constant current, constant voltage and constant power.

The polysilicon has a positive temperature coefficient of resistance α_T, which is constant provided the power supplied to it is lower than a threshold value [1]. The resistance R will increase when a current passes through the polysilicon due to Joule heating and for large currents can lead to thermal runaway and ultimately to destruction. We described earlier that the thermal response time of these micro-radiator is approximately 20 ms. However, there exists a phenomenon where the polysilicon resistance increases slowly with time while under power when the power is above a threshold value. The threshold power can be as low as 9 mW for microresistors similar to the ones used in this project [1]. Figure 4.6 shows the radiation signal from the micro-radiator detected by the photodetector versus time when a constant current $I_0 = 1.7\ mA$ is supplied to the micro-radiator at atmosphere pressure. The micro-radiator is operating above the threshold power where the resistance slowly increases. The magnitude of photodetector signal increases from 0.075 nA to about 0.14 nA in 350 seconds, which means the magnitude of photodetector signal increases about 87% in this time. This is due to the power supplied to the polysilicon, $W = I_0^2 R$, which increases when R increases; the corresponding increase in temperature T shifts the polysilicon emission further into the response region of the detector.

At the cessation of the experiment in Figure 4.6, the micro-radiator room temperature resistance, R_0 and the temperature coefficient of resistance, α_T, have permanently changed. The existence of changing values of R_0 and α_T are linked to the polysilicon resistance trimming process that has been investigated for a number of years [2]. A number of mechanisms for these changes will be discussed in Chapter 5.

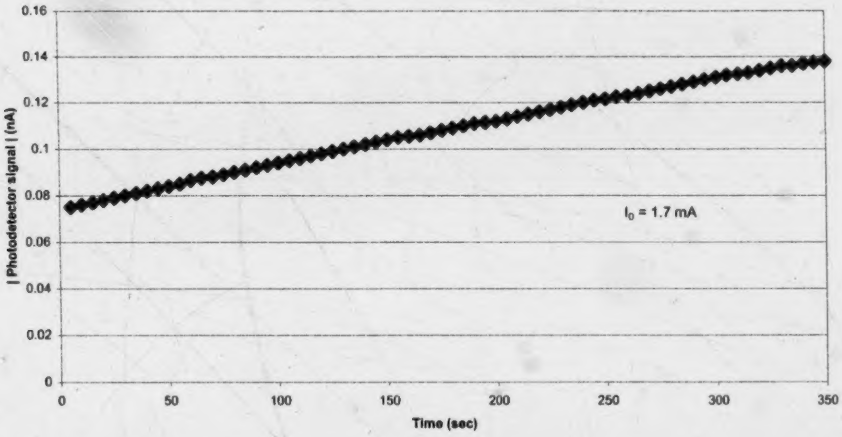

Figure 4.6 Variation of photodetector signal versus time operating with constant current at atmospheric pressure

Figure 4.7 shows the photodetector signal when a constant voltage $V_0 = 10\ V$ is applied to the micro-radiator. Data were recorded every five seconds. The power supplied to the polysilicon, $W = V_0^2 / R$, decreases when R again slowly increases due to the effect discussed above. The corresponding decrease in temperature T also shifts the polysilicon emission out of the detector response region. The magnitude of the photodetector signal decreases from 0.65 nA to about 0.51 nA in 350 seconds, a decrease of about 22%.

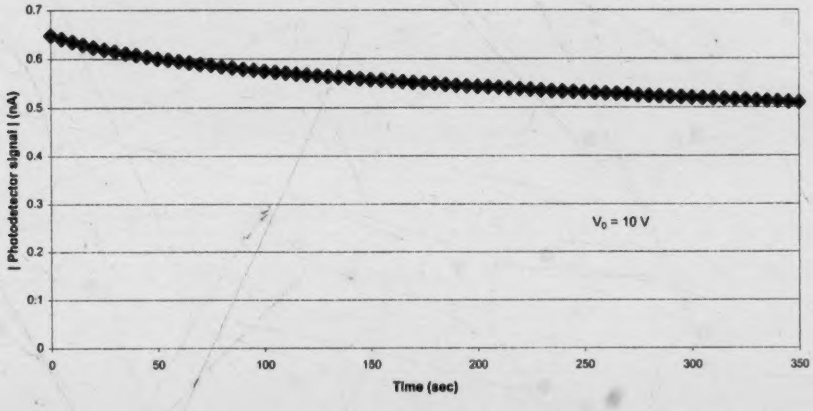

Figure 4.7 Variation of photodetector signal versus time operating with constant voltage at atmospheric pressure

Because the resistance of polysilicon and hence the radiation signal increases or decreases with time in the above two modes of operation above the power threshold, neither of them is suitable for use as a pressure sensor.

In order to keep the radiation from the micro-radiator constant at a given pressure, we keep the power supplied to the micro-radiator constant. Haswell and Robinson developed an analog constant power system [3] and Hogg, Warkentin and Thurston developed a digital constant power system in 1994 [4]. The digital constant power system is modified and used in this project to allow the users to not only apply constant power, but also to be able to apply power waveform functions other than just constant power to the micro-radiator.

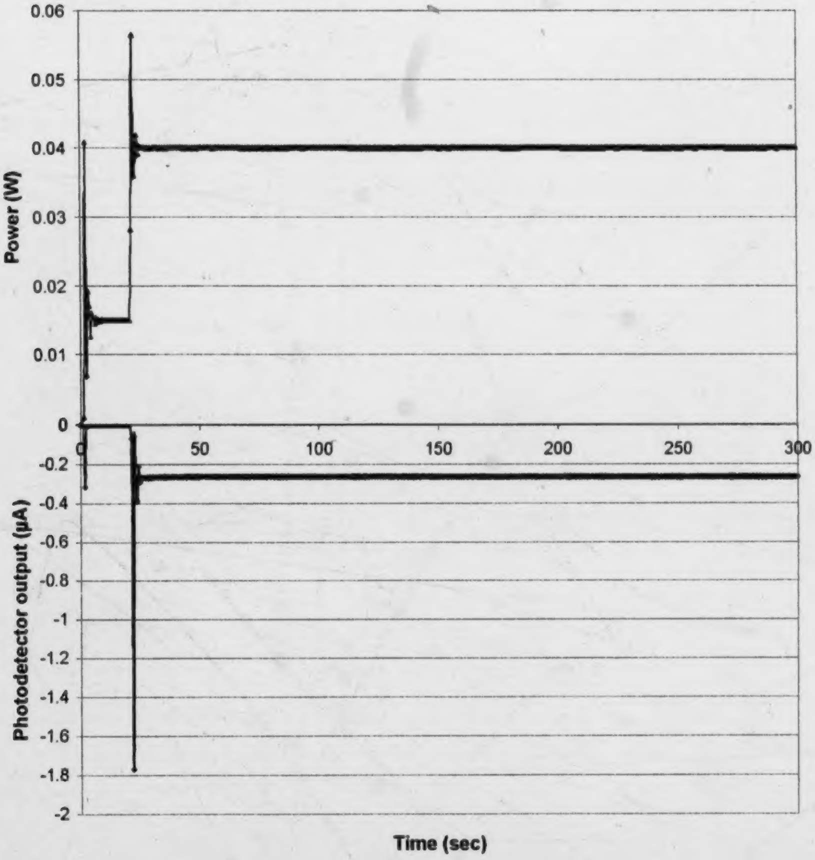

Figure 4.8 Photodetector signal (bottom) showing the radiation follows in a non-linear fashion the variation of the power supplied to the micro-radiator (top)

Figure 4.8 shows the output of the photodetector when it is used to monitor the radiation from a micro-radiator heated under a constant power of 40 mW using the CPS. The top half of the figure shows the electrical power applied to the micro-radiator while the lower half shows the photodetector signal. Before the constant power level reaches 40 mW, a power level of 15 mW was used to pre-heat the device for about 20 seconds to decrease the magnitude of the overshooting at the beginning of 40 mW power stage. Details about the overshooting will be described in the following section. The radiation from the micro-radiator at 40 mW was in the visible range, which indicates the temperature of the polysilicon was very high and its resistance changes significantly. However, the photodetector signal remains constant due to the constant input power, which makes the CPS a suitable operation mode for pressure sensing using the micro-radiator.

4.3.1 Test of constant power supply unit

The CPS is the main part of the experiment control system. The CPS controls a Keithley 236 Source Measure Unit (SMU) using a computer program written in Instrument Basic and supplies constant power through the micro-radiator at a specified level regardless of the value of the resistance. The other part of the experiment control system is a data acquisition unit, which acquires output data of the photodiode from a digital multi-meter. Details about the experiment control system including the design flow chart, user interface and the Instrument Basic program are included in Appendix B.

The digital constant power supply unit was tested with different powers from the CPS applied to the micro-radiator operated at atmospheric pressure. Figure 4.9 (a) shows a typical result when the power supplied is a staircase function. The power applied to the micro-radiator increases 2 mW every 30 seconds from 16 mW up to 50 mW. The micro-radiator starts to glow from about 30 mW.

For a power level not high enough to cause failure of the polysilicon micro-radiator, the fluctuation of the digital constant power is less than 0.2% after the initial homing-in of the system onto the set power. Figure 4.9 (b) shows the details of the overshoot and homing-in processes. This procedure takes a longer time at higher constant power when the temperature of the micro-radiator is higher, but it usually takes less than five seconds. The cause of the power over-shooting at the beginning of each power level is due to the continuous change of polysilicon resistance and the way the software calculates the current output. Details about the programming can be found in the Appendix. If the power supplied to the micro-radiator is too high, the resistance of the micro-radiator increases dramatically to infinity, which will cause the power shown in Figure 4.9 to increase, ultimately, to infinity.

Figure 4.10 shows the variation of the power dissipated by the micro-radiator under a series of power levels from 5 mW to 15 mW for 10 minutes respectively. The data were only recorded when the change in power is larger than 0.01%. The fluctuation of the power is less than 0.15% after the initial homing-in of the system. A power level about half the magnitude of the specified power is supplied to the micro-radiator at the beginning of each test to minimize the magnitude of power over-shooting.

The digital constant power supply unit is also been tested for long-term stability and yielded power fluctuations of ±0.4% over an 80-hour period.

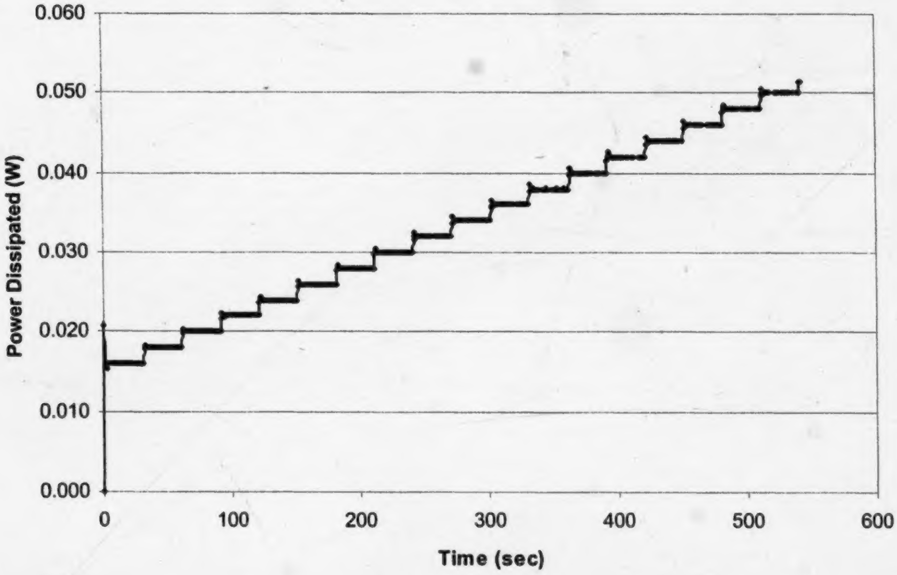

Figure 4.9 (a) Test of digital constant power supply unit with staircase function power output

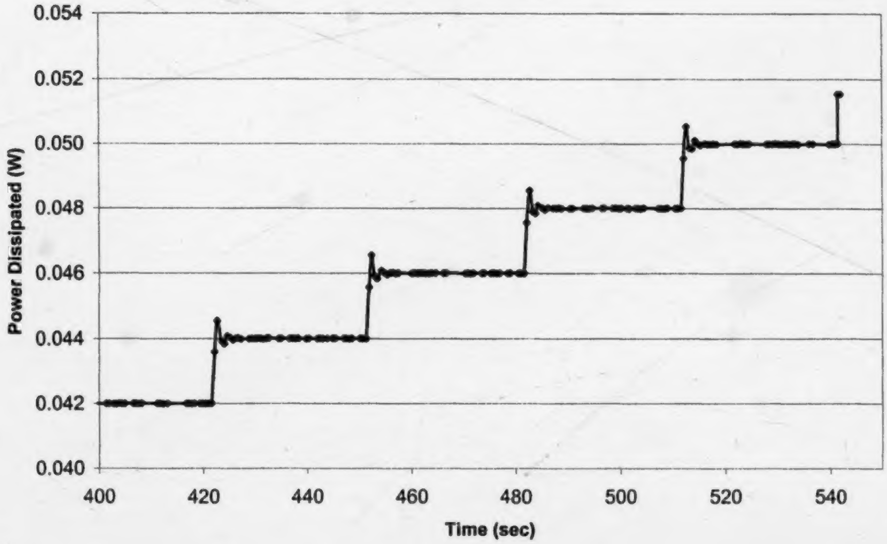

Figure 4.9 (b) Test of constant power supply unit showing the "homing-in" procedure of the system

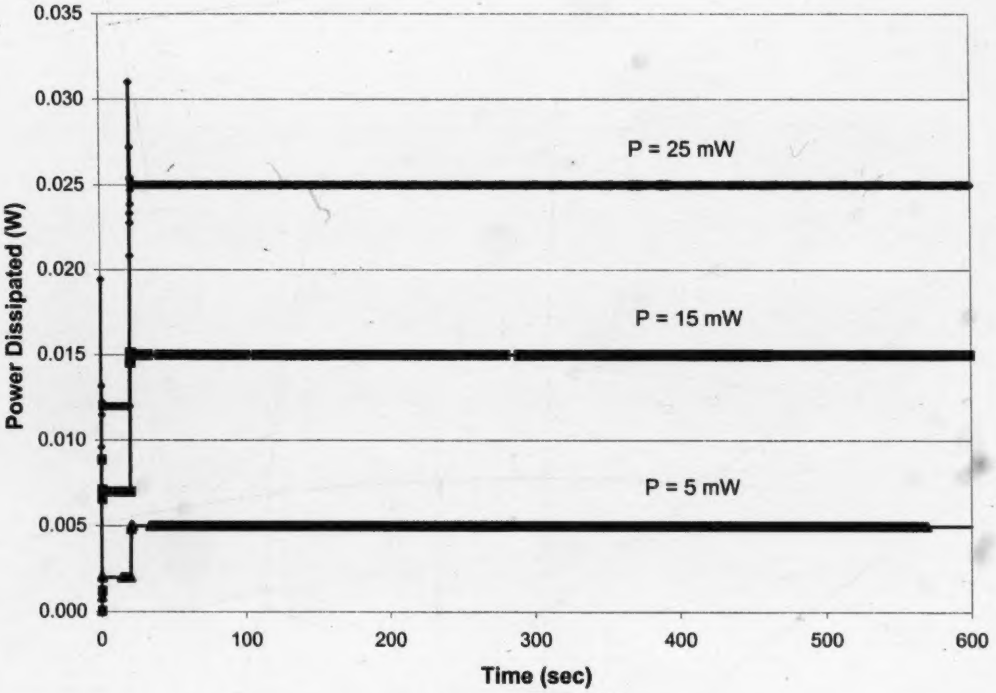

Figure 4.10 Test of constant power system operating at different powers

4.3.2 Test of experiment control unit

The Experiment Control System has been tested with the digital CPS supplying power to the micro-radiator and the data acquisition unit monitoring the output from the photodetector. Figure 4.8 shows the result under 40 mW operation power. Figure 4.11 magnifies the first 50 seconds of Figure 4.8 to show the details of the power and photodetector signals. When the electrical power is bigger than a threshold (about 25 mW in Figure 4.11), the micro-radiator starts to emit a detectable signal. The overshoot of the 15 mW power step briefly exceeds this threshold at about 3 seconds; the photodetector thus registers a short pulse signal. With the power overshoot and homing in to the 40 mW power level, starting at 22 seconds, the photodetector signal shows a similar but non-linear variation before the applied power becomes constant. The photodetector signal stays constant after the homing-in of the CPS. The process of power homing-in takes about six seconds at the 15 mW level and takes less than five seconds at the 40 mW level. The experiment control system has also been tested under other powers and pressures. The variation of the constant power is less than 0.2% after the homing-in while the variation of the photodetector signal is less than 3%.

From the various experiments described above, we can see the Melles Griot photodetector is reliable to measure the radiation from the micro-radiator and the output signal is linear to the intensity of incident light. A constant power supply is chosen instead of constant current or voltage power sources to keep the radiation from the micro-radiator constant at a fixed pressure. Therefore, the variation of the radiation from the micro-radiator is only due to the temperature change caused by the pressure change at a given constant power and will be used as the measurand of the surrounding gas pressure as described in the following chapter.

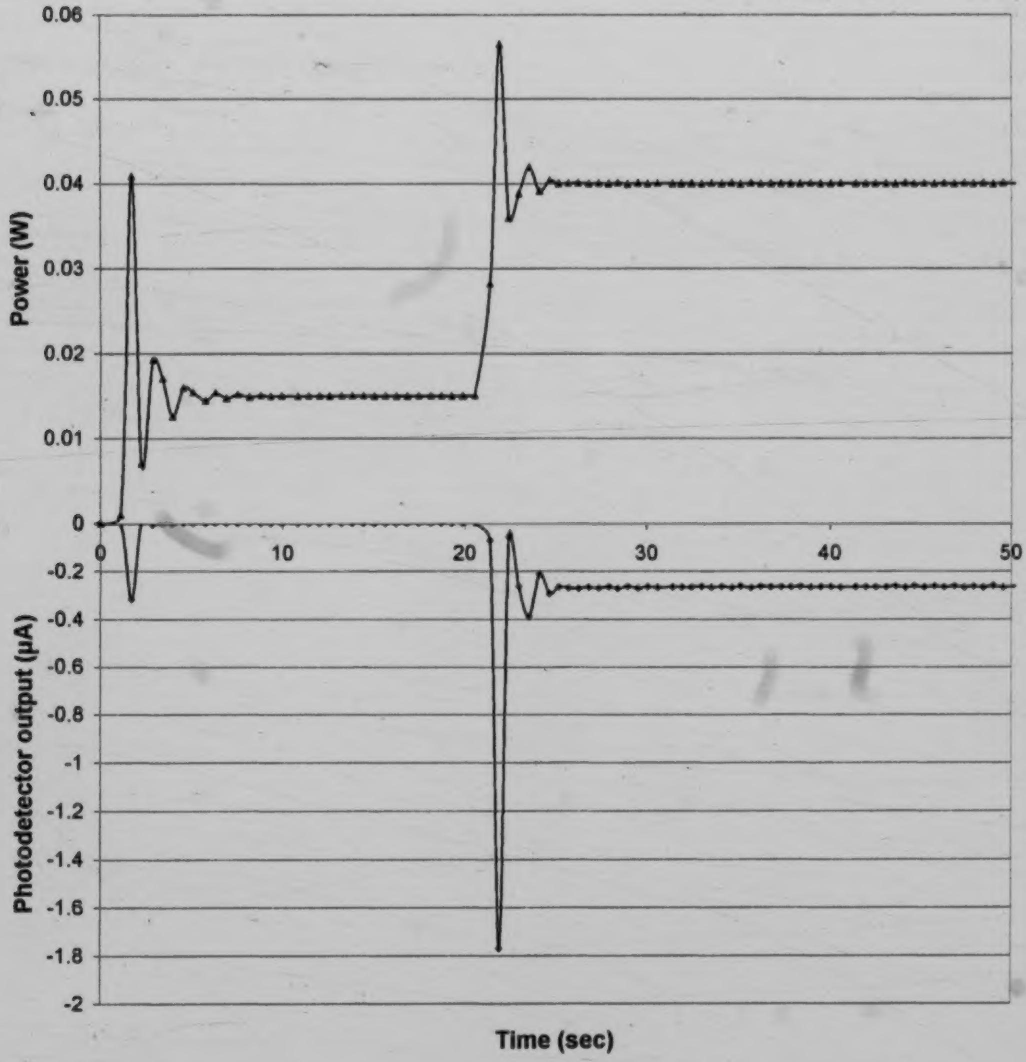

Figure 4.11 Magnified part of Figure 4.8 showing the details of photodetector and power signals

4.4 Measurement sensitivity

The radiation power from the micro-radiator can be evaluated using the photodetector. The output current of the photodetector I_d can be expressed by:

$$I_d(T) = \kappa \int_0^\infty \varepsilon(\lambda, T) \cdot E_{\lambda,b}(\lambda, T) \cdot R(\lambda) d\lambda \tag{4.4.1}$$

in which λ is the radiation wavelength, T the temperature and ε the emissivity of the micro-radiator, $E_{\lambda,b}$ is the emissive power of the micro-radiator and can be calculated by equation (1.4), $R(\lambda)$ is the responsitivity of the photodetector as shown in Figure 4.2 and κ is a proportionality constant to account for the detector - radiator geometry and configuration. We assume here that the emitter has a constant temperature T over its surface. The responsitivity of the photodetector is the current output of the photodetector when the photodetector is illuminated with incident light of 1 W at various wavelength. Since the National Institute of Standards and Technology (NIST) only provided the responsitivity data between 400 nm and 1100 nm, the responsitivities below 400 nm and above 1100 nm are extrapolated from the slope of the last two numbers at each end, as shown in Figure 4.12.

The emissivity of the micro-radiator ε is a function of both wavelength λ and temperature T, but a value of 0.8 is used here for simplicity of calculation. The feasibility of this assumption will be addressed later in Chapter 5. A value of 8% is used for the proportionality constant κ to account for the detector - radiator geometry and configuration, as shown in Figure 4.1.

The emissivity of the micro-radiator ε is a function of both wavelength λ and temperature T, but a value of 0.8 is used here for simplicity of calculation. The feasibility of this assumption will be addressed later in Chapter 5. A value of 8% is used for the proportionality constant κ to account for the detector - radiator geometry and configuration, as shown in Figure 4.1.

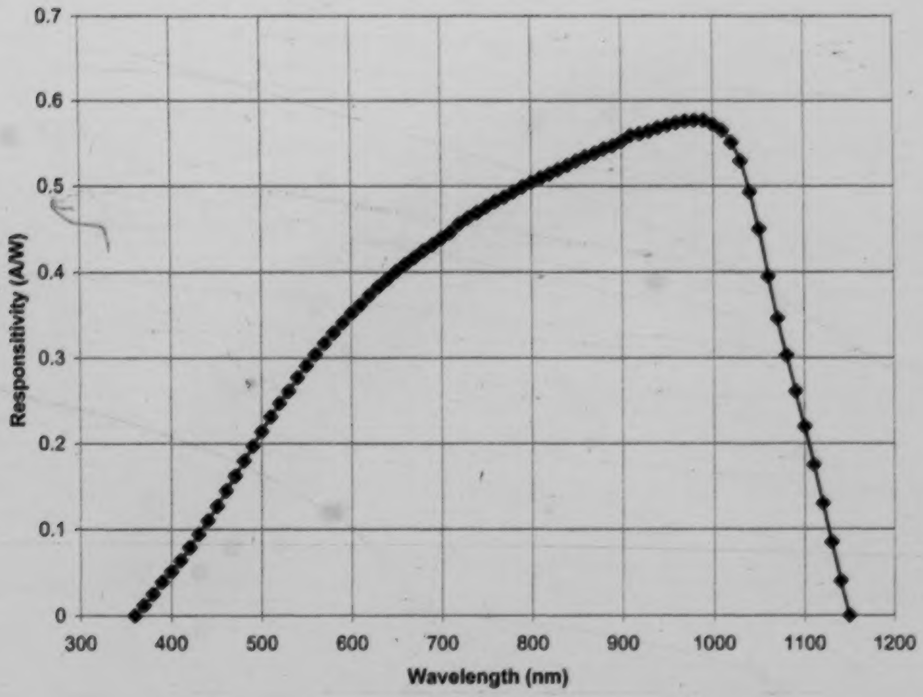

Figure 4.12 Extrapolated response of silicon photodetector 13 DAS 011/C

Figure 4.13 shows the integration results of equation (4.4.1) compared with the total emissive power, equation (1.5), and resistance variation, equation (1.3), of a typical micro-radiator at different temperatures. At a given temperature, the emissive power $E_{\lambda b}(\lambda, T)$ of the micro-radiator was calculated from 360 nm to 1150 nm in steps of $d\lambda =$ 10 nm using the Boltzmann distribution. Then the total signal detected by the photodetector was numerically integrated using rectangles, which calculates the sum of products $E_{\lambda b}(\lambda, T)$, $R(\lambda)$ and $d\lambda$. We felt that other numerical integration methods such as Simpson's rule or the trapezoidal rule were not necessary, as we were interested in working a qualitative comparison of the resistance, radiation and photodetector output as shown in Figure 4.13.

From Figure 4.13, we can see the output of the photodetector increases much more sharply with the temperature than the variation of total emissive power, which varies as T^4, and the output of the traditional Pirani gauge, which measures the resistance variation with temperature using equation (1.3). For a micro-radiator with 0.01 mm^2 surface area and a temperature change of ΔT = 1400-400=1000 K, the magnitude of the photodetector output signal changes by about 10^{10}, while the magnitude change of the total radiation changes by about 10^3 and the resistance change is less than 10. The dramatic increase of the photodetector output signal is due to the blackbody distribution not only increasing in absolute magnitude, but shifting more into the response region of the photodetector, which makes it the most sensitive detection method of the three compared in Figure 4.13.

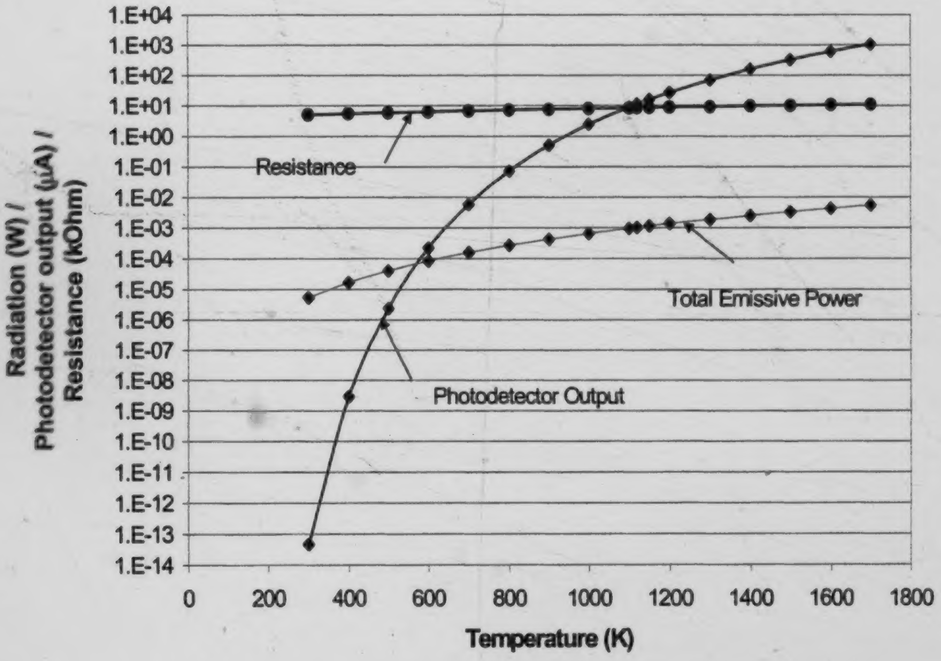

Figure 4.13 Comparison of the photodetector output with the total radiation and resistance of the micro-radiator as a function of temperature

From an analytic form of the photodetector output curve in Figure 4.13 and the curves in Figure 3.6, we can plot the photodetector output versus the gas pressure. Figure 4.14 shows the variation of photodetector output with the pressure of surrounding gas under two different input powers along with the temperature versus pressure curves as shown in Figure 3.6.

From Figure 4.14, we can see the sensitivity of the micro-radiator pressure sensor is different with different input powers. Higher input power leads to bigger sensitivity at the linear heat transfer region and it also shifts the pressure-sensitive region to higher values. A power-switching scheme based on this feature will be introduced in Chapter 6 to increase the sensitivity and measurement range of the micro-radiator. Photodetector output calculated in Figure 4.14 will also be compared with experimental results in Chapter 6.

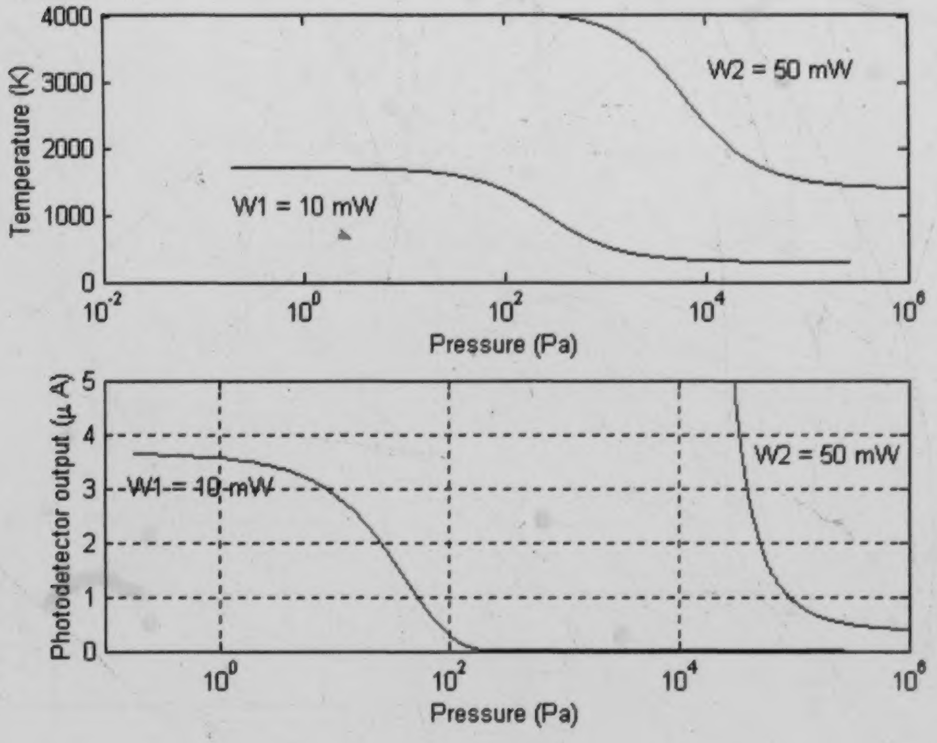

Figure 4.14 Micro-radiator temperature and photodetector output versus pressure operating at input powers of 10 and 50 mW

References:

[1] A. M. Robinson, "Mitel 1.5 μm CMOS Process: Characterization Measurements of the Polysilicon Layers for Use in a Micro-sensor", *Canadian Microelectronics Corporation Report*, IC95-06, 1995.

[2] J. A. Babcock, D. W. Feldbaumer and V. M. Mercier, "Polysilicon resistor trimming for packaged integrated circuits", *Tech. Dig., IEDM '93*, Washington, DC, 11 Dec. 1993, pp. 247-250.

[3] P. Haswell and A. M. Robinson, "Constant power testing system for polysilicon microresistor characterization measurements", *Meas. Sci. Technol.*, vol. 4, 1993, pp. 957-961.

[4] B. Hogg, P. Warkentin and R. Thurston, "Digital Constant Power System", CMPE 499 Project Report, Electrical Engineering Department, University of Alberta, April 1994.

Chapter 5

Device Characterization

The micro-radiator is characterized as an emitter in this chapter. Radiation from the micro-radiator, including radiation intensity, spectral and spatial distribution, is measured and the results are discussed.

A reliability study of polysilicon is also included in this chapter to find out the threshold operation power of the micro-radiator where the stability of the electrical characteristics starts to decay.

5.1 Micro-radiator radiation measurements

Figure 5.1 shows the experiment setup used to study the radiation from the micro-radiator. The micro-radiator is mounted on a ceramic 40-pin DIP (dual in-line package). The radiation is monitored with the photodetector. The incidence angle of the radiation to the photodetector is θ and ϕ is the azimuth angle of the photodetector. A large dynamic-range amplifier amplifies output from the photodetector and the Experiment Control System supplies a constant power to the micro-radiator and reads the amplified output of the photodetector.

5.1.1 Micro-radiator radiation response with input power

The radiation from the micro-radiator was measured at one atmosphere under different input powers, as shown in Figure 5.2. The photodetector was 2.5 cm away from the micro-radiator and directly above it ($\theta = 0°$). Constant power input up to 60 mW was used to heat the micro-radiator; radiation was visible at about 30 mW input at atmospheric pressure.

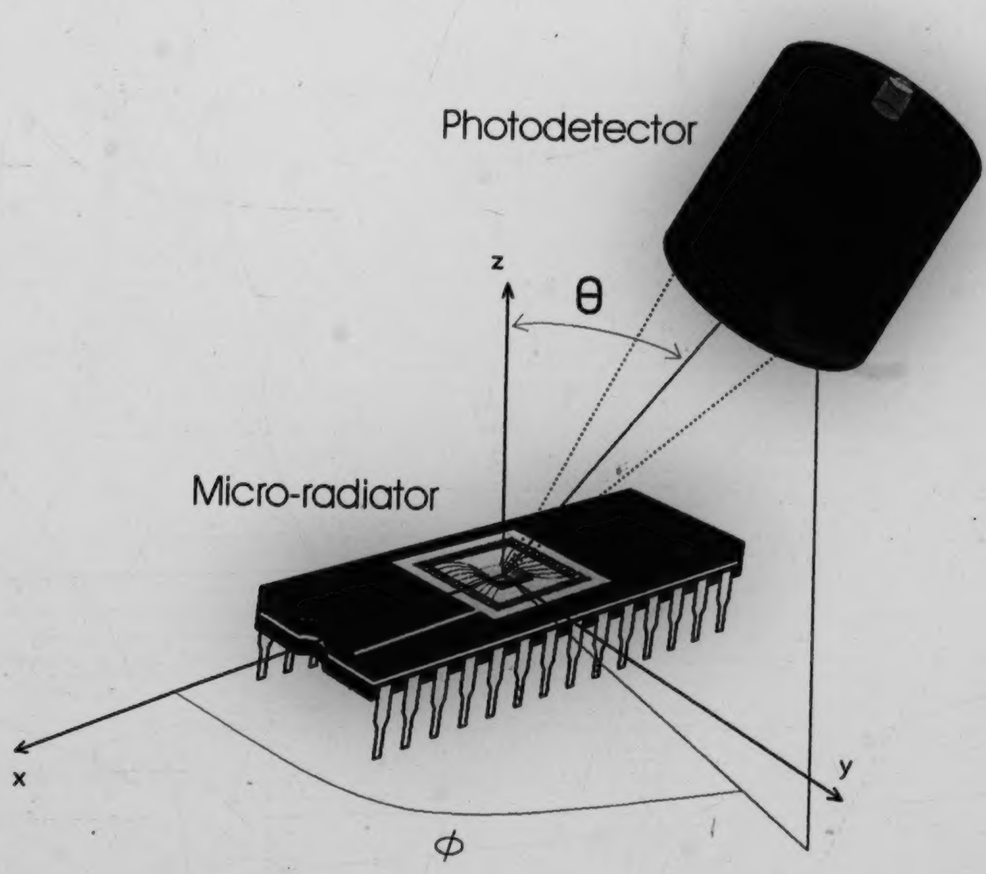

Figure 5.1 Experiment setup for radiation measurement

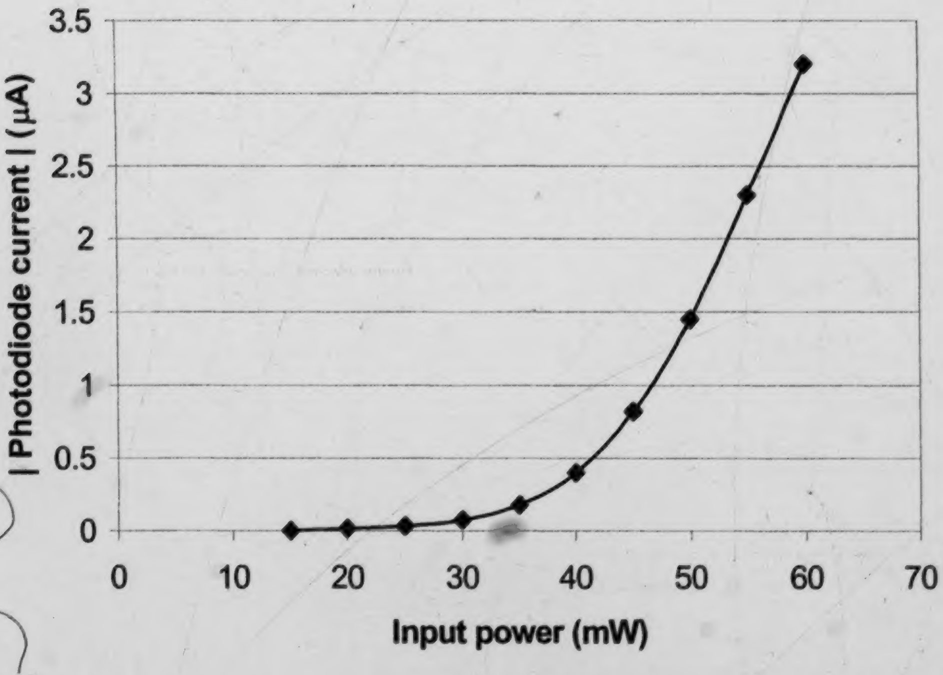

Figure 5.2 Photodetector signal versus the micro-radiator input power ($\theta = 0$)

From Figure 5.2 we can see the relationship between the radiation from the micro-radiator and the input constant power is a polynomial curve. After about 25 mW, the photodetector signal varies rapidly with the constant power input. Experiment data above 60 mW are not collected because the excessive heat will burn out the micro-radiator.

5.1.2 Micro-radiator radiation spectral analysis

The micro-radiator was treated as a gray body with an emissivity of 0.8 in Chapter 4 to calculate the photodetector output. In order to compare the radiation from the micro-radiator with the blackbody radiation, a spectral measurement is performed by inserting a set of filters between the micro-radiator and a HgCdTe infrared photodetector. The HgCdTe photodetector is fabricated by Electro-Optical Systems, Inc. (Model: MCT16), with a sensitive range between 1 μm and about 18 μm. Figure 5.3 shows a schematic of the experiment setup. The input power of the micro-radiator was 50 mW. Radiation from it was collimated and focused using ellipsoidal reflectors and then detected by the HgCdTe photodetector after intensity modulation. A lock-in amplifier amplified the output of the photodetector. The filter characteristics are summarized in Table 5.1.

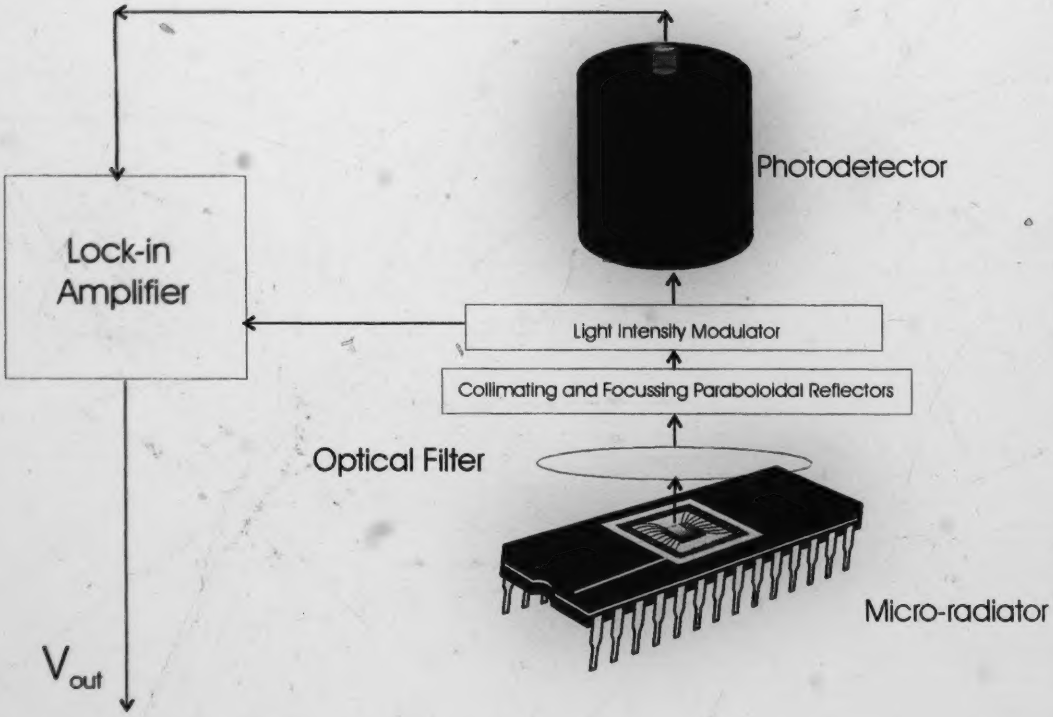
Photodetector
Lock-in Amplifier
Light Intensity Modulator
Collimating and Focussing Paraboloidal Reflectors
Optical Filter
Micro-radiator
V_{out}

Figure 5.3 Apparatus used for radiation spectral analysis

Table 5.1 Optical filters and lock-in amplifier output

Filter Type	Center Wavelength (μm)	Bandwidth or Transmission range (μm)	Lock-in Amplifier Output (mV)	Relative spectral intensity
BP-1230-1580	1.40	0.35	0.7	0.18
LP-1000	1.47	0.94	10.7	0.90
LP-1600	2.07	0.94	13.5	1.00
LP-3000	3.72	1.44	10.5	0.33
BP-3900-110	3.95	0.11	1.4	0.55
SP-6000	4.97	2.06	8.4	0.17
SP-8750	7.55	2.4	7.2	0.07
LP-6000	7.99	3.98	9.2	0.035
BP-10500-385	10.69	0.385	0.3	0.12
LP-10800	14.67	7.74	4.2	0.01

- All filters are fabricated by Spectrogon Inc.

The relative spectral intensity at the center wavelength of each filter was calculated by dividing the photodetector output by the transmission of each filter and the response of the photodetector at that wavelength. The transmission of each filter is the product of the bandwidth of the filter and the average transmission rate. Please refer to Spectrogon Inc. homepage (http://www.spectrogon.com) for transmission curves of each filter for details. The resulting spectral radiation is normalized and plotted in Figure 5.4. Experimental data are least-squares fitted to a blackbody radiation curve.

The temperature of the least-squares-fitted curve is 1521 K and the corresponding peak of the emission can be calculated using Wien's Displacement Law [1]:

$$\lambda_{\max} = 2897.8(\mu m \cdot K)/T = 1.9\mu m \qquad (5.1.1)$$

Experimental data shows a good agreement with the blackbody radiation curve in Figure 5.4. Therefore, the assumption of a constant emissivity of micro-radiator surface used in Chapter 4 is feasible. The data divergence from the blackbody curve at 1.5 μm, 4 μm and 10.7 μm is possibly due to an interference effect of the silicon nitride layer on the micro-radiator surface [2]. The temperature of the fitted blackbody curve is roughly in the same range as the temperature derived from measured resistance in Section 5.2.

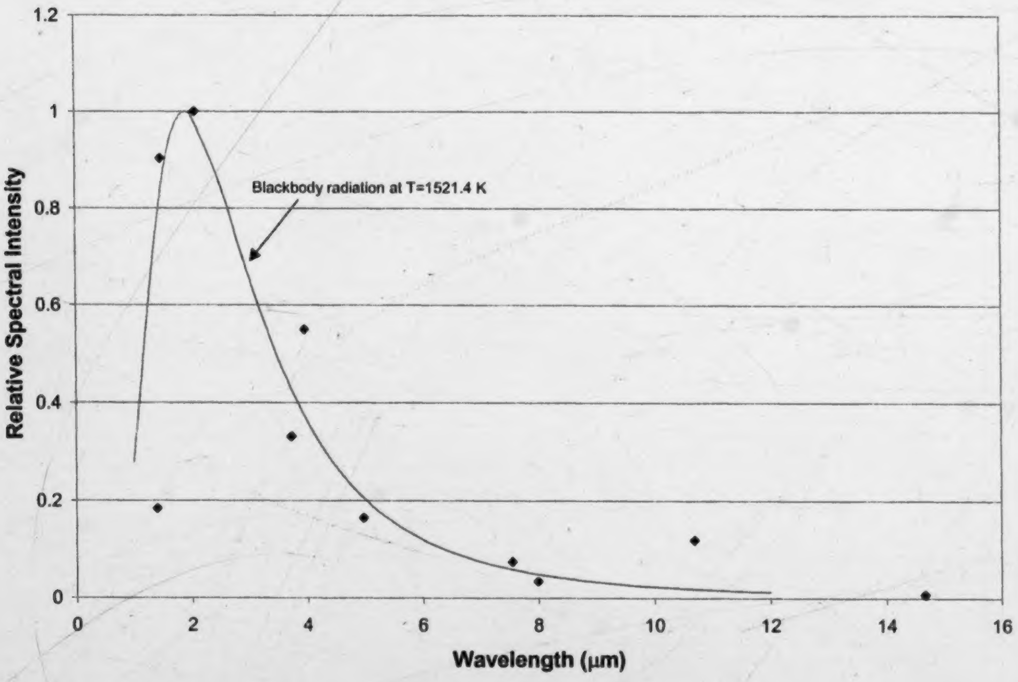

Figure 5.4 Normalized spectral distribution of a micro-radiator with 50 mW input power. The points are measured values.

Optical spectral radiation below 1.2 μm was also measured with an Ocean Optics S2000 Miniature Fiber Optic Spectrometer calibrated with a tungsten filament lamp [3]. The sensitive range of the spectrometer is from 300 nm to 1200 nm. Figure 5.5 shows the experimental configuration. The micro-radiator was placed 2 mm away from the pinhole (diameter: 200 micron) of the optical fiber. Light from the micro-radiator enters the optical fiber and is efficiently transmitted to the spectrometer, which is the middle of Figure 5.5. Once in the spectrometer, a spherical mirror collimates the divergent light emerging from the optical fiber. Then a plane grating diffracts the collimated light and a second spherical mirror focuses the resulting diffracted light. An image of the spectrum is projected onto a 1-dimensional linear CCD array, and the data is transferred to a computer through an A/D card.

Three different constant powers from 35 mW to 70 mW were used to successively heat the micro-radiator to incandescence. Typical results from 650 nm to 1200 nm are shown in Figure 5.6. The radiation below 600 nm is very small and barely detectable with the grating provided by the Ocean Optics S2000 spectrometer.

The spectral distribution measured by the Ocean Optic spectrometer is far from a gray body emission. This is mainly due to the wavelength range measured by the Ocean Optic spectrometer is only a small part of the micro-radiator emission. From Figure 5.4 we can see the radiation from micro-radiator is mainly in the infra-red region. Therefore, peaks around 930 nm and minimum radiance around 650 nm and at 1170 nm shown in Figure 5.6 is due to the interference effects of the silicon nitride film.

The refractive index of silicon nitride, *n*, is 1.98. Since the minimum radiance point around 650 nm is not accurate, the wavelength difference between minimum radiance was calculated by:

$$\Delta\lambda = 2\times(1170-930) = 480nm \tag{5.1.1}$$

The film thickness of the interference layer can be calculated by:

$$d\_film = \lambda_{\max}{}^2 / 2n\Delta\lambda = 455nm \tag{5.1.2}$$

This result agrees well with the thickness of the silicon nitride layer on top of the micro-radiator surface.

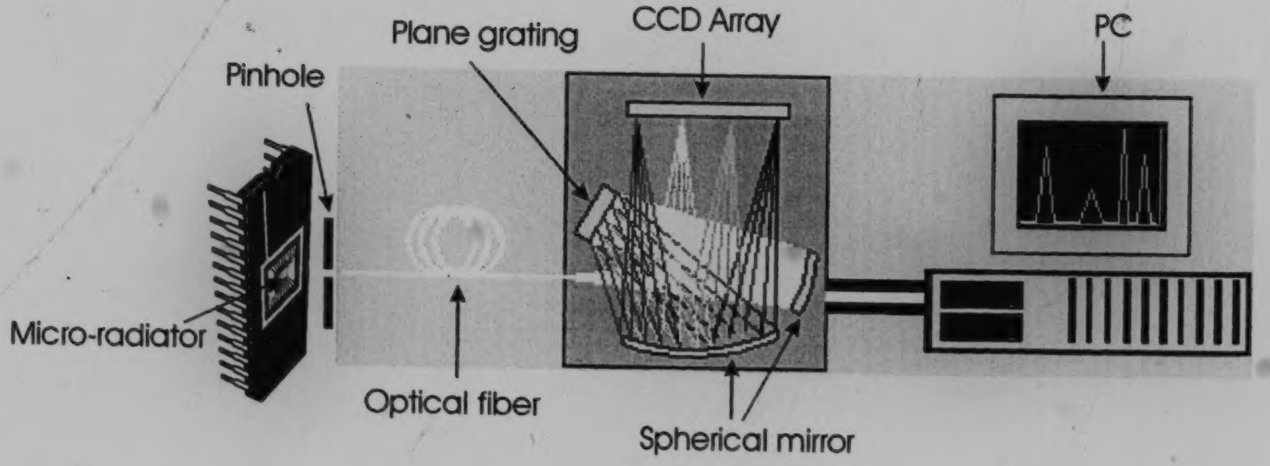

Figure 5.5 Spectral emissive power analysis experiment setup

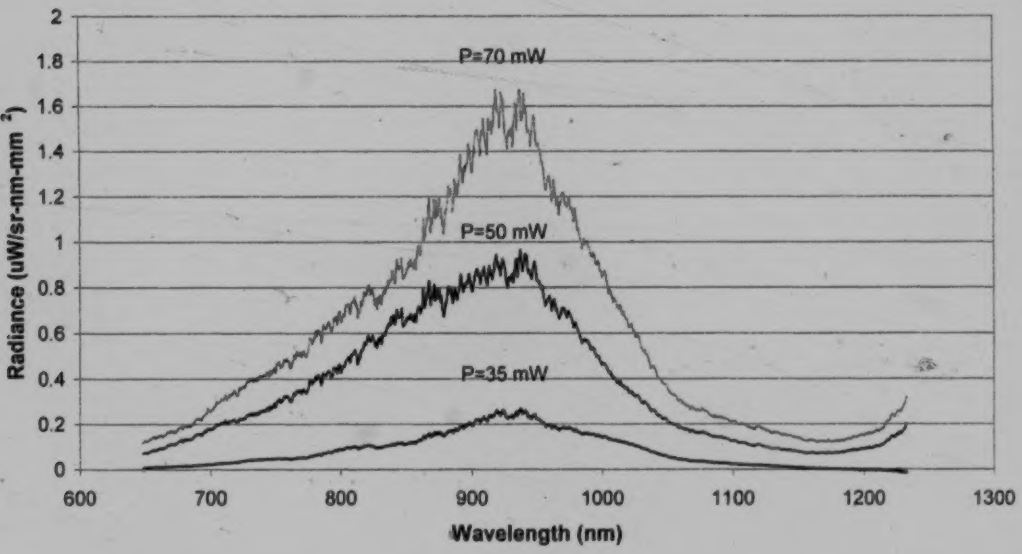

Figure 5.6 Spectral emissive power of the micro-radiator from 650 nm to 1200 nm

5.1.3 Micro-radiator radiation spatial distribution

Figure 5.7 shows the radiant intensity distribution as a function of the incidence angle θ, measured from the perpendicular to the plane of the micro-radiator as shown in Figure 5.1. The measurement was done by varying the incident angle θbetween 0° and 90°. The distance between the photodetector and the micro-radiator is constant about 5 cm. The azimuth angle of the photodetector ϕ was varied from 0° to 360°. The experimental results are independent of ϕ and closely follows Lambert's cosine law.

Lambert's cosine law is a mathematical statement that the radiance of certain idealized optical sources is directly proportional to the cosine of the angle with respect to the direction of maximum radiance, from which the source is viewed [4]. Lambert's cosine law is plotted as a series of "+"s in Figure 5.7.

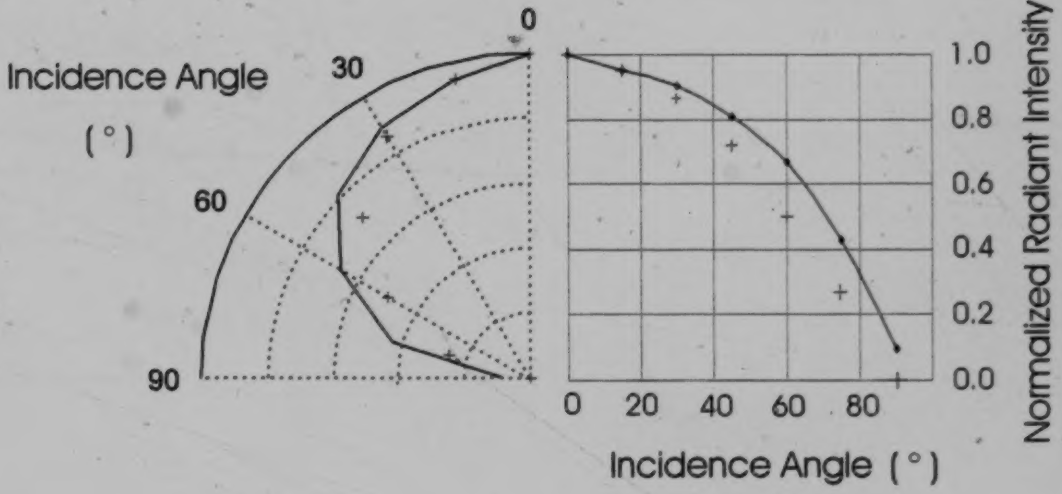

Figure 5.7 Normalized angular radiant intensity of a micro-radiator as a function of the polar angle θ

5.2 Reliability study of polysilicon

Reliability is one of the most important characteristics of a sensor, and the reliability of polysilicon film has been extensively studied in the past decade [5-9]. Research results proved that high thermal isolation with micromachining could result in high resistor temperature, leading to significant resistance drifts or even failure of the device. In this section, the reliability of the micro-radiator is studied using the Keithley Source Measure Unit.

Figure 5.8 (a) shows typical voltage current characteristics of the micro-radiator at atmospheric pressure. The data were obtained with a series of current steps from 0 to 2 mA applied to the micro-radiator and measuring the voltage at the same time. The step of the input current is 0.1 mA. Experimental data from the first sweep (curve marked "Sweep 1") was slightly above the traces obtained with the following sweeps (curves marked with "Sweep 2-6"). The repeatability of the voltage-current curves after the initial sweep is very good and the data were least square fitted to a polynomial equation shown in the figure.

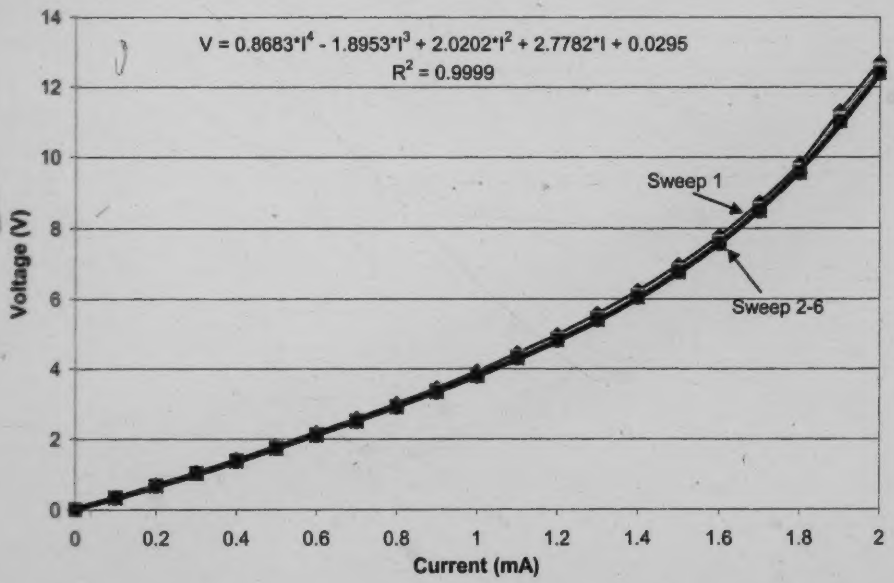

Figure 5.8 (a) Voltage-current characteristics of micro-radiator for a current from 0 to 2 mA

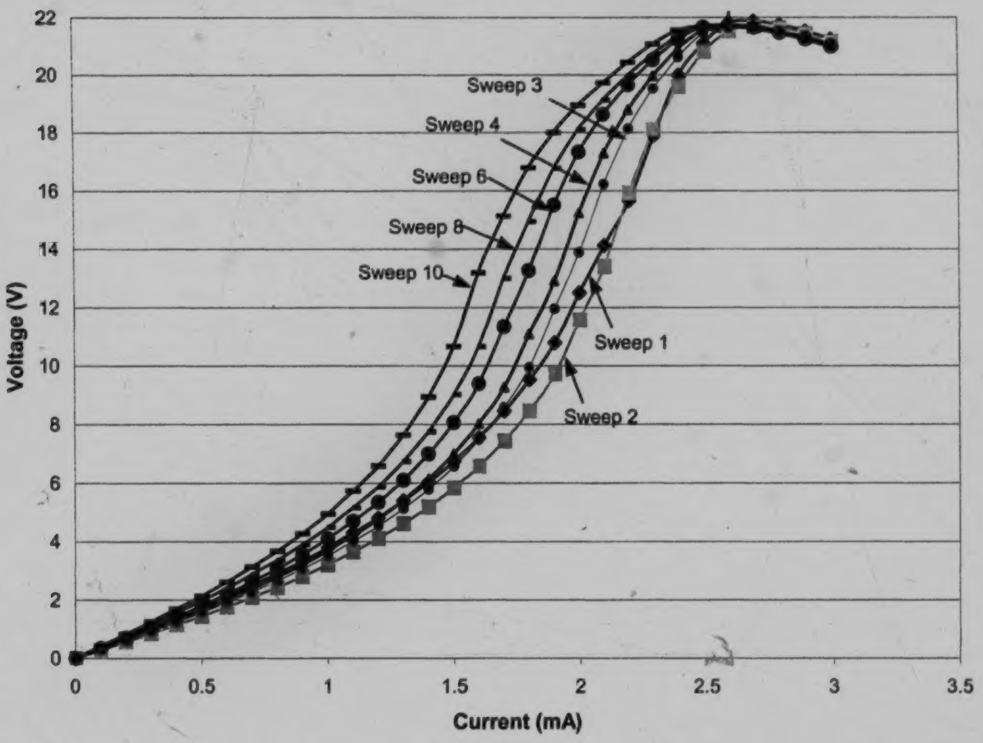

Figure 5.8 (b) Voltage-Current characteristics of micro-radiator for a current from 0 to 3 mA

If we increase the maximum current to 3 mA on the same resistor, the shape of the voltage-current characteristic curves change, and are shown in Figure 5.8 (b). The input current is started from 0 to 3 mA in steps of 0.1 mA. At relatively low current, the voltage across the micro-radiator increases with increasing current due to the positive temperature coefficient of the polysilicon. After the current reaches 2.6 mA, which corresponds to a power about 56 mW, the voltage starts to decrease, similar to what was observed by others [5,9,10,11].

After the first sweep up to 3 mA, the voltage-current characteristic curves start to drift from their original trace. For currents below 2.2 mA on the second sweep, the measured voltages are smaller than the ones obtained from the first sweep and are approximately the same as the first sweep after 2.2 mA. This is a general behavior observed on several micro-radiators, although the point where two traces cross may be different than 2.2 mA. The voltage-current characteristic curves drift to the left from the third sweep and keep drifting in the same direction on the following traces. Sweeps 5, 7, and 9 are not shown in Figure 5.8 (b).

The resistance of the micro-radiator as a function of input current is plotted in Figure 5.9 (a). The data are taken from sweeps 1, 4, 6, and 10 shown in Figure 5.8 (b). A maximum in each curve occurs, after which the resistance decreases.The point where the resistance is maximum moves to the left with sweep number, similar to what was observed in Figure 5.8 (b).

The resistance of polysilicon starts to decrease after a threshold of 2.6 mA in air, which corresponds to a threshold power of 56 mW and a threshold current density of 1.7 × 10^5 A/cm^2.

Resistance of the micro-radiator was also plotted as a function of input power in Figure 5.9 (b). The input power was calculated by $W = I^2R$ and the average temperature of the micro-radiator can be estimated with the relationship between resistance R and temperature T:

$$R(T) = R_0[1 + \alpha_T(T - T_0) + \beta_T(T - T_0)^2 + \ldots] \tag{5.2.1}$$

where α_T is the temperature coefficient of resistance and equal to 1.09×10^{-3}, $\beta_T = 7.4 \times 10^{-7}$ [9], R_0 is the room temperature resistance, and T_0 is room temperature (20°C). The room temperature resistance R_0 changes after each sweep, as shown in Figure 5.9 (a), changing from about 3.5 kΩ before the first sweep to about 4.2 kΩ after sweep 10. This is only a crude calculation because values of α and β were obtained in [9] experimentally in the temperature range from 20 °C to 400 °C, and we are using them well beyond this range. The temperature of the micro-radiator at different input powers can be calculated by solving equation (5.2.1). The calculated temperature versus input powers for the first and last sweep is shown in Figure 5.9 (c), where we used the appropriate value of R_0 for each sweep. The maximum temperatures for sweep 1 and sweep 10 are about 1100 K and 1200 K. The fact that temperature is not the same for a given input power except at low power (< 5 mW) on each sweep means that α and β have changed after each sweep. The temperature calculated after these maximum points are not valid, because equation (5.2.1) is no longer valid at high temperatures. Other effects and processes are occurring which equation (5.2.1) is incapable of describing.

This resistance decrease occurs because the increase in temperature at increasing currents leads to significant reduction in the grain boundary barrier potential and possibly leads to formation of narrow filaments of molten silicon creating low resistivity paths for current flow [5]. Movement of grain boundaries leading to grain growth or re-crystallization, which subsequently lead to lower resistivity of thin polycrystalline film, is also possible [6]. Electro-migration has also been observed with high gain Optical Beam Induced Current imaging at high temperature as reported in [8]. Catastrophic failure has been observed if the polysilicon micro-radiator is heated under excessively high power for very long time or after many pulses of heating cycle. In this project, the working condition of polysilicon micro-radiator is controlled below the threshold power of 56 mW in air to avoid the resistance drifts, and to extend the lifetime of the devices.

The above experiments have also been performed at a pressure of 50 mTorr. The general behavior and the shape of the resistance versus the input current curves remain the same, but the threshold current decreases to 1.1 mA and the threshold power decreases to about 10 mW.

In conclusion, the polysilicon micro-radiator is not electrically stable at high temperature. Many complicated processes occur under high input power which we cannot describe or understand well. The best we can do is to operate the micro-radiator at as low a power as will give us a reasonable signal and keep the power constant.

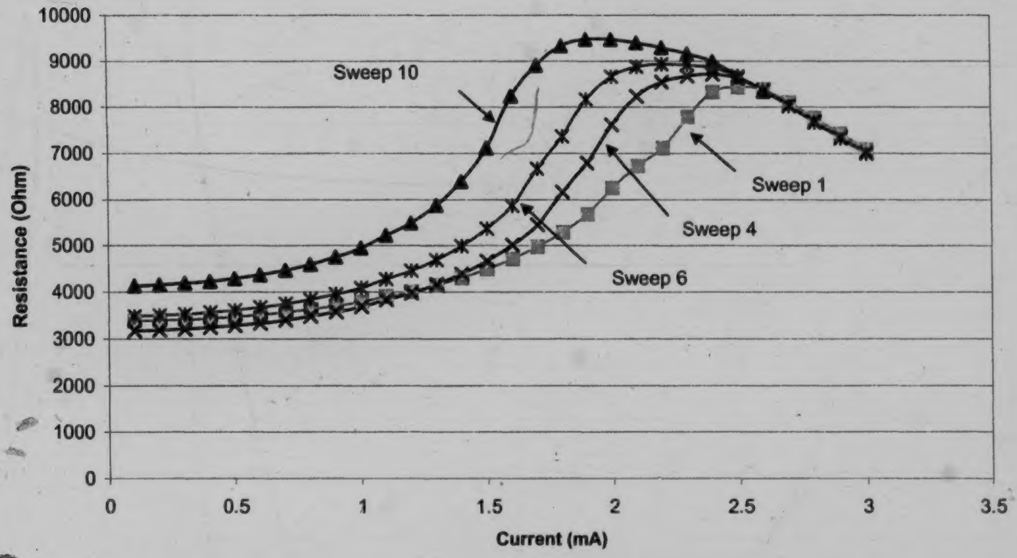

Figure 5.9 (a) Resistance of micro-radiator as a function of input current-from sweep 1,4,6 and 10 of Figure 5.8 (b)

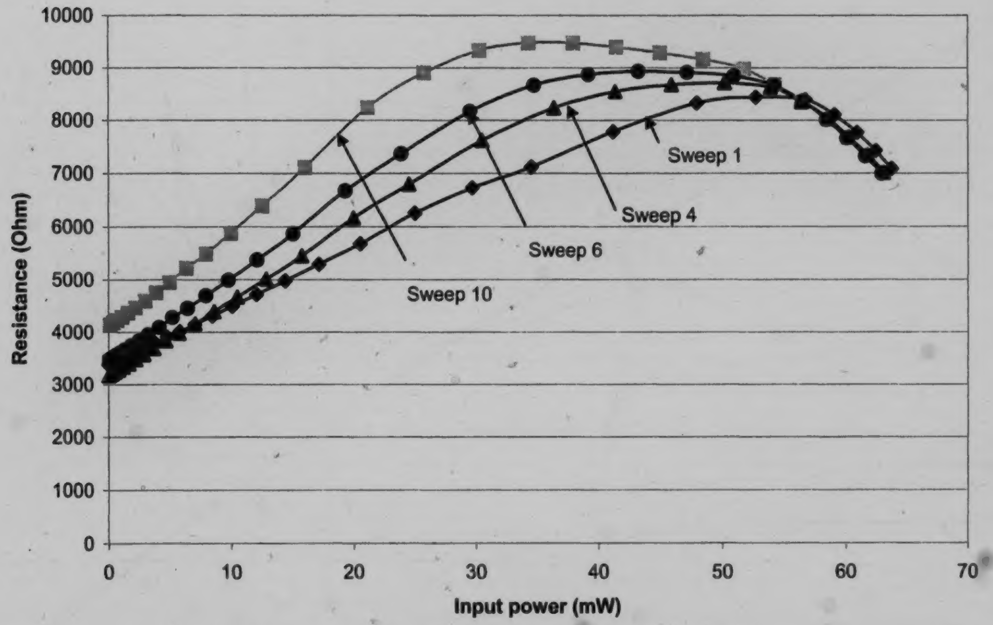

Figure 5.9 (b) Resistance of micro-radiator as a function of input power

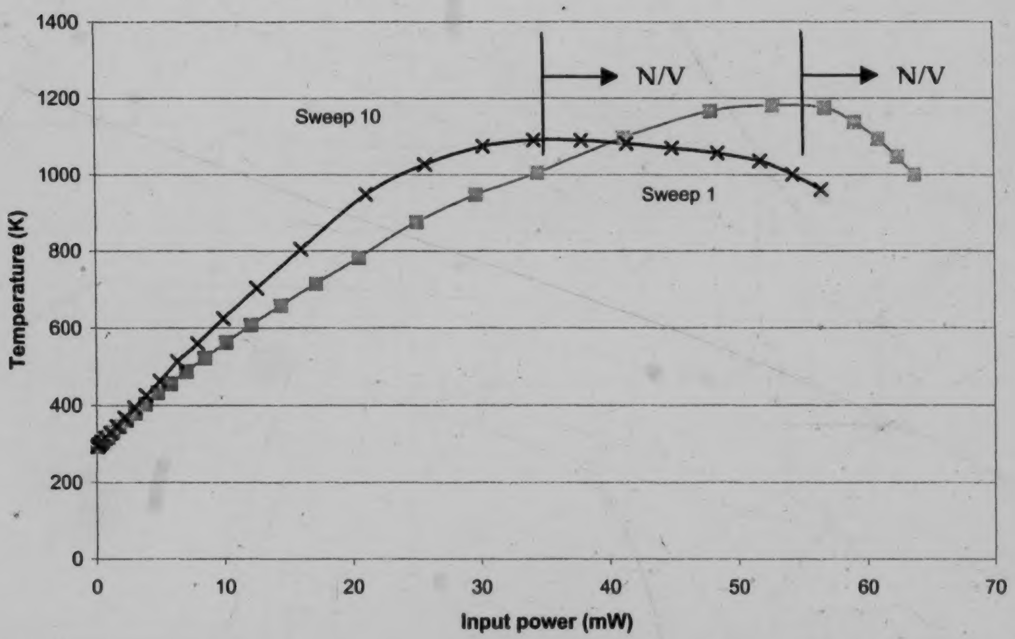

Figure 5.9 (c) Temperature versus input power curves for the first and last sweep (N/V: Not Valid)

References:

[1] Frank P. Incropera, David P. DeWitt, Introduction to Heat Transfer, John Wiley & Sons, Inc., New York, 1985, p. 610.

[2] C. H. Mastrangelo, J. H. Yeh, and R. S. Muller, "Electrical and optical characteristics of vacuum-sealed polysilicon microlamps", IEEE Trans. Electron Devices, vol. 39, 1992, pp. 1363-1375.

[3] http://www.oceanoptics.com/specanim.asp

[4] H. O. McMahon, "Thermal radiation from partially transparent reflecting bodies", Journal of the Optical Society of America, Vol. 40, No. 6, June 1950, pp. 376-380.

[5] N. R. Swart and A. Nathan, "Reliability study of polysilicon for microhotplates", *Solid-State Sensor and Actuator Workshop*, Hilton Head, South Carolina, June 13-16, 1994, pp. 119-122.

[6] H. Akimori, N. Owada, T. Taneoka, and H. Uda, "Reliability study of polycrystalline silicon thin film resistors used in LSI under thermal and electrical stress", *Proc. IEEE Int. Reliability Phys. Symp.*, 1990, pp. 276-280.

[7] M. Parameswaran, A. M. Robinson, D. L. Blackburn, M. Gaitan, and J. Geist, "Micromachined thermal radiation emitter from a commercial CMOS process", IEEE Electron Device Letts., vol. 12, 1991, pp. 57-59.

[8] E. I. Cole, Jr., J. S. Suehle, K. A. Peterson, P. Chaparala, A. N. Campbell, E. S. Snyder, and D. G. Pierce, "OBIC analysis of stressed, thermally-isolated polysilicon resistors", *Proc. IEEE Int. Reliability Phys. Symp.*, 1995, pp. 234-243.

[9] A. M. Robinson, "Mitel 1.5 µm CMOS Process: Characterization Measurements of the Polysilicon Layers for Use in a Micro-sensor", *Canadian Microelectronics Corporation Report*, IC95-06, Kingston, ON, 1995.

[10] D. W. Greve, "Programming mechanism of polysilicon resistor fuses", IEEE Trans. Electron Devices, vol. 29, 1982, pp. 719-724.

[11] K. Ramkumar and M. Satyam, "Negative-resistance characteristics of polycrystalline silicon resitors", J. Appl. Phys., vol. 62, 1987, p. 174-176.

Chapter 6

Vacuum Pressure Sensing and Power-Switching Scheme

The micro-radiator is tested under different pressures in this chapter and a power-switching scheme is introduced to increase the sensitivity of the measurement and lifetime of the device.

6.1 Micro-radiator radiation response with pressure

Radiation from the micro-radiator has been monitored with a photodetector under different pressures. Figure 6.1 shows the variation of the photodetector signal versus the pressure operating the micro-radiator at a constant power of 10 mW. A piecewise-fitted curve from Excel indicates the first measurement cycle and the data from the following seven cycles are indicated by the corresponding symbols. Each experimental data was taken after the pressure inside the experiment chamber has been stabilized and each pressure measurement cycle took about an hour. The repeatability of the experimental data is good. Figure 6.2 compares the experimental results with the theoretical simulations obtained in Chapter 4 (see Figure 4.14). Experiment and simulation are in reasonable agreement.

The curves shown in Figure 6.1 and Figure 6.2 demonstrate the typical shape for a conventional thermal conductivity pressure gauge [1], but with a much more sensitive output. Above 1000 Pa, the thermal conductivity of the gas is independent of the pressure, and the element temperature and therefore the radiation is almost constant. Below 1 Pa, the radiation is again less dependent on the pressure because heat loss by conduction through the gas becomes significantly less than the radiation heat loss and conduction heat loss through the support arms, both of which are approximately pressure-independent. In the region between 1 Pa and 1000 Pa, the gas conduction heat loss tends to dominate and the temperature, hence the photodetector signal, is a strong function of the gas pressure. The dynamic range of the output signal in Figure 6.1 varies from 0.2 μA to about 3.4 μA in the pressure range from 1 Pa to about 300 Pa, which corresponds to a change of 16 times the output at 1 Pa, while a standard Pirani gauge and a CMOS Pirani gauge both change only about 3 % in this range [1].

As discussed in Chapter 4, higher input power shifts the micro-radiator emission more into the sensitive range of the photodetector. The response curve shown in Figure 6.1 and 6.2 shifts to a different pressure range in Figure 6.3 when the constant power input is increased to 20 mW.

It should be noted that the constant power delivered to the polysilicon micro-radiator necessary to produce a particular detectable photodetector signal increases as the pressure increases. A power of 5 mW at 10^{-3} Pa increases to about 25 mW at one atmosphere due to the increase of cooling by the surrounding gas. Figure 6.3 shows the photodetector signal versus gas pressure at two different constant powers. The 10 mW curve has a sensitive pressure range from 1 Pa to about 10^3 Pa. The 20 mW curve has a sensitive range from one atmosphere (~10^5 Pa) down to about 10^3 Pa. Operating the micro-radiator at 20 mW below 10^3 Pa reduces the lifetime of the device due to excessive heating. The difference between the experimental data and the analytical simulation is probably due to such factors as the simplification of the thermal model, constant emissivity used and instability of polysilicon under high temperature.

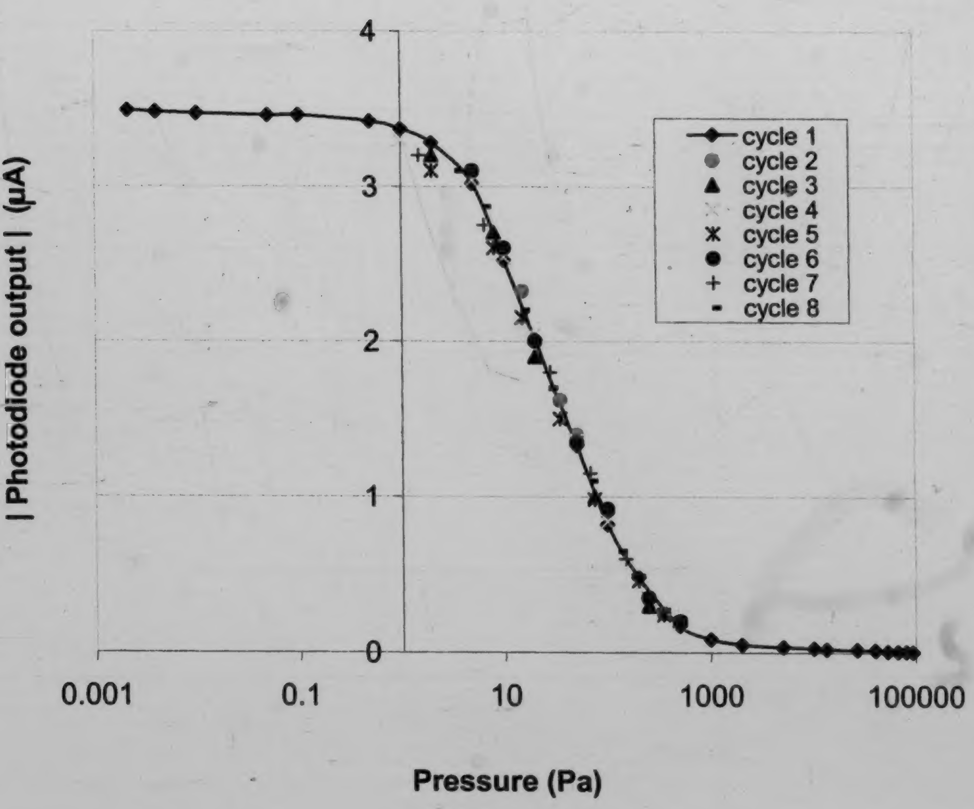

Figure 6.1 Photodetector signal versus pressure operating at a constant power of 10 mW

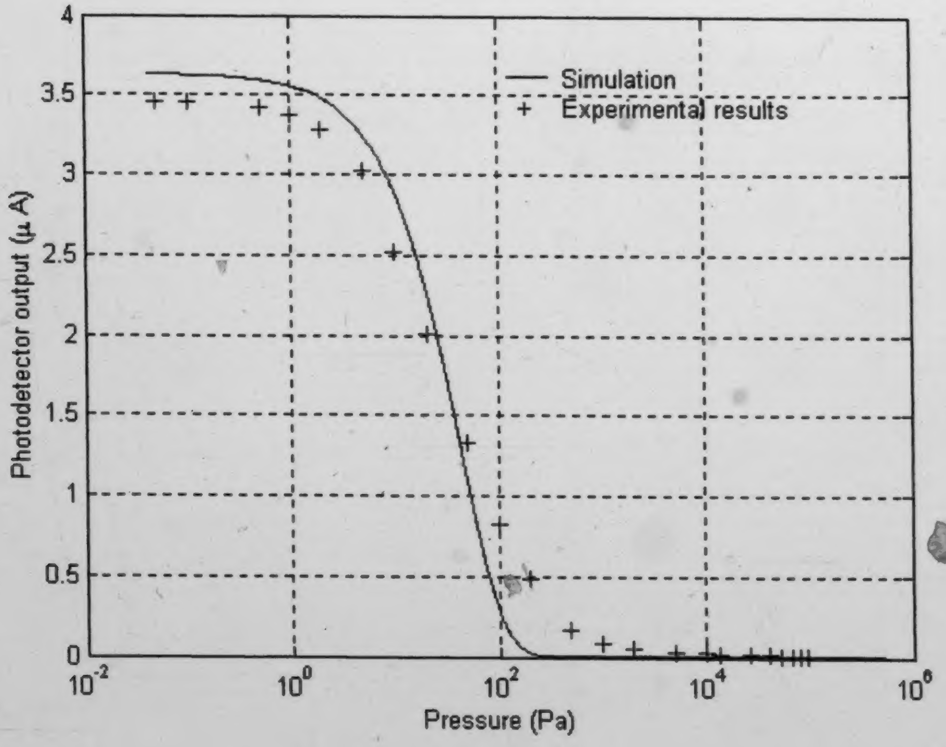

Figure 6.2 Analytical simulation compared with experimental resutls

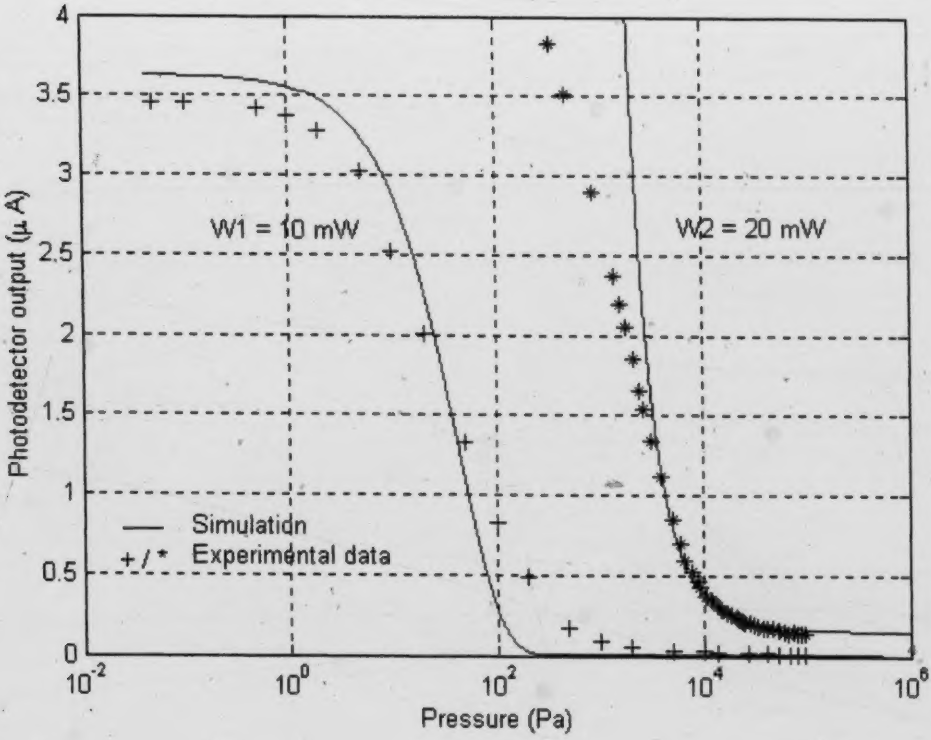

Figure 6.3 Analytical simulation and experimental results showing photodetector signal versus pressure operating at constant powers of 10 and 20 mW

6.2 Power-switching scheme

Because polysilicon is electrically unstable at high temperature, as discussed in Chapter 5, and the sensitivity of the photodetector signal varies rapidly with emitter temperature, it is advisable to constrain the photodetector output to a small range at the most sensitive response region and where the temperature is not too high. From Figure 6.3, we can see the sensitivity of the measurement can be increased over a larger pressure range by manipulating the constant power applied to the polysilicon micro-radiator.

The sensitive pressure range can be extended to 10^{-3} Pa by the same mechanism with a different photodetector signal sensitive range. Large numbers of experimental data were not collected in the pressure range around 10^{-3} Pa due to the fact that the overshooting of the constant power system can damage the micro-radiator at that pressure, while it might not be a problem at a higher pressure. An input power of 2 mW at 10^{-3} Pa is enough to provide a sensitive photodetector signal (not included in Figure 6.4). Calibration of the micro-radiator was mainly focused in the pressure range from 0.1 Pa to one atmosphere.

Figure 6.4 shows such a power-switching scheme in the pressure range from about 0.1 Pa to one atmosphere. Seven different levels of constant power of 7 mW, 10 mW, 14 mW, 20 mW, 27 mW, 36 mW and 46 mW were used to achieve a larger dynamic range if the output of the photodetector signal is constrained to vary between 1 μA to 3 μA. The darker vertical straight lines in Figure 6.4 indicate the automatic power switching process.

The conceptual diagram of a possible such power manipulation circuit is shown in Figure 6.5. The photodetector signal is compared to two thresholds *High Threshold* and *Low Threshold* by two comparators *C1* and *C2*. The results from these two comparators are inputs to a JK flip-flop. Table 6.1 shows the truth table of the J-K flip-flop. When the photodetector signal is higher than the *High Threshold*, the output from comparator *C1* sets the JK flip-flop and the output from the flip-flop is sent back to the experimental control system to switch the power input to a lower level. When the photodetector signal is lower than the *Low Threshold*, the output from comparator *C2* resets the JK flip-flop and the output from the flip-flop is sent back to the control system to switch the power input to a higher level. On each different power level, a different calibration equation is used to output the measured pressure according to the detected photodetector signal.

Table 6.1 J-K flip-flop truth table

J	K	Output Q
0	1	0
1	0	1
0	0	No change
1	1	Toggle

For any point (e.g. I_d on the 7 mW curve) on the straight-lines plotted in Figure 6.4, we have:

$$y = y_0 + k(x - x_0) \tag{6.2.1}$$

in which k is the slope of the straight line, x_0, y_0, x and y are as shown in Figure 6.4. Therefore, the photodetector output on the straight-line plots can be represented by:

$$I_d = A + k(\log_{10} p - \log_{10} B) \tag{6.2.2}$$

where A is the photodetector output at the lower end of the linear output range (ie. 1 μA for Figure 6.4), B is the corresponding pressure at that point and p is the pressure to be measured. The slope of each curve, k, can be determined from the pressures at 1 μA and 3 μA. Table 6.2 lists the values of A, k and B at each input power level obtained from Figure 6.4.

The relationships between parameters k, B and the power supplied to the micro-radiator are plotted in Figure 6.6 and 6.7 and data are least-square fitted to polynomial curves. Therefore, the parameters k and B under an arbitrary power can be obtained and the pressure can be calculated from the photodetector output using equation (6.2.2).

Table 6.2 Parameter table for Figure 6.4

Power (mW)	**A (μA)**	**K**	**B (Pa)**
7	1	-1.45	5
10	1	-1.66	80
14	1	-2.00	800
20	1	-2.74	4300
27	1	-2.95	20000
36	1	-5.03	50000
46	1	-7.83	90000

However, the implementation of the above power-switching scheme can be very time consuming and is not included in this thesis. For each device, a series of calibration measurements operating at different input powers must be performed and the calibrated results have to be pre-programmed into the measurement system.

A simpler approach also based on the power-switching scheme has been designed and implemented. It measures the variation of the power consumption to the micro-radiator, keeping the photodetector signal constant at all pressures. Equation (6.2.2) can be rewritten as:

$$p = B10^{\frac{I_d - A}{k}} \tag{6.2.3}$$

If we keep the photodetector output constant, the pressure versus power consumption curves can be plotted using equation (6.2.3) along with the curve fitting equations of Figure 6.6 and Figure 6.7. The resulted pressure versus power consumption curves are plotted in Figure 6.8. Experiment data directly taken from Figure 6.4 are also plotted in Figure 6.8. The difference between the experimental data and curves plotted using equation (6.2.3) is caused by the curve fitting in Figure 6.6 and 6.7. The least-squares fitting polynomial equations for the experimental data are shown in the figure, but not the curves, for simplicity.

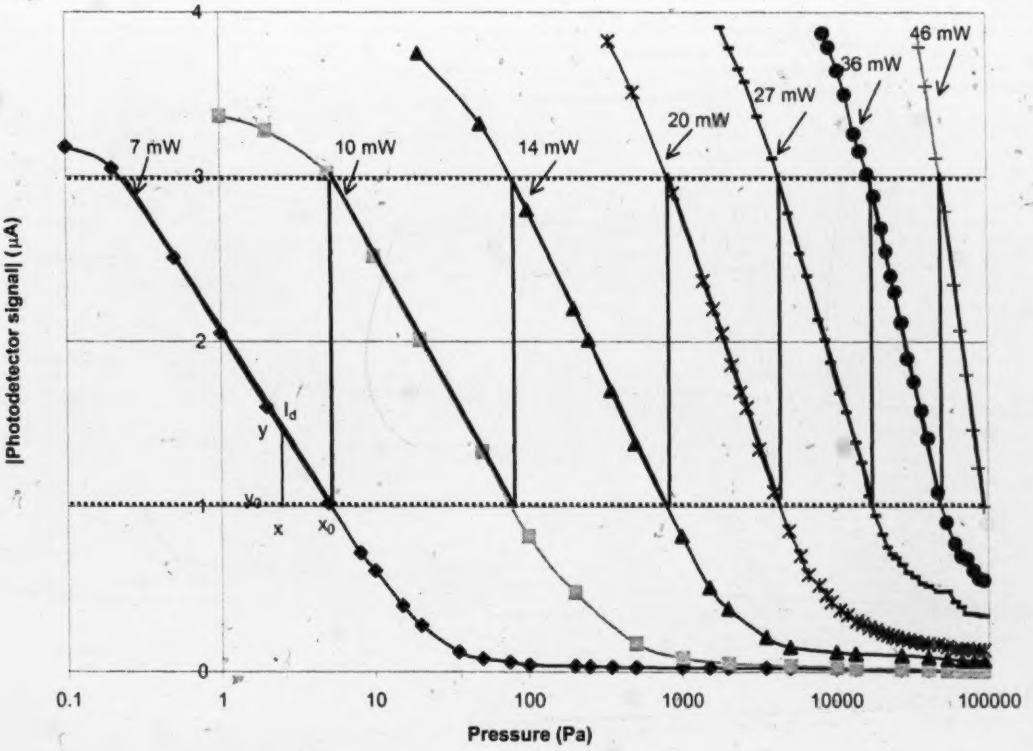

Figure 6.4 Photodetector signal versus pressure operating at different constant powers showing power-switching scheme

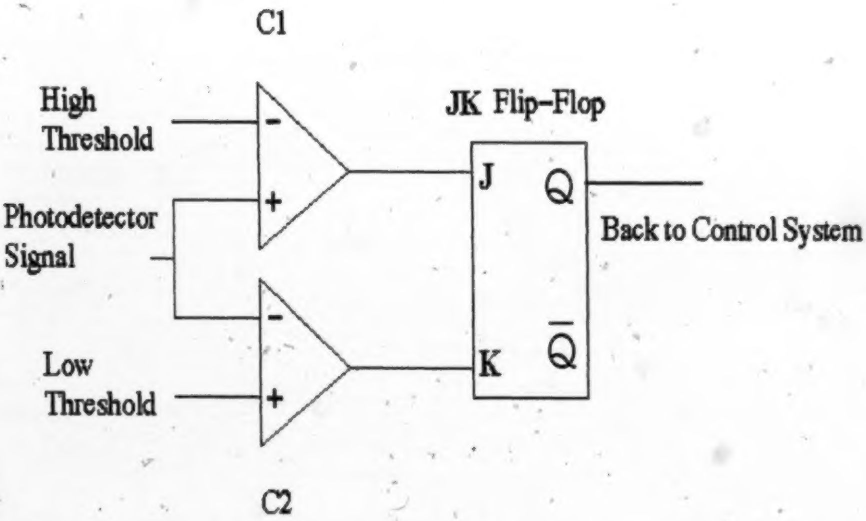

Figure 6.5 Conceptual diagram of power-switching scheme

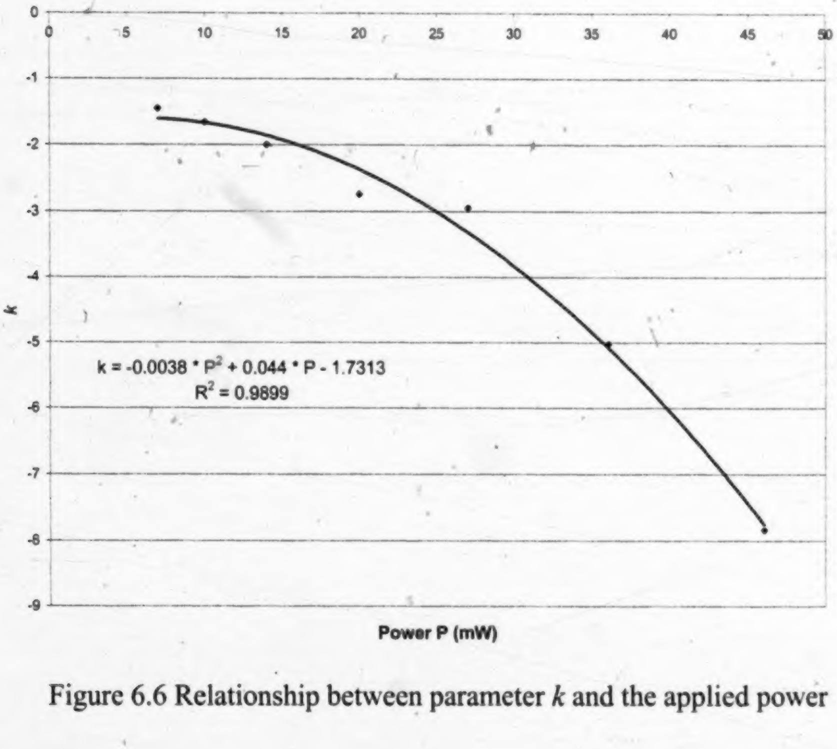

Figure 6.6 Relationship between parameter *k* and the applied power

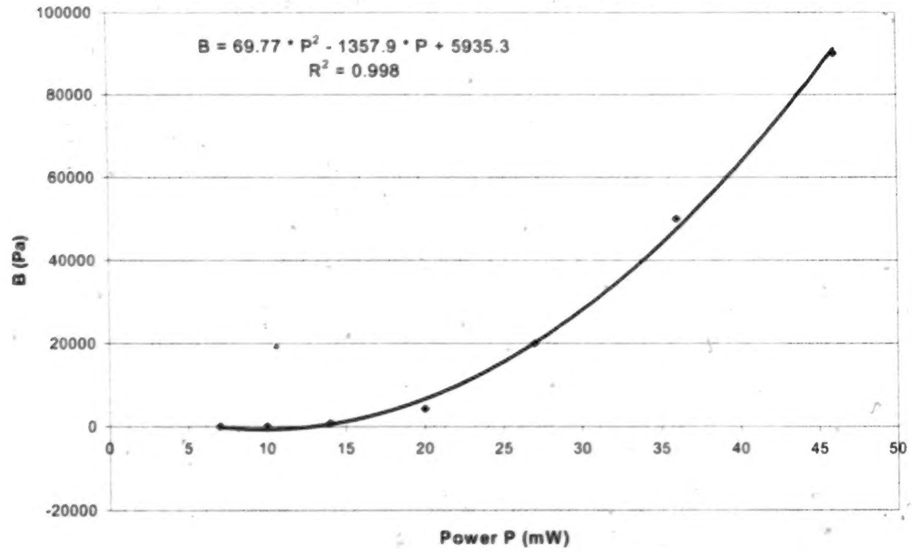

Figure 6.7 Relationship between parameter B and the applied power

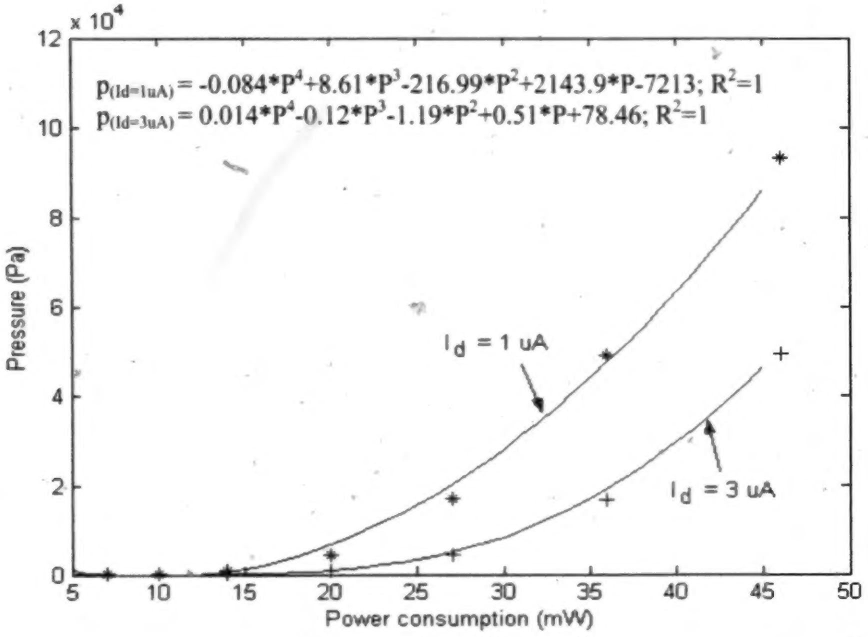

Figure 6.8 Power consumption of the micro-radiator versus the pressure with constant photodetector output of 1 μA or 3 μA. The plotted curves are derived from equation (6.2.3); the least-squares polynomial equations fitted to the experimental data are not plotted.

Compared with the power-switching measurement shown in Figure 6.4, this approach has the advantage of ease of implementation, but the minimum pressure variation it can measure is limited by the output of the constant power supply. Since the minimum output of the constant power supply is about 10^{-3} mW and dp/dP of the curves in Figure 6.8 varies from 10 to 10^5, the minimum pressure variation that can be measured is about 10^{-2} Pa at low pressure and about 10^2 Pa at high pressure. The minimum pressure variation that can be measured in Figure 6.4 is about 10^{-5} Pa at low pressure and 10^{-1} Pa at high pressure due to the high sensitivity of the photodetector.

6.3 Calibration by comparison

If the vacuum gauge is calibrated by copmaring its reading to the pressure indicated by a so-called reference gauge (secondary standard), it is called *calibration by comparison* [3]. In this section, the micro-radiator pressure sensor is calibrated and tested using this method.

6.3.1 Calibration curves

For a micro-radiator fabricated with a different process run, slightly different characteristics have been observed. The calibration curve is shown in Figure 6.9 (a) and (b). A smaller vacuum chamber originally designed for XeF_2 etching is used as the experimental chamber. Details of the etching vacuum system can be found in reference [2].

It is difficult to find a close polynomial to fit all experiment data, so the curve was divided into two parts and separately fitted into polynomial curves as shown in Figure 6.9 (a) and (b).

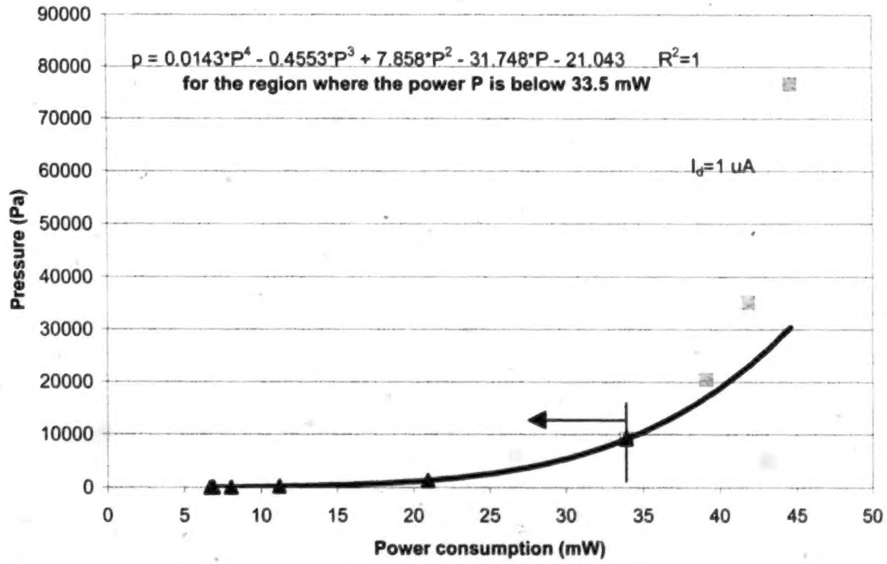

Figure 6.9 (a) A typical calibration curve with data below 33.5 mW being fitted onto a polynomial curve

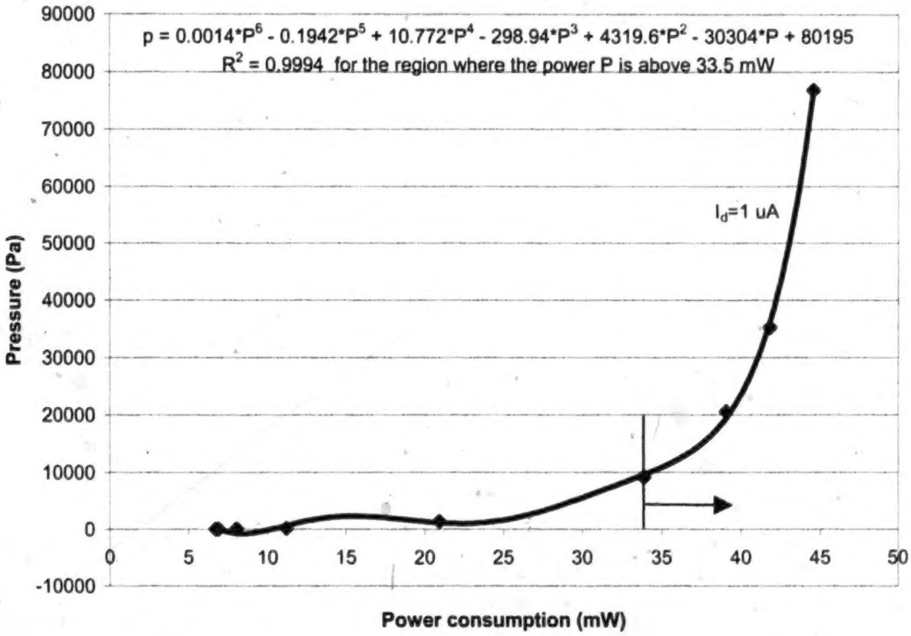

Figure 6.9 (b) A typical calibration curve with data above 33.5 mW being fitted onto a polynomial curve

6.3.2 System automation

The pressure measurement system using the power variation method above is automated using a program written in Instrument Basic. The flow chart of the program is shown in Figure 6.10.

At the beginning of the program, the user can choose a constant photodetector signal to perform the pressure measurement if multiple calibration curves are available. The program first sets up the Source Measure Unit (SMU) and Digital Multi-Meter (DMM) and measures the room temperature resistance of the micro-radiator by outputting a 0.1 mA current into the micro-radiator and measuring the corresponding voltage across it. A small initial input power is then used to determine an initial current to the micro-radiator; the corresponding radiation is measured and compared to the predefined constant value. If the absolute value of the difference between the measured signal and the predefined constant value is larger than ΔI_d, the input current to the micro-radiator is increased or decreased correspondingly by a small step value ΔI and the updated radiation signal is measured again and compared with the predefined constant value again. The loop continues until the difference between the measured photodetector signal and the predefined constant value is smaller than a tolerance value ΔI_d (e.g. 0.05 μA), the power consumed by the micro-radiator is calculated and the corresponding pressure is then calculated by the pressure (p) - power (P) calibration curve.

The time each measurement takes depends on the pressure, predefined initial power and the tolerance value ΔI_d. Optimization has been made in the program to vary the current step value according to the difference between the photodetector signal and predefined value. When the difference is big, a larger step current ΔI is used to increase or decrease the radiation. Otherwise a smaller step current is used.

A sample code can be found in Appendix C.

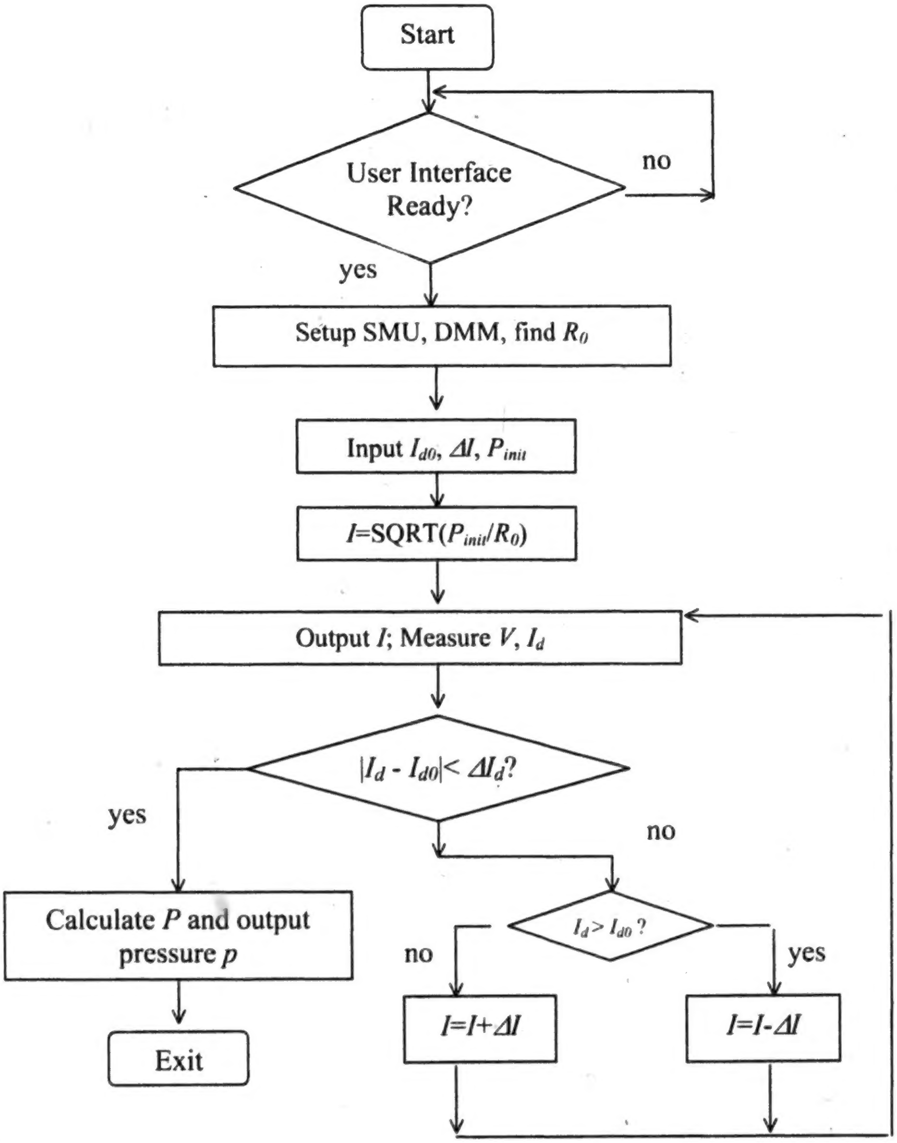
Start
User Interface Ready?
no
yes
Setup SMU, DMM, find R_0
Input I_{d0}, ΔI, P_{init}
I=SQRT(P_{init}/R_0)
Output I; Measure V, I_d
$|I_d - I_{d0}| < \Delta I_d$?
yes
no
Calculate P and output pressure p
Exit
$I_d > I_{d0}$?
no
yes
$I=I+\Delta I$
$I=I-\Delta I$

Figure 6.10 Flow-chart of the pressure measurement system

6.3.3 Test results

The automated measurement system has been tested for a series of devices at a constant photodetector output of 1 μA. Table 6.3 shows the typical results for a pressure measurement using a calibration curve obtained from the same device. The reference gauges are two Wallace & Tiernan diaphragm manometers (2667 - 9333 Pa, 67 - 2667 Pa).

Table 6.3 Typical measurement results using calibration curve obtained from same device

Reference gauge (Pa)	Micro-radiator output (Pa)	Difference (%)
146.65	151.98	3.5
182.65	182.65	0
399.96	414.63	3.5
6532.68	6132.72	6.5
21997.80	23331.00	5.7
49595.04	50261.64	1.3
74125.92	80525.28	7.9
93057.36	85991.40	8.2

From Table 6.3, we can see the difference between the micro-radiator measurement and the reference gauge is 8.2 % or less. Differences are caused by the curve fitting equations, and tolerance value defined in the program. It will be improved if a smaller tolerance value is used, but the computation time will be longer.

If a typical calibration curve is used, test results on different devices generate a difference as high as 35%. Therefore, for each micro-radiator vacuum sensor, a calibration test before using it as pressure sensor is necessary. The calibration curve may change over time; therefore, a calibration test should be done periodically.

6.3.4 Factors that affect the calibration

There are many factors that affect the calibration of the micro-radiator pressure sensor. Here we discuss several important factors that should be taken into account for the device calibration.

1. Distance between micro-radiator and photodetector:

The distance between the micro-radiator and photodetector will affect the magnitude of photodetector output. All of the experimental data in the previous sections were obtained using a default distance of 2.5 cm. Figure 6.11 shows the photodetector output versus pressure for two different distances, 1 cm and 3 cm. Input power to the micro-radiator is 20 mW. From Figure 6.11 we can see the shorter the distance, the stronger the photodetector signal because the proportionality constant *k* in equation (4.4.1) is bigger for a shorter distance. Both the intensity of the radiation from the micro-radiator and the solid angle from the micro-radiator to the photodetector are bigger with a shorter distance.

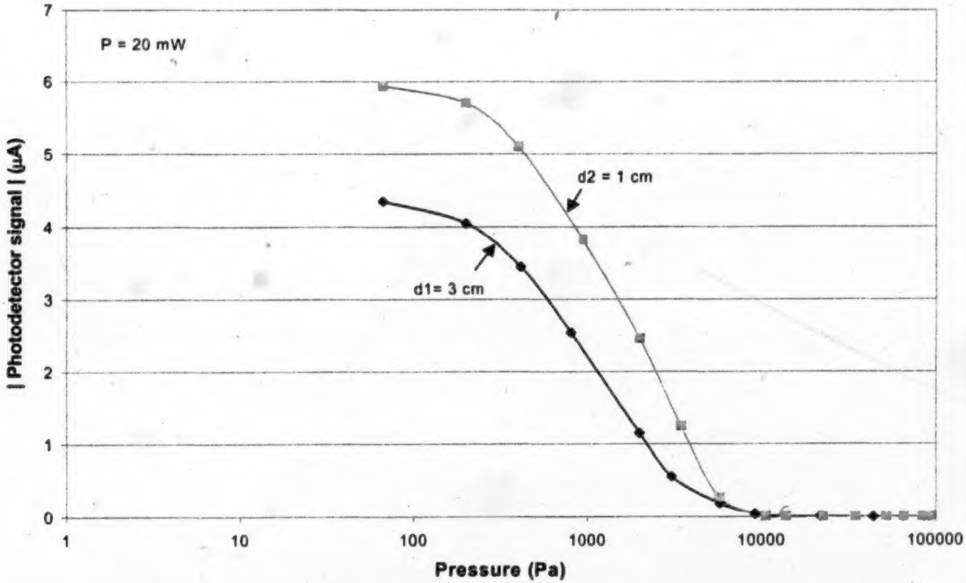

Figure 6.11 Photodetector signal versus pressure with different distance between micro-radiator and photodetector

2. Ambient temperature:

From the theoretical calculation in Chapter 4, we can see the temperature of the ambient gas and substrate is an important factor in calculating the micro-radiator equilibrium temperature. The conventional Pirani gauge shows a degree change in gauge-wall temperature can cause up to 20% change in gauge readings [3]. The effect of the ambient temperature on the micro-radiator sensing results was not investigated in this project. Due to the high operating temperature of the micro-radiator, the effect of the ambient temperature is minimized.

3. Accommodation coefficient α

The accommodation coefficient introduced in Chapter 3 depends on the surface condition of the micro-radiator. There may be an increase of α by as much as a factor of 10 when a 'clean' surface becomes contaminated with an adsorbed layer of gas molecules [4]. Therefore, the micro-radiator should be recalibrated periodically to increase the accuracy of measurement. The recalibration can be done easily with a reference gauge and the automated pressure measurement system program listed in Appendix C.

4. Ambient gas

Different gases have different thermal conductivities at different pressures. Thus the calibration of the micro-radiator is gas dependent. The micro-radiator needs recalibration if a gas other than air is measured. An example of the radiation signal from the incandescent micro-resistor is shown in Fig. 6.12, for two different gases, He and air. The photodetector output versus the pressure curve shifts to the left when the ambient gas is changed from air to He. This feature may be used to analyze the ambient gas change. It should be noted that the reference gauge is also gas dependent. Thus the pressure indicated in Figure 6.12 is not accurate for He.

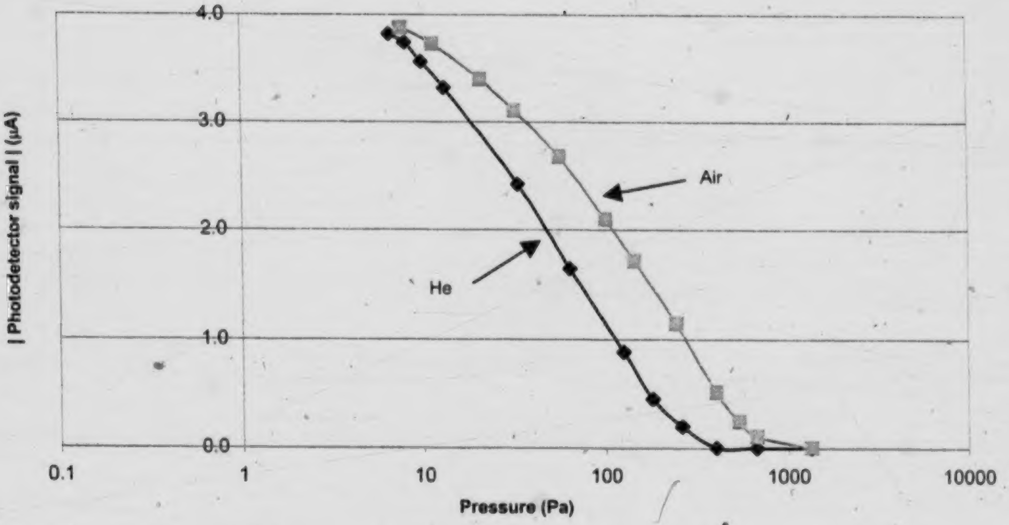

Figure 6.12. Photodetector outputs for air and He

References:

[1] W. Allegretto, B. Shen, P. Haswell, Z. Lai, and A. M. Robinson, "Numerical Modeling of a Micromachined Thermal Conductivity Gas Pressure Sensor", IEEE Transactions on Computer-aided Design of Integrated Circuits and Systems, Vol. 13, No. 10, October, 1994, pp. 1247-1256.

[2] K. Brown, EE 641 Project report, Department of Electrical and Computer Engineering, University of Alberta, 1999.

[3] J. M. Lafferty, Foundations of Vacuum Science and Technology, John Wiley & Sons, Inc., New York, 1998, p. 673.

[4] J. H. Leck, Pressure Measurement in Vacuum Systems, Chapman and Hall Ltd., London, 1957, p. 76.

Chapter 7

CMOS Photodetector Design

We have demonstrated in the previous chapters that measuring the radiation from a micro-radiator is an effective way of measuring gas pressure. In terms of packaging such a device, integrating the photodiode with the emitter chip would be an advantage. First, it integrates the emitter and the detector into a single unit. Second, the distance between the emitter and the photodetector can be reduced to about 100 micron or less. Therefore, the photodetector output signal will increase. In addition, the decreased distance between the emitter and the photodetector will shift the sensitive range to a higher pressure.

A P-N junction diode and a bipolar transistor are two of the most commonly used photodetector configurations and they are natural elements in a standard CMOS process. We have designed and tested a three-mode CMOS photodetector for this purpose. Integration of the photodetector with the micro-radiator is achieved using an assembly approach and a flip-chip integration approach is discussed as future work of the project.

7.1 P-N junction and photodiode

The P-N junction is one of the most important junctions in solid-state electronics. It refers to the change from N-type material, which means the majority charge carriers are electrons, to P-type material, which has holes as the majority charge carriers, within a single crystal.

Adding impurities can change the majority charge carries of the material. The added impurity is called dopant. For example, when an atom containing five outer-shell electrons, such as arsenic, is added to a semiconductor, four of them participate in the covalent bonds and one electron is left over. This extra electron is nearly free and has an energy level that lies within the energy gap, just below the conduction band. Such a pentavalent atom in effect donates an electron to the structure and, hence, is referred as donor. If the semiconductor is doped with atoms containing three outer-shell electrons, such as indium and aluminum, the three form covalent bonds with neighboring atoms, leaving an electron deficiency, or hole, in the fourth bond. The energy levels of such impurities also lie within the energy gap, this time just above the valence band. Electrons from the valence band have enough thermal energy at room temperature to fill these impurity levels, leaving behind a hole in valence band. Because a trivalent atom in effect accepts an electron from the valence band, such impurities are referred to as acceptors.

The P-N junction can be realized by either changing the dopant from donors to acceptors during the growth of the crystal or by introducing impurities of one type into regions of a crystal that was grown with lighter doping of the opposite type [1]. The fabrication techniques used to form P- and N-type regions involve i) epitaxial procedures where the dopant species are simply switched at a particular instant in time; ii) ion-implantation in which the dopant ions are implanted at high energies into semiconductor; iii) diffusion of dopants into an oppositely doped semiconductor.

Figure 7.1 gives the schematic view of a P-N junction and various current and particle flow components in the P-N diode at equilibrium. The P-type region at the far left and the N-type region at the far right in Figure 7.1 (a) are neutral. The density of the acceptors at the P-type region and the density of the donors at the n-type region exactly balance the densities of holes and electrons correspondingly. In the middle region, where P-type and N-type materials meet, an electric field exists. This region is called the depletion region and extends a distance X_p in the p-region and a distance X_n in the N-region. Any electrons or holes in the depletion region are swept away by the electric field present. Thus a drift current exists which counterbalances the diffusion current that arises because of the difference in electron and hole densities across the junction. The directions of the four components of particle flow within the transition region and the resulting current directions are shown in Figure 7.1 (b).

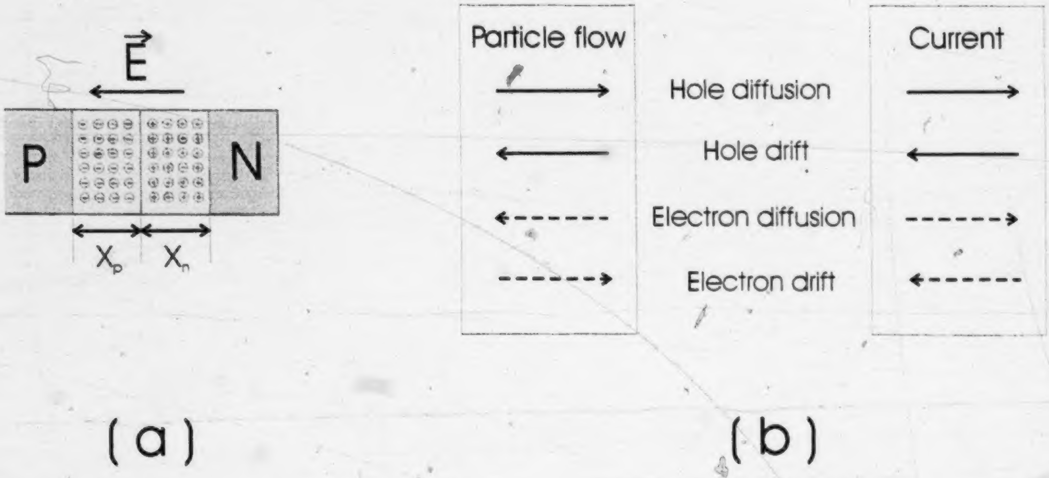

Figure 7.1 (a) An idealized model of the P-N junction without bias showing the neutral and the depletion areas. (b) A schematic showing various current and particle flow components in the P-N diode at equilibrium

A P-N junction is also called a diode and the junction device designed to respond to photon absorption is called a photodiode. When a voltage is applied to the P-N junction as shown in Figure 7.2 (a), the excess carriers generated by the incident photons are collected to form a photocurrent I_{op}. If the junction is uniformly illuminated by photons with energy $h\nu$ larger than the energy band gap of the material E_g and assuming the excess carriers are generated at a rate g_{op} (electron-hole pair/cm^3-s), the resulting current due to collection of the optically generated carriers by the junction can be calculated by

$$I_{op} = qAg_{op}(L_p + L_n + W) \tag{7.1}$$

in which q is the electrical charge; A is the diode cross-sectional area and we assume a uniform generation rate in the diode; L_p and L_n are the diffusion length of hole and electron respectively; and W is the width of the depletion region. Diffusion length is the average distance where the hole or electron can be found from the point where they were generated.

Figure 7.2 (b) shows the symbol of a diode and Figure 7.2 (c) the I-V characteristics of an illuminated junction. The current due to optical generation is negative and proportional to g_{op} when the junction is reverse biased. Since g_{op} is linearly proportional to the intensity of incident light at a given wavelength in the low intensity regime, the optically generated current is linearly proportional to the intensity of incident light. When the intensity of incident light is extremely high, the optically generated current becomes saturated. The saturation point of the linear response depends on the reverse voltage applied to the P-N junction. The saturation points are not indicated in Figure 7.2 (c).

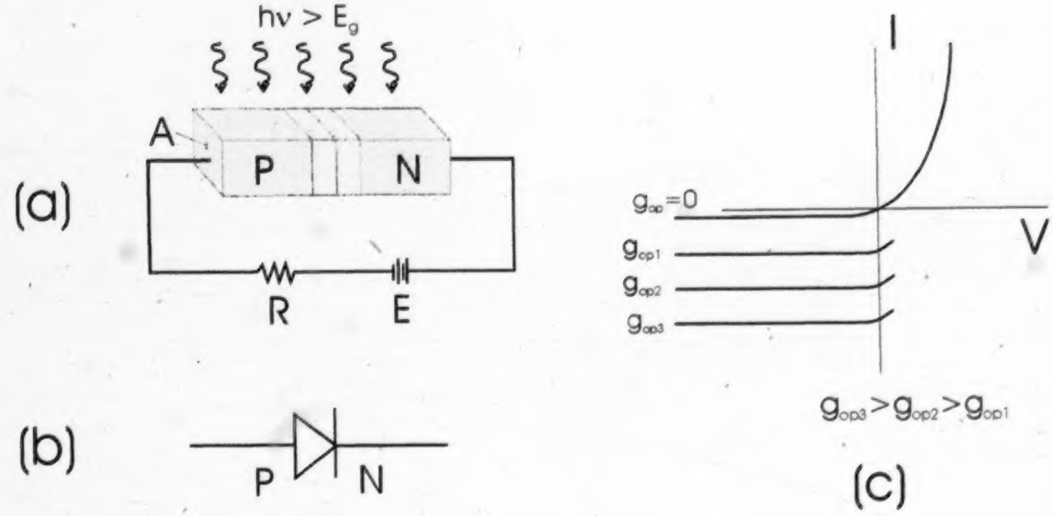

Figure 7.2 (a) Optical generation of carriers in a P-N junction; (b) P-N junction symbol; (c) I-V characteristics of an illuminated junction

7.2 Phototransistor

A bipolar device refers to a device where the action of both electrons and holes is important. When two back-to-back P-N diodes are connected together, a bipolar junction transistor (BJT, either N-P-N or P-N-P) is formed. Figure 7.3 shows an N-P-N transistor, which has an emitter, a base and a collector. The n^+ region, which serves as the source of injected electrons, is called the emitter, and the N region into which the electrons are swept by the reverse-biased junction is called the collector. The center P region is called the base. When the emitter base junction (EBJ) is forward biased and the base-collector junction (BCJ) is reversed biased, the BJT produces a high current gain.

A number of currents can be identified in the BJT, as shown in Figure 7.3. The first one is from the injected electrons lost to recombination in the base, and the second one is due to the electrons reaching the reverse-biased collector junction. The third one is produced by the thermally generated electrons and holes making up the reverse saturation current of the collector junction and the fourth one is from the holes supplied by the base contact for recombination with electrons. The last one is due to holes injected across the forward biased emitter junction.

The phototransistor is a bipolar transistor used for optical detection. The base current of a phototransistor is not provided by an external supply (often there is no base contact on the phototransistor), but through optical generation. Light shining on the device creates electron-hole pairs. These pairs are generated throughout the device. The phototransistor provides higher gain than the photodiode due to the transistor action.

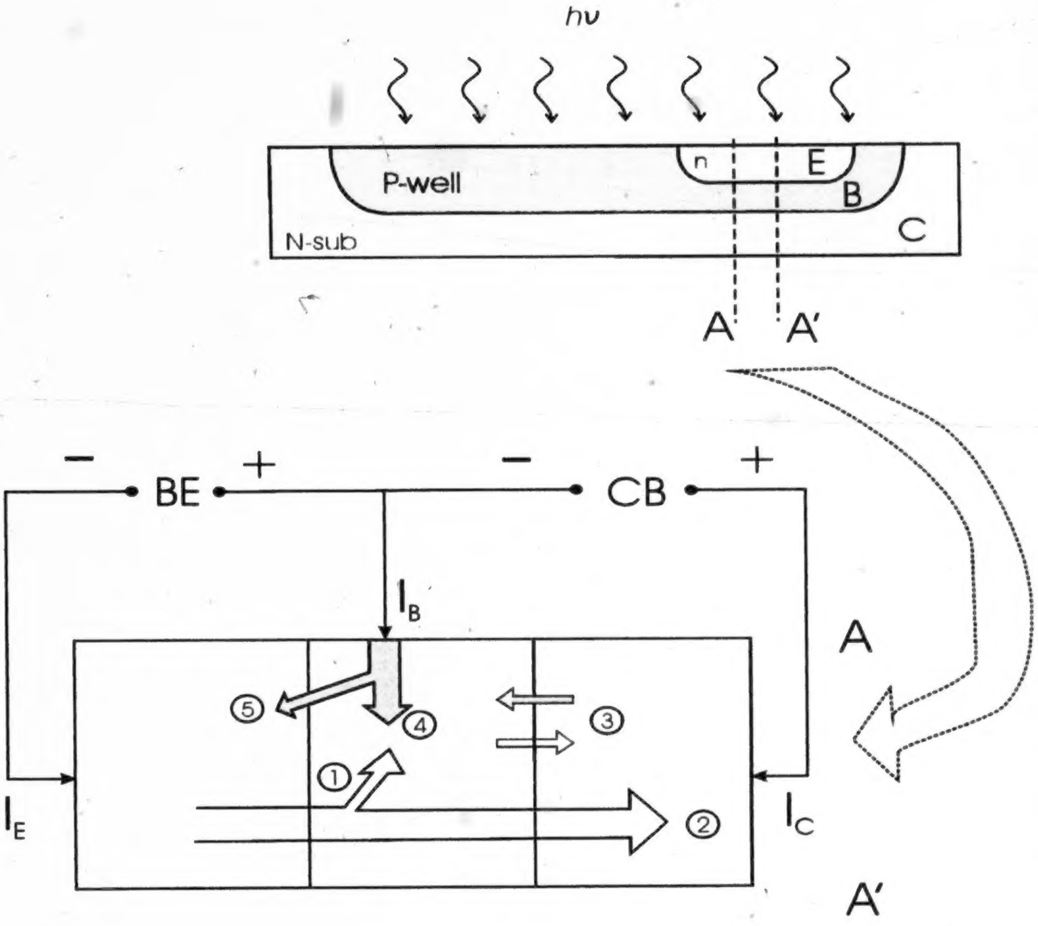

Figure 7.3 Schematic of an N-P-N transistor showing hole and electron flow: (1) injected electrons lost to recombination in the base; (2) electrons reaching the reverse biased collector junction; (3) thermally generated electron-hole pairs making up the reverse saturation current of the collector junction; (4) holes supplied by the base contact for recombination with electrons; (5) holes injected across the forward biased emitter junction.

7.3 Three-mode CMOS photodetector design

The sensitivity of a photodiode as introduced in section 7.1 can only be changed by the applied voltage across the diode and the photodiode output can be saturated when the intensity of incident light is high enough [2]. Therefore, this amount of controllability is not enough for practical applications. Ward-Syrzycki's multi-sensitivity photodetector [3] is designed here and fabricated with the CMOS IC process for integration of the micro-radiator pressure sensing system.

The detector features three modes of operation corresponding to different light intensities. Figure 7.4 (a) shows the design of a vertical N-P-N transistor that can be used in two different operating modes with a Metal Oxide Semiconductor Field Effect Transistor (MOSFET) attached.

The MOSFET is placed across the base-emitter junction of the vertical n-p-n phototransistor; it is used to force the device into one of two modes. The equivalent circuits of two operating modes are shown in Figure 7.4 (b). In the diode mode, the MOSFET is turned on and permits the substrate-to-p-well photocurrent to flow directly to the n^+ emitter, and no transistor action occurs. The resulting structure is like a reverse biased substrate-to-p-well junction as introduced in Section 7.1. When the MOSFET is turned off, electrons generated by photons in the p-well add to the base current of the vertical transistor and is then amplified by the forward current gain of the device. The resulting structure is like the one shown in Figure 7.3.

The third mode of the photodetector can be obtained by connecting two vertical transistors in a Darlington connection. A second transistor then amplifies the output current from the first phototransistor.

A photodetector with all of three operational modes can be implemented using two MOSFETs as shown in Figure 7.5. Figure 7.5 (a) shows the structure and Figure 7.5 (b) shows the equivalent circuit of the three-mode photodetector design. The two gate inputs *Sel 1* and *Sel 2* can be set in any of four combinations, each resulting in a different mode of operation. Table 7.1 shows the function table of the designed photodetector. When *Sel 1* is high and *Sel 2* is low, the circuit is equivalent to a reverse-biased photodiode with the output signal amplified by a transistor, and it is not defined as a separate operating mode here.

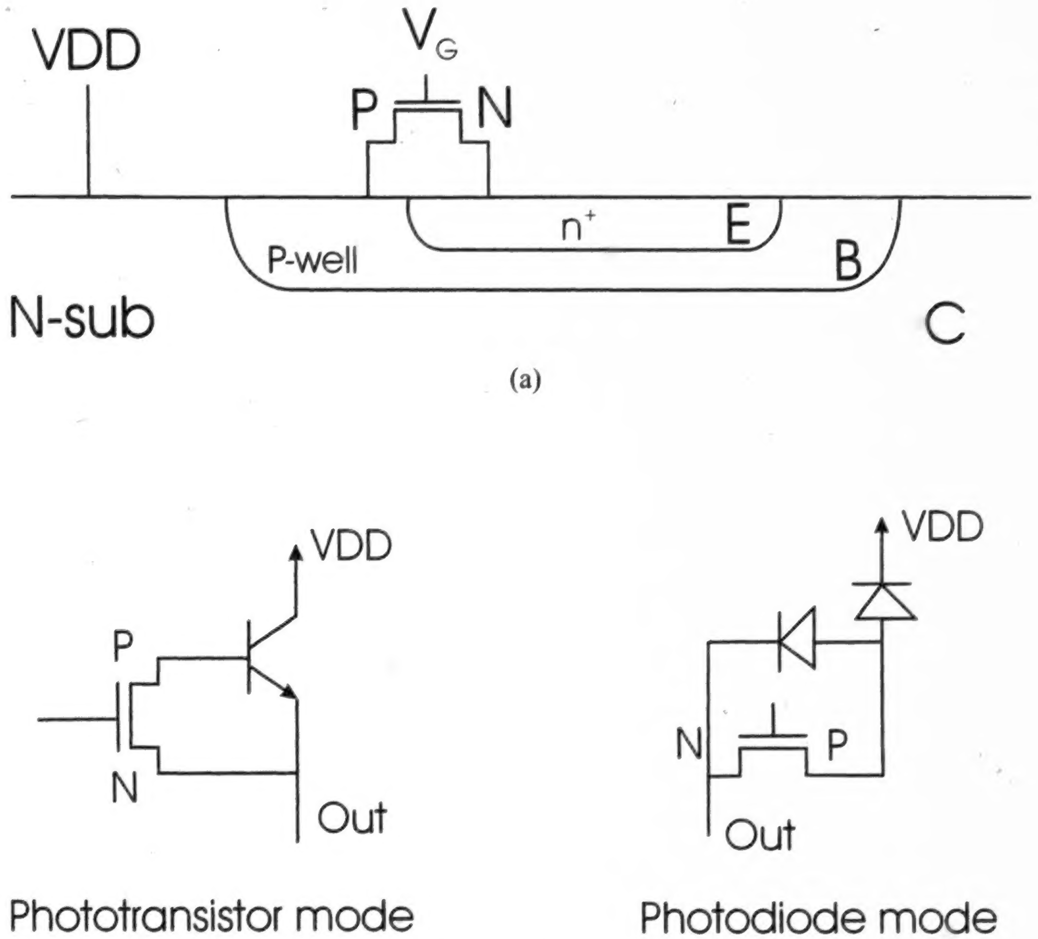

(a)

(b)

Figure 7.4 Structure and equivalent circuits of the CMOS multi-mode photodetector

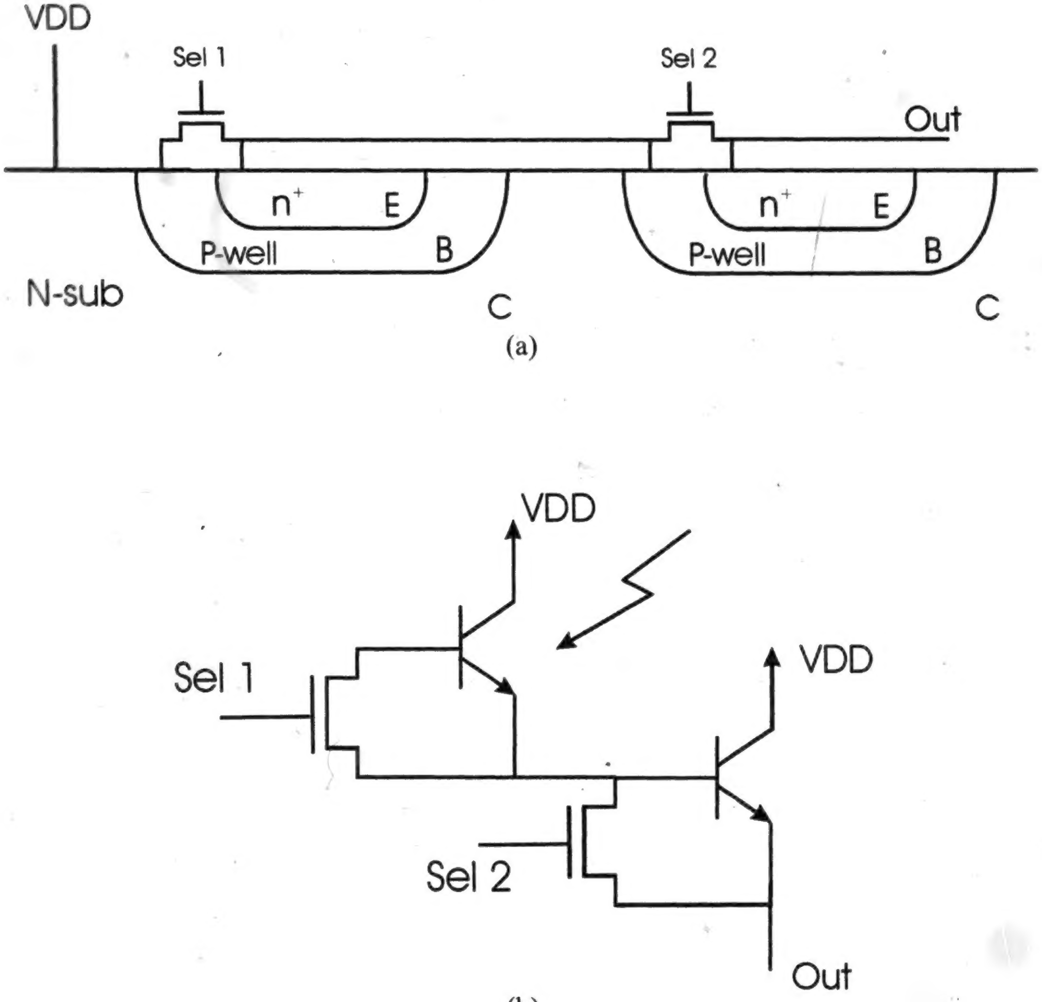

(a)

(b)

Figure 7.5 Structure and equivalent circuit of the three-mode photodetector

Table 7.1 Function table of three-mode photodetector

Sel 1	Sel 2	Equivalent Circuit	Working Mode
1	1	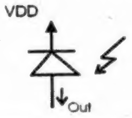	Photodiode
0	1	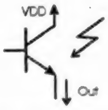	Phototransistor
0	0	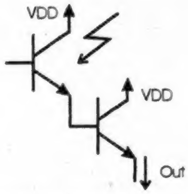	Darlington connection
1	0	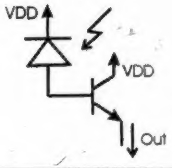	Photodiode with transistor amplifier

7.4 Test of three-mode CMOS photodetector

The three-mode CMOS photodetector was tested using a point source, a 4.2 mW adjustable focus laser diode (Thorlabs Model S1021), and a micro-radiator. The results of the tests are described in this section.

7.4.1 Test with a point light source

The light source introduced in Chapter 4 has been shown to behave as a point source of light. It is now used to test the photodetector working in the photodiode mode and phototransistor mode. Figure 7.6 (a) and (b) show the output of the photodetector versus the inverse distance squared between the photodetector and light point source. Experiment data were least-squares fitted into straight lines, which means the photodetector output is linear to the intensity of incidence light and is a reliable detector to measure the radiation from the micro-radiator in the signal range covered by this test. The output of the photodetector working in the phototransistor mode is about two orders of magnitude higher than the one working at photodiode mode. This is due to the light falling on the photodiode changing the base current of the transistor, causing the collector current to be amplified.

7.4.2 Test with a laser diode

The wavelength of the laser diode is 670 nm. A series of plastic films with identical thickness were used as the intensity attenuator. Different attenuation was achieved by using a different number of films between the laser diode and the photodetector. A Newport 840 optical power meter was used to measure the light intensity. Output signal from the photodetector was amplified by a large dynamic range current amplifier fabricated by Melles Griot (model 13 AMP 003) and the amplified signal was measured with a digital multi-meter.

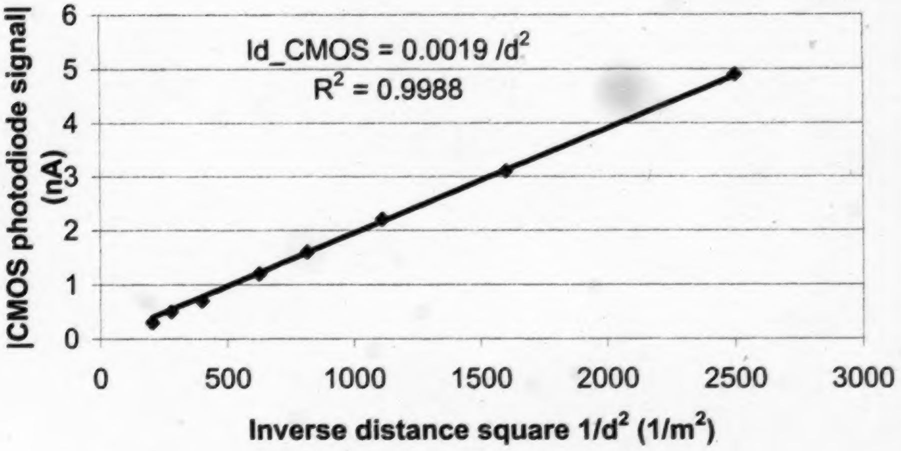

Figure 7.6 (a) Output of photodetector working in photodiode mode versus inverse distance squared of the light source

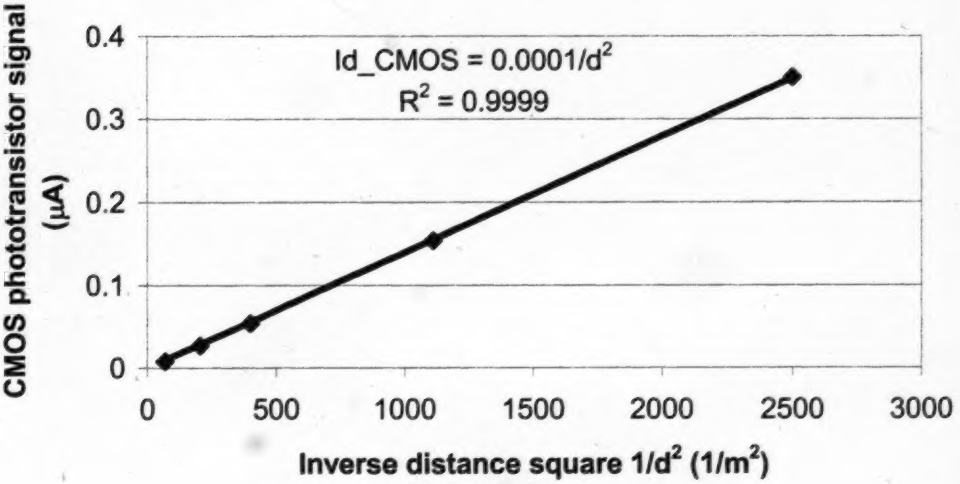

Figure 7.6 (b) Output of photodetector working in phototransistor mode versus inverse distance squared of the light source

Figure 7.7 shows the measured response of the three-mode photodetector operating in different modes. The photodetector signal is linear to the power of incident light in the range from 0.01 mW to 10 mW when it is operated in the photodiode mode and phototransistor mode. The output of the photodetector operating in phototransistor mode yields a current approximately two decades greater than that resulting from the photodiode operation mode as expected from the linearity results. The output of the photodetector operating in the Darlington connection mode is not linearly proportional to the intensity of incident light. The amplitude of the output signal increases more than two decades when the incident power is around 1 mW. This non-linearity is because the second transistor is not covered from the incident light. The output signal is a combination of the amplified signal from the first phototransistor and the photocurrent generated in the second phototransistor. In order to get the linear response from the third mode, the second phototransistor should be covered with a metal layer in the fabrication process to prevent the photocurrent from being generated. This has been improved in our next design, but no chip has been tested by the time of writing this thesis. A linear response is expected and the second transistor will amplify the magnitude of the signal by about two decades.

The output of CMOS photodetector was also tested as a function of sensitive area of the design. Figure 7.8 shows the result from two designs with two different sensitive areas working in the phototransistor mode. The ratio of the sensitive areas (the P-well region in Figure 7.4 (a)) is 8.7:1, which is the same as the average ratio of the corresponding outputs. This indicates that the output of CMOS photodetector is proportional to the area of sensitive surface.

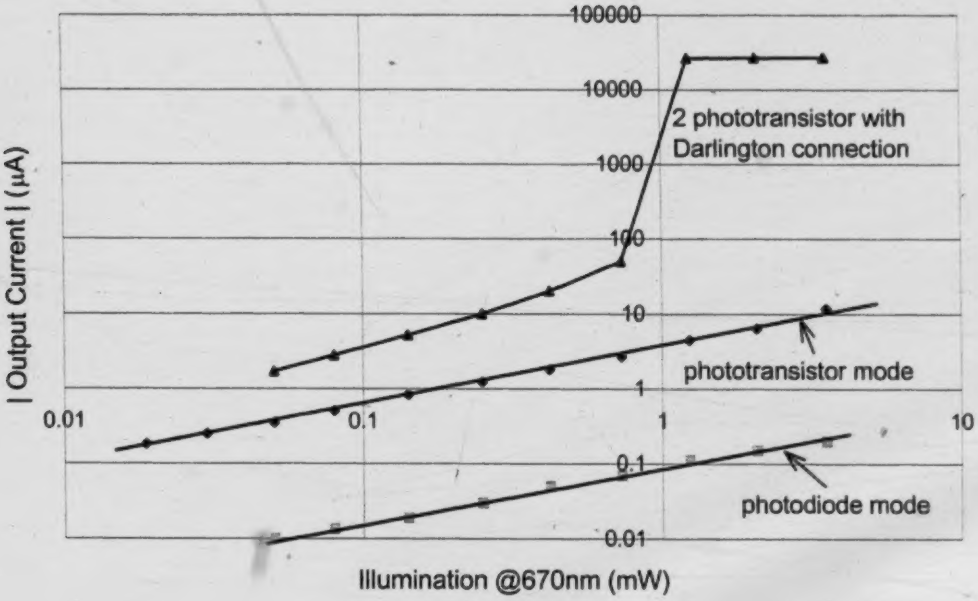

Figure 7.7 Measured response of the CMOS photodetector operating in different modes

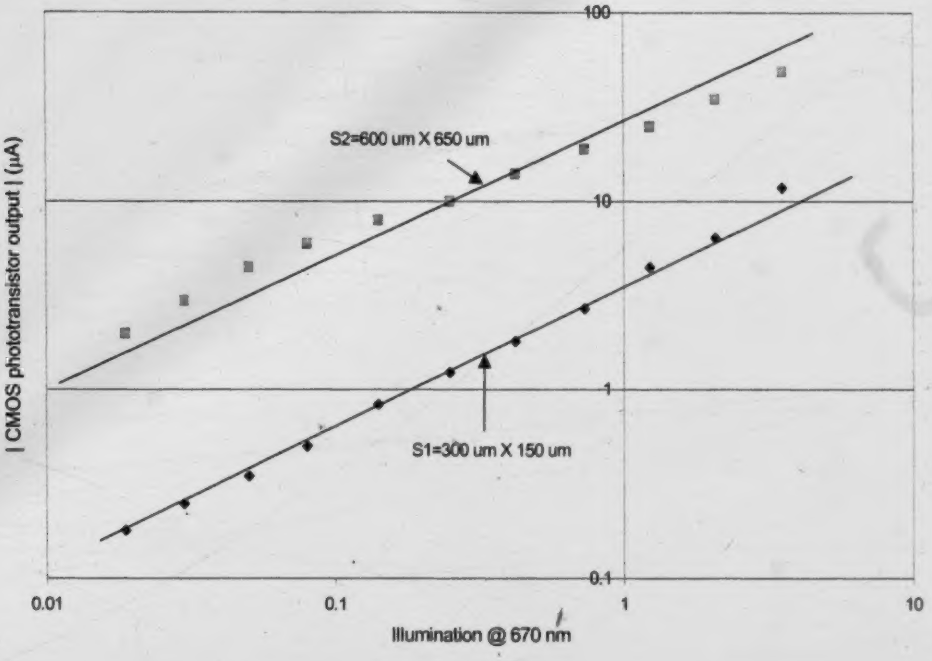

Figure 7.8 Comparison of CMOS photodetector output with two different sensitive areas in the ratio of 8.7:1

7.4.3 Test with a micro-radiator

The CMOS photodetector working in the phototransistor mode was used to measure the radiation from a micro-radiator. Both micro-radiator and photodetector were mounted on 40-pin DIPs and the two chips were put face-to-face with each other at a separation of 1 mm. Alignment was optimized by manually moving one device to approximately achieve maximum output signal.

Figure 7.9 shows the photodetector output versus the input power of the micro-radiator. From 7.9 we can see the output of photodetector starts to increase rapidly from about 20 mW at one atmosphere. Comparing Figure 7.9 and Figure 5.2, we can see the magnitude of the CMOS phototransistor output is much smaller than the output from the commercial photodiode. The output of the commercial photodiode is about three times bigger than the output of the CMOS phototransistor when the micro-radiator is heated with 30 mW power. The output of the CMOS photodetector operating in the photodiode mode is about 50 times even smaller than the output operating in the phototransistor mode as shown in Figure 7.7. This is due to the sensitive area of the CMOS phototransistor is about four orders of magnitude smaller than that of the commercial photodiode although the distance between the micro-radiator and the photodetector is about 25 times shorter.

The micro-radiator input power only went up to 35 mW in Figure 7.9, while the commercial photodiode was tested with a micro-radiator input power up to 60 mW. In the common range of the two figures, the photodetector response curves demonstrated a similar shape.

Figure 7.10 shows a typical response from the CMOS phototransistor used to detect the radiation from a micro-radiator with a 15 mW input in a pressure range from 100 Pa to one atmosphere. Compared with the experimental results obtained using the commercial photodiode and a power input of 14 mW in Figure 6.4, the shape of the curves is similar, but the pressure sensitive ranges are not exactly same. This may be due to the difference of the micro-radiators fabricated with two different process batches, the change of micro-radiator to photodetector distance and the different spectral response of two photodetectors.

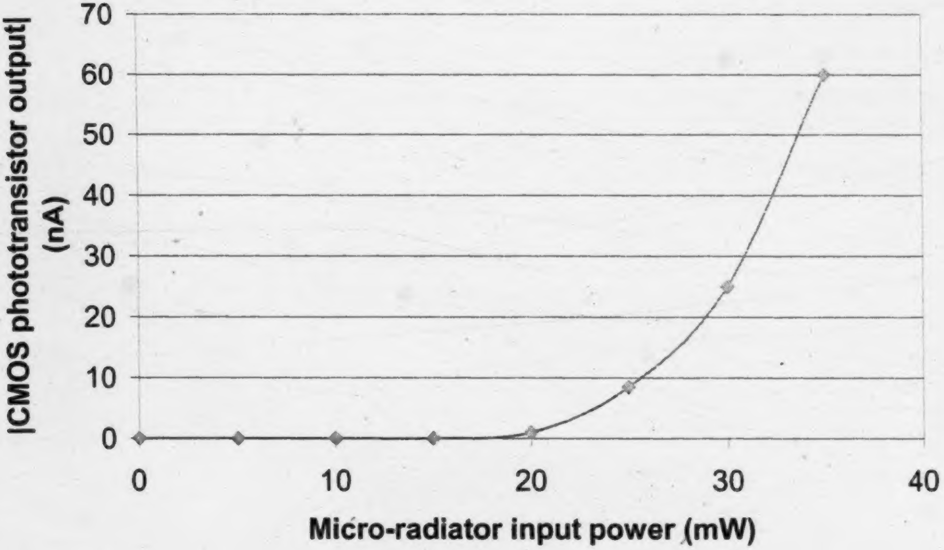

Figure 7.9 Output of CMOS photodetector working in the phototransistor mode versus power input of micro-radiator

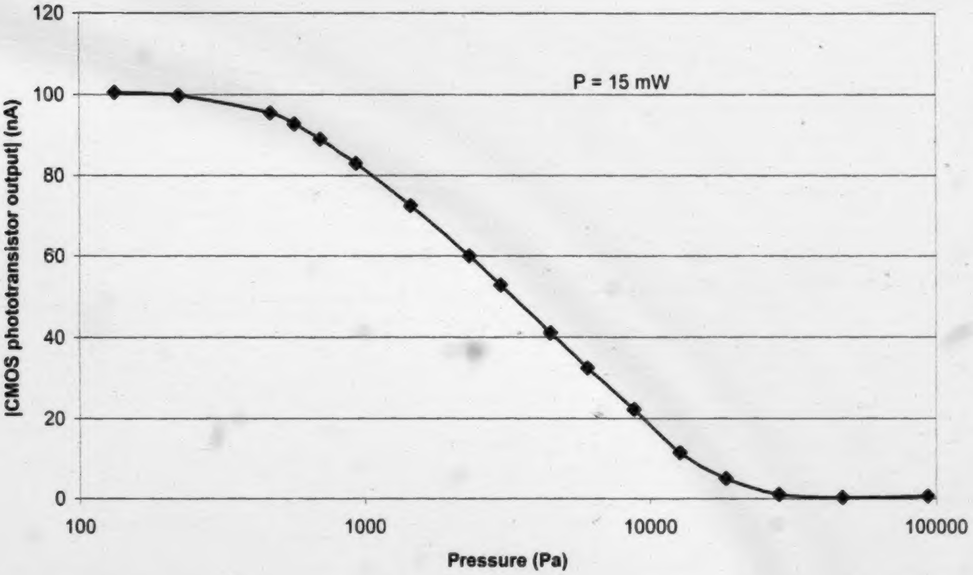

Figure 7.10 Output of CMOS photodetector working in phototransistor mode versus pressure

7.5 Noise in CMOS photodetector

Noise is a rather profound subject. A complete list of all types of noise is beyond the scope of this thesis. The following types of noise are those most likely to be found in the CMOS photodetector [4]:

1. Johnson Noise: Johnson noise is sometimes call thermal noise. It occurs in all conducting materials. It is a consequence of the random motion of electrons through a conductor.
2. Shot Noise: Shot noise is often called "photon noise". It occurs in all photon detectors due to the random arrival rate of photons from the source of radiant energy under measurement and background radiation. In semiconductor diodes, the shot noise associated with the random generation of carriers is the major noise source.
3. Excess Noise: At low frequencies, there are many types of noise for which the noise power varies inversely with frequency. A common term for this type of noise is 1/f noise. It is called excess noise since it exceeds shot noise at low frequencies.

Major noise in the CMOS photodetector can be any one or a combination of the above types of noise. The amplifier used with the photodetector is also made of semiconductor devices; there is also noise in the amplifier. However, all the measurement done in this project are not very sensitive to the noise. Noises were minimized in the experiment by making a number of measurements at each pressure and averaging all the experimental data and pre-offsetting the current amplifier.

7.6 Integration of the micro-radiator and photodetector

We have demonstrated in this chapter that the CMOS photodetector can be used to measure the radiation from the micro-radiator. The integration of the micro-radiator and the CMOS photodetector into a whole system will provide advantages such as better performance and controllability.

Several different approaches can be used in the integration of the CMOS photodetector with the micro-radiator. A monolithic approach, in which the photodetector is fabricated on the same substrate side by side with the micro-radiator, is the simplest approach. However, because the photodetector can only collect a small portion of the radiation from the micro-radiator, a more sensitive photodetector or a micro-radiator that emits more power is necessary. The second approach is an assembly approach such as the one we used for the testing of the CMOS photodetector. Both the micro-radiator and the photodetector are individually packaged and then two chips are aligned and assembled face-to-face with each other. This allows the performance optimization of each device, but requires accurate alignment and the distance between the micro-radiator and the photodetector is limited by the package.

Flip chip MEMS has emerged as an excellent alternative to the above methods. This method involves fabricating the photodetector and the micro-radiator as separate parts and then attaching them, face-to-face, with solder bumps [5]. Figure 7.11 shows an example of the process.

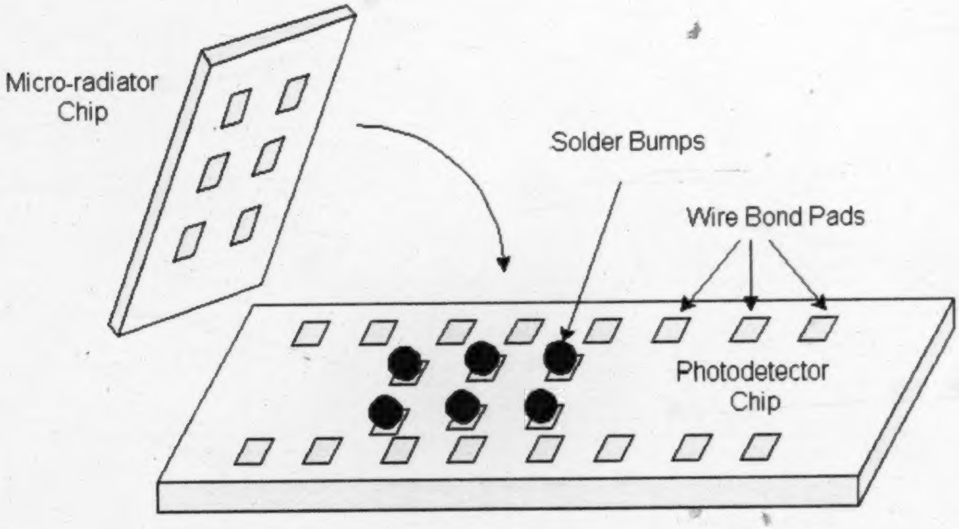

Figure 7. 11 Integration of the photodetector and micro-radiator with flip-chip technique

After the fabrication of both the micro-radiator and photodetector chips, electroplated solder bumps are created for attachment. One chip (e.g. micro-radiator chip in Figure 7.11) is then placed face down (flip chipped) on to the other chip (i.e. photodetector chip in Figure 7.11) and chips are aligned, contacted and heated to reflow the solder bumps. After solder reflow, the joined pair can be placed in a traditional package (e.g. DIP) and wire bonded as shown in Figure 7.12. The solder bumps provide both mechanical and electrical connection for two chips. The height of the solder bumps provides a distance of about 100 μm between the micro-radiator and the photodetector, which will greatly increase the magnitude of the photodetector signal.

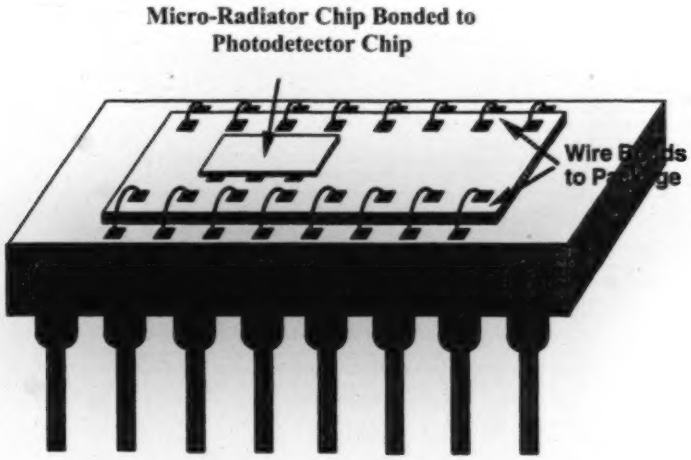

Figure 7.12 The joined micro-radiator / photodetector pair is die-attached and wire-bonded to a DIP

However, to develop a flip-chip process that is compatible with the CMOS process is time consuming and the process can be very expensive. The integration of the micro-radiator pressure sensing system is achieved using the assembling approach as shown in Figure 7.13 in this project and the flip-chip integration is included as future work.

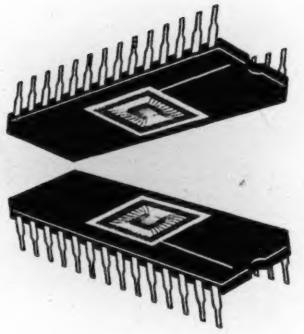

Figure 7.13 Assembling of the photodetector and micro-radiator with two DIPs

References:

[1] B. G. Streetman, Solid State Electronic Devices (fourth Edition), Prentice Hall Inc., London, 1995, p. 140.

[2] R. G. Hunsperger (Ed.), Photonic devices and systems, Marcel Dekker, Inc., New York, 1994, p. 183.

[3] V. Ward, M. Syrzycki and G. Chapman, "CMOS photodetector with built-in light adaptation mechanism", Microelectronics Journal, vol. 24, 1993, pp. 547-553.

[4] W. Budde, Optical Radiation Measurements, Vol.4, "Physical Detectors of Optical Radiation", Academic Press, New York, 1983.

[5] "SmartMUMPs Design Handbook - Draft 7/15/96", JDS Uniphase Inc.- MEMS Business Unit, Research Triangle Park, NC, USA, p. 37 (available through CMC and JDSU WebPages)

Chapter 8

Numerical Modeling

The finite element method is a powerful approach for analyzing physical problems for which no closed-form analytical solutions exist. In the finite element method, a structure is broken down into many small simple blocks or elements. The behavior of an individual element can be described with a relatively simple set of equations. Just as the set of elements would be joined together to build the whole structure, the equations describing the behaviors of the individual elements are joined into an extremely large set of equations that describe the behavior of the whole structure. The computer can solve this large set of simultaneous equations. From the solution, the computer extracts the behavior of the individual elements.

Dr. Allegretto in the Department of Mathematics of the University of Alberta developed a software package that numerically models the operation of the micro-radiator pressure sensor based on a thermal-electrical model similar to the one introduced in Chapter 3 [1]. This package is referred to as Allegretto's Package in the following text. ANSYS, a commercial finite element software available from Swanson Software, also allows us to simulate the operation of the micro-radiator under given operating conditions. Both packages are used to simulate the operation of the micro-radiator and there is no significant difference observed between the results from each package. Although results from both packages are presented in this chapter, only the procedure used to simulate the micro-radiator in ANSYS is introduced in the following section. Please refer to reference [1] for the details of the Allegretto's Package. It should be noted that the Allegretto's Package used in this project is an updated version from what is presented in reference [1], with a radiation term included.

8.1 Model building

The first part of any numerical simulation is building the model. This includes defining the geometry of the device, choosing a suitable element, and defining the material properties. The ANSYS element library has more than 100 different element formulations or types. Different elements have a different number of nodes, degrees of freedom. A suitable element needs to be chosen based on the analysis type and the structure of the device.

Data from the L-Edit layout are extracted for building the geometry of the device [2]. Figure 8.1 shows the 3-D model built with ANSYS 5.6. The input file for the simulation is listed in Appendix D. Two-dimensional data extracted from L-Edit is used as the base to build the 3-D model in ANSYS.

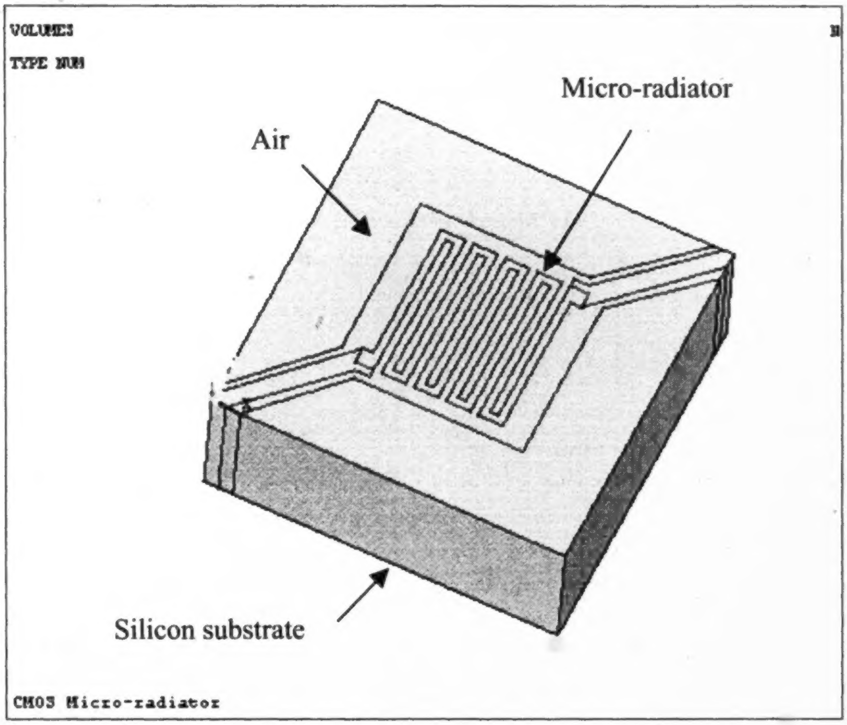

Figure 8.1 Micro-radiator model built in ANSYS

The micro-radiator is built with the air surrounding it and beneath it. The isotropic etching pit is approximated by a rectangular cavity for the simulation. The four sides and the bottom of the rectangular cavity indicate the boundary with the silicon substrate and are simulated in ANSYS by constraining the temperature of this boundary to be 293 K. The top surface of the 3-D model shown in Figure 8.1 is defined as a boundary with the air above it.

A thermal solid element (SOLID 87) is chosen for the simulation and the material properties for different parts of the model are listed in Table 8.1. SOLID 87 has ten nodes, and one degree of freedom, temperature, at each node. It is well suited to model shapes produced from various computer aided design software, e.g. L-Edit.

Table 8.1 Table of thermo-physical properties

Material	Thermal Conductivity (W/m °C)	Specific Heat (J/kg °C)	Density (kg/m^3)
Polysilicon	34.0	700	2320
SiO2	1.4	1400	2190
Al	237	896	2700
Air	0.025	1010	1.21

8.2 Temperature distribution analysis

Temperature distribution on the platform of the micro-radiator operating at a power of 15 mW at 10^{-5} Torr (~10^{-3} Pa) and 740 Torr (~10^{5} Pa) is simulated with both packages. Figure 8.2 shows the result for the temperature distribution on the micro-radiator surface at 10^{-3} Pa simulated with Allegretto's package. Figure 8.3 shows the result simulated with ANSYS. Both results have similar temprature contours. The hottest points on the platform are at the two corners that are furthest away from two supporting arms and are about 1300 K from Allegretto's package and about 1400 K from ANSYS. The difference between two results is less than 10%, which is considered accetable.

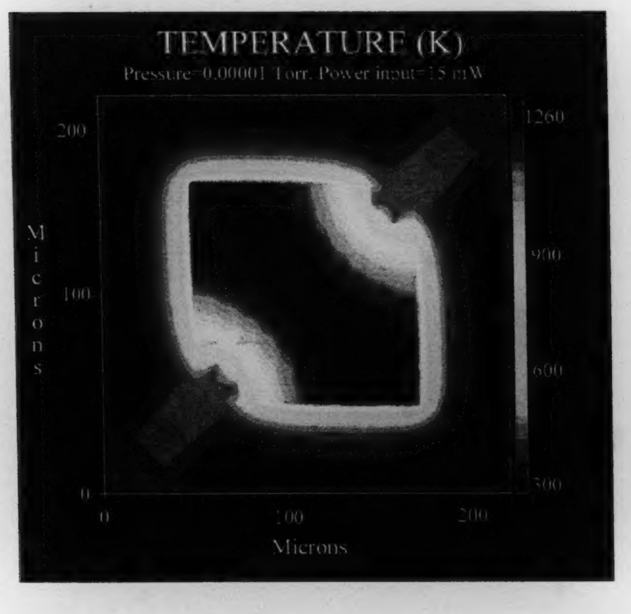

Figure 8.2 Temperature distributions operating at a power of 15 mW at 10^{-3} Pa simulated with Allegretto's package

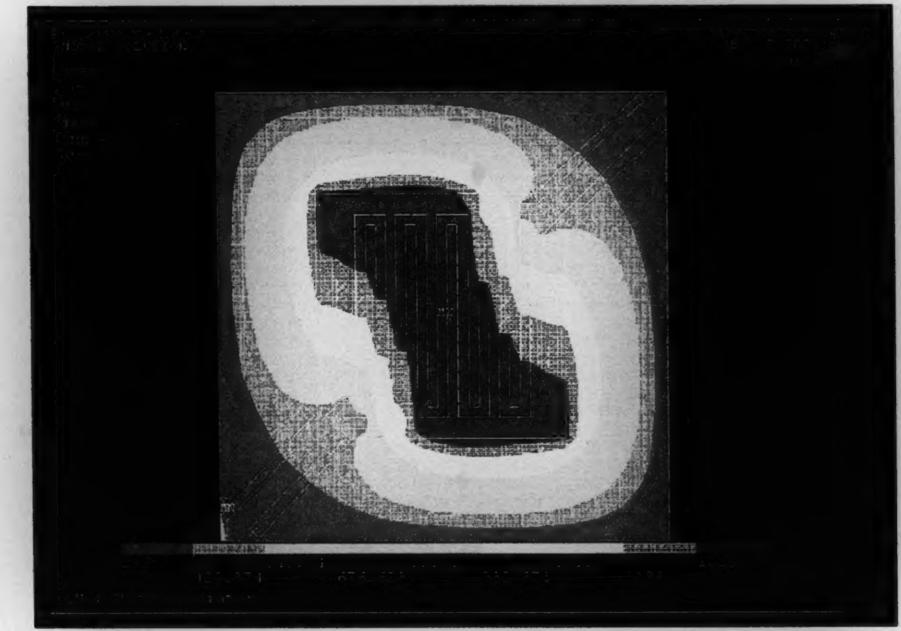

Figure 8.3 Temperature distributions operating at a power of 15 mW at 10^{-3} Pa simulated with ANSYS

Figure 8.4 shows the result for the temperature distribution at 10^5 Pa obtained with Allegretto's package. Figure 8.5 shows the result obtained from ANSYS. The device is cooler due to increased heat transfer from the micro-radiator to the surrounding gas. The hottest point on the platform is at the center of the platform and is about 900 K with an input power of 15 mW. The average temperature of the structure is approximately 700 K, which is the same order of magnitude of the temperature calculated using resistance change in Figure 5.9 (c). Simulations from ANSYS gave similar distribution contours but the orentation of the temperature contour is slightly different to the one obtained with Dr. Allegretto's Package. This is due to the structure mesh used in the ANSYS simulation was not as dense as the mesh used in Dr. Allegretto's package.

Experimental results confirmed the simulation results qualitatively. Figure 8.6 show a picture taken after a micro-radiator had been burnt out with an excessive high power at one atmosphere. The black dot at the center of the platform shows the destruction of the structure material due to heating, indicating the location of the hottest point on the structure.

Figure 8.7 shows the photo taken after a micro-radiator was heated at 10 mW, with pressure decreases from one atmosphere down to 10^{-3} Pa. From the picture we can see the hottest point moves from the center of the platform to the two corners without supporting arms and the glass at these two corners starts to deform. The device did not burn out during experiment, but the room temperature resistance of the device changed permanently after the experiment from 3.9 kΩ to 2.8 kΩ. This is due to the overheating of polysilicon particularly near the two corners without supporting arms.

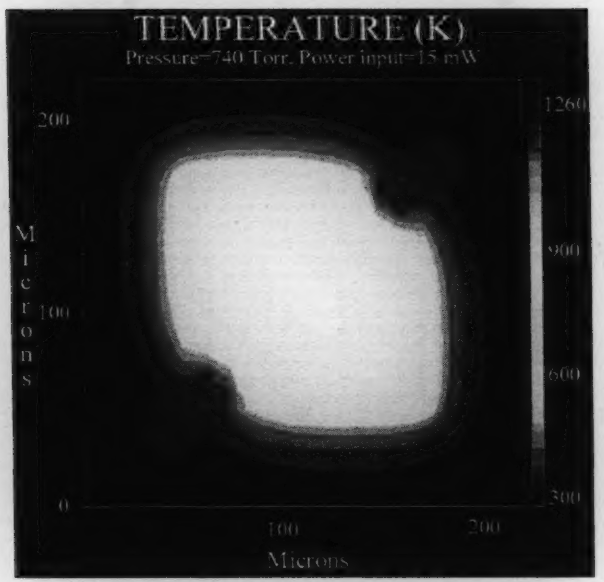

Figure 8.4 Temperature distributions operating at a power of 15 mW at 10^5 Pa simulated with Allegretto's package

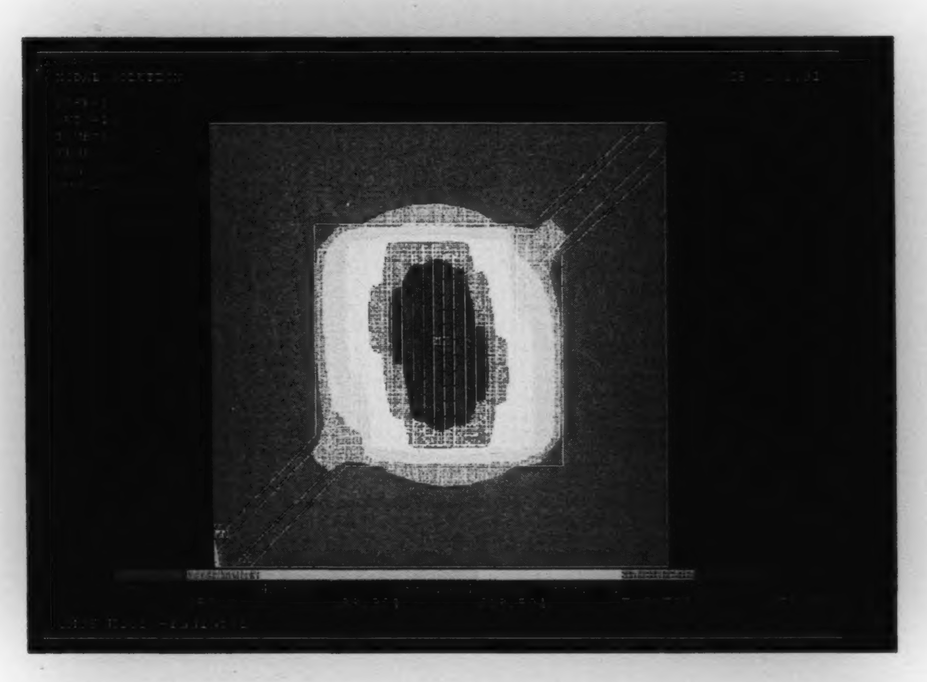

Figure 8.5 Temperature distributions operating at a power of 15 mW at 10^5 Pa simulated with ANSYS

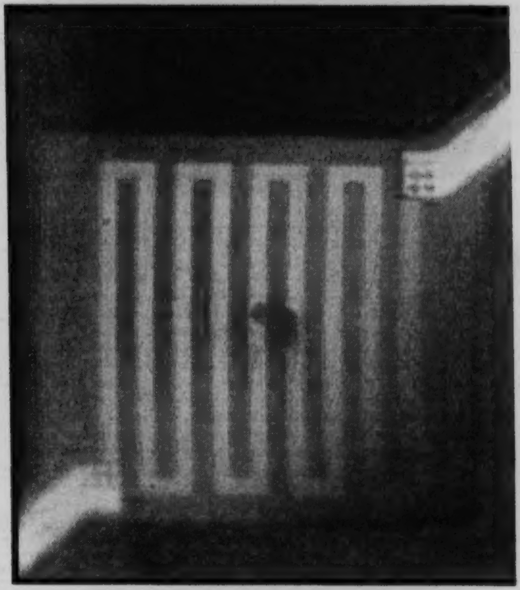

Figure 8.6 Picture of burnt out micro-radiator showing the hottest point at the center of the platform at 10^5 Pa

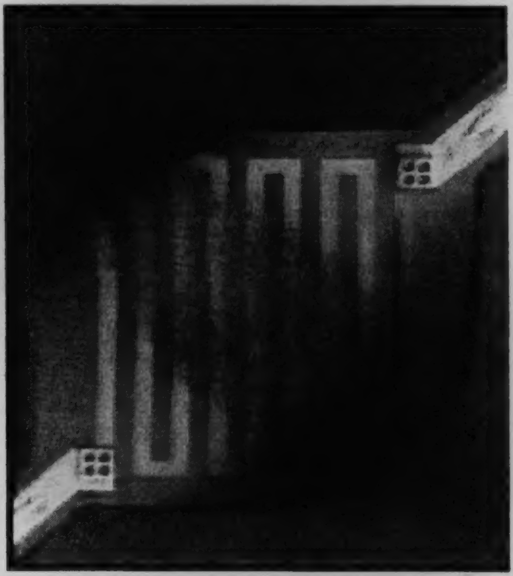

Figure 8.7 Picture of micro-radiator at 10^{-3} Pa showing the hottest point at two corners of the platform without supporting arms

8.3 Radiation calculation

Temperature profile data from the numerical simulation are averaged to calculate the radiation from the micro-radiator using the micro-radiator radiation curve and photodetector response. Output of the photodetector is derived from the response curve of the photodetector output curve in Figure 4.14 and compared with experimental results. Figure 8.8 shows the result from Allegretto's package compared with experimental data operating at a power of 10 mW and pressure range from 0.005 Pa to 10000 Pa. The simulated photodetector output shows a good agreement with experimental data except simulated results are a little smaller than the experimental ones in the middle part of the curve.

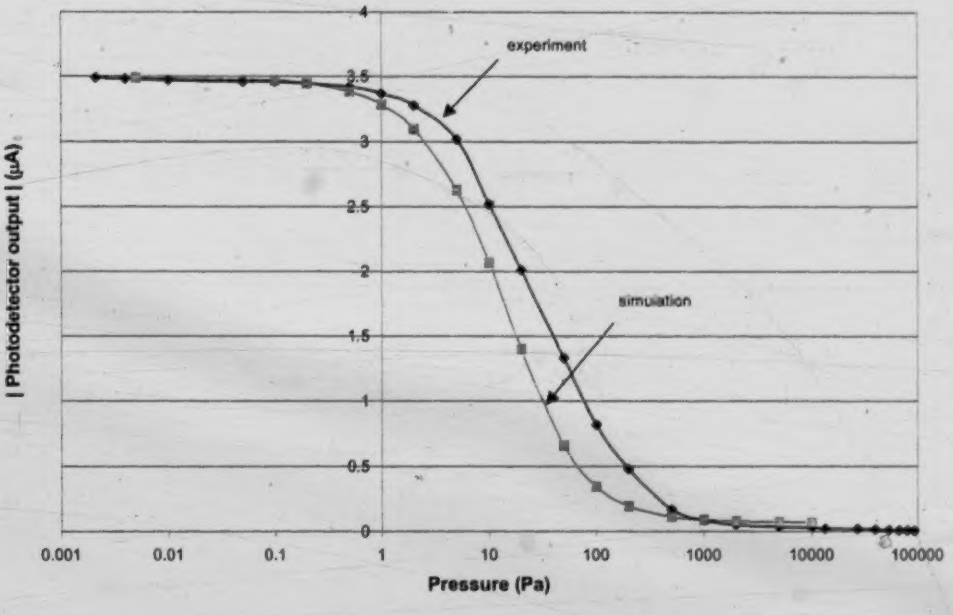

Figure 8.8 Allegretto's simulated photodetector output compared with the experimental data

Although there are limits to the numerical modeling, such as the accuracy of the simulation is dependent on the material parameters; it provided a good way to estimate the temperature distribution of the micro-radiator and guidance for future design optimization.

References:

[1] W. Allegretto, B. Shen, T. Kleckner, and A. M. Robinson, "Micromachined Polysilicon Power Dissipation: Simulation and Experiment", IEEE Transactions on Computer-Aided Design of Integrated Circuits and Systems, Vol. 16, No. 6, June 1997, pp. 627-637.

[2] R. Yeh, "A CIF Conversion Program", Summer Report, Department of Electrical and Computer Engineering, University of Alberta, August 2000.

Chapter 9

Conclusions and Future Work

Conclusions on main achievements and future work of this project are included in this chapter.

9.1 Conclusions

A micro-machined radiator has been designed, tested and calibrated as a thermal conductivity pressure sensor in this project. Test results demonstrate that the polysilicon micro-radiator embedded in a silicon dioxide platform is a good radiation source and measuring the variation of the radiation signal provides a sensitivity at least several orders of magnitude higher than conventional conductivity pressure sensor. Micromachining technology helps to lower the power consumption of the device. The small size of the micro-radiator effectively minimizes the characteristic dimension of the system and therefore increases the upper limit of the sensitive range. A power-switching scheme has been introduced to operate the micro-radiator with constant radiation output to increase the pressure measurement range and extend the lifetime of the device. The pressure measurement range of the micro-radiator with the power-switching scheme is from $10^{-3} - 10^{5}$ Pa.

The optical radiation from the micro-radiator is measured with both commercial photodetector and a three-mode CMOS photodetector. The CMOS photodetector is tested with a point light source and the output is linear to the intensity of incidence light and proportional to the sensitive area of the device. A preliminary integration approach by flip-assembling DIPs of micro-radiator and CMOS photodetector indicates that the CMOS photodetector and micro-radiator can be fully integrated in the future.

A micro-radiator electro-thermal model is built and the photodetector response with the pressure variation is analytically simulated. Two numerical modeling packages are used to simulate the temperature profile of the device. Both analytical and numerical simulation results give a good agreement to the experimental results.

9.2 Future work

There are a few things can be done for the further study of this project.

9.2.1 Micro-radiator matrix design

A micro-radiator matrix has potential application in optical image generation and thermal resolution test targets. Thermal resolution test targets are a matrix of point sources of thermal radiation used for calibrating infrared and thermal sensors [1]. Design of a 2^nx2^m micro-radiator matrix will be discussed in this section.

For a chip containing a large number of devices, such as a MEMS chip with a 2-D matrix of micro-radiators, efficiently using the limited number of I/O pads is essential. CMOS micromachining technology provides the opportunity of on-chip circuitry, which enables multi-device addressing via standard digital decoders and analog switches and greatly reduces the requirement for I/O pads and simplifies the packaging process.

For a $2^n \times 2^m$ micro-radiator matrix, individual control of the micro-radiators can be achieved by using two decoders and ($2^n + 2^m$) n-type Field Effect Transistors (nFET) with CMOS technology as shown in Figure 9.1. The nFETs are operated as electrical switches. The ON/OFF selection of the nFET is controlled by the gate voltage, which is connected to one of the outputs of the decoder. The inputs of the decoders are connected to power VDD. Only one horizontal nFET and one vertical nFET will be switched ON at each time, thus applying electrical power to the corresponding micro-radiator.

However, the MOS transistor is very susceptible to electric static discharge damage (ESD) [2]. Several hundreds volts of ESD is enough to destroy the CMOS decoder and analog switches. Previous 2-D matrix design in the lab failed due to the ESD problem. Proper precautious should be taken in the future on both design and device handling. In design, I/O pads should include ESD protection circuits, such as diodes to sink the excessive currents and diffusion resistor to buffer the shock. A properly designed ESD protection circuit should take up to 10,000 volts of static voltage discharge. In handling, the operator should be properly grounded by wearing a wrist strap and following proper procedures.

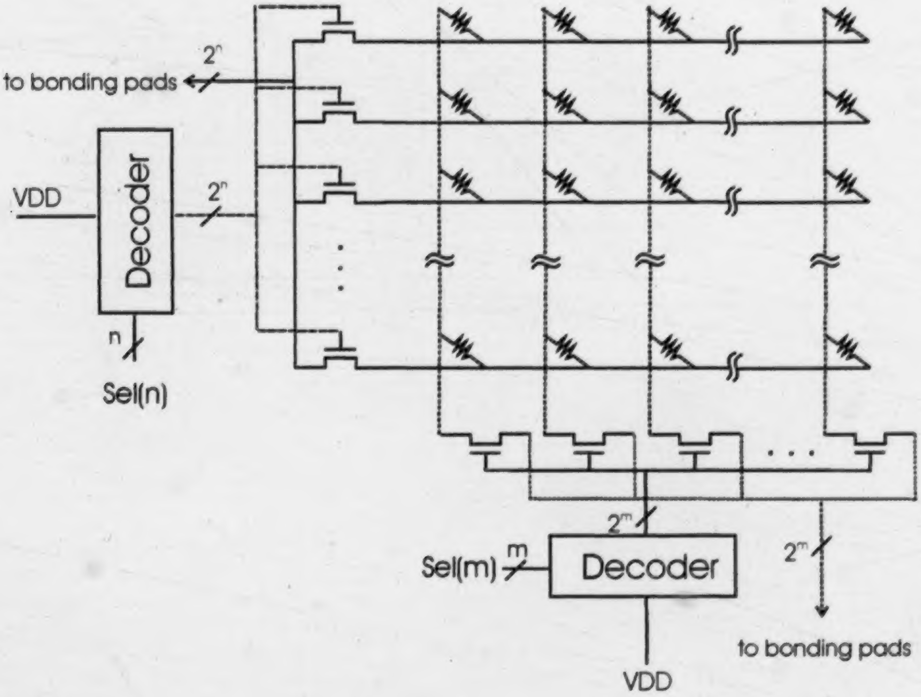

Figure 9.1 Micro-radiator matrix (2^n x 2^m) design

9.2.2 Variation of the characteristic dimension of the system

The characteristic dimension of the system will affect the upper limit of the pressure-sensitive range. The distance between the micro-radiator platform and the bottom of the etched pit in the substrate dominate the characteristic dimension in this project. Only one distance of 85 μm has been used and tested in this project. Future work can be done to increase the upper pressure sensitive limit by introducing a CMOS photodetector as a heat sink above the micro-radiator or reduce the depth of the etched cavity beneath the micro-radiator. However, overheating of the CMOS photodetector will change the response of the photodetector and should be avoided.

9.2.3 Integration of the system

As discussed in Chapter 7, integration of the photodetector with the micro-radiator using a flip-chip process will reduce the distance between the photodetector and the micro-radiator to about 100 μm and the photodetector signal will be increased significantly. A digital amplifier can also be designed on chip with the CMOS photodetector to increase the photodetector output.

9.2.4 Gas analysis using micro-radiator pressure sensing system

The calibration curve of the system depends on the gas in the system as shown in Figure 6.12. Thus the micro-radiator pressure sensing system could possibly be used for gas analysis.

References:

[1] A. P. Pritchard, "Dynamic IR Scene Generation: Basic Requirements and Comparative Display Device Design", Proc. SPIE-940, 1988, pp. 144-149.

[2] G. Bertrand, C. Delage, M. Bafleur et al., "Analysis and compact modeling of a vertical grounded base NPN bipolar transistor used as an ESD protection in a smart power technology", 2000 Bipolar/BiCMOS Circuits and Technology Meeting (BCTM'2000), Minneapolis, USA, 24-26 September 2000, pp.28-31.

Appendix A

Micro-radiator electro-thermal model analysis

This program written in Matlab was used for the electro-thermal model analysis of the micro-radiator. The program plots the temperature versus pressure curve at a certain input power based on the heat balance equation (3.2.17) introduced in Chapter 3.

```
%*************************************
%Micro-radiator electro-thermal model analysis
%*************************************
% temperature range
t = 0:0.1:5000;
% input power in W
w = 0.01;
% room temperature in K
tg= 293;
% micro-radiator surface dimension
x = 120*10^-6;
y = x;
% supporting arm length
e = 85*10^-6;
% distance from micro-radiator to the substrate
s = 85*10^-6;
%
% radiation heat loss
% emissivity
eps = 0.8;
% Stefan-Boltzmann constant
ste = 5.67*10^-8;
% equation (3.2.16)
Kr = 2*eps*ste*x*y;
%
% conduction through arms
% coefficient accounting for 2 supporting arms
eta = 2;
% poly area in the cross-section of the arm (thickness * width)
As1 = 0.32*10^-6*10^-5;
% thermal conductivity of poly
ks1 = 34;
% oxide area in the cross-section of the arm (thickness * width)
As2 = 3.2*10^-6*10^-5;
% thermal conductivity of oxide
ks2 = 1.4;
% equation (3.2.15)
Kcs = eta*(ks1*As1+ks2*As2)/e;
```

```
% conduction through air
% accormmodation coefficient
alpha = 0.9;
% ratio of specific heat of air
gama = 7/5;
% Boltzmann constant
k0 = 1.38*10^-23;
% mass of air molecule
m = 28.98/6.022*10^-23;
% equation (3.2.5)
K= 0.25*(gama+1)/(gama-1)*sqrt(2*k0/3.14159/m/tg)/100;
% coefficient accounting for first order approximation
eda =1.5*x*y/85*10^6;
% equation (3.2.14)
Kcm = K*eda*x*y/s
%
% equation (3.2.19)
p=(w-Kcs*(t-tg)-Kr*(t.^4-tg^4))./Kcm./(t-tg);
%
% plot the results
semilogx(p,t),
hold on;
%
xlabel('Pressure (Pa)'),
ylabel('Temperature (K)'),
axis([0.01,10^4,0,2500]),
```

Appendix B

Experiment control system

B.1 User interface

Figure B.1 shows the user interface of the experimental control system.

The power level is specified by the user in the *Pulse Definition* part and can be either constant or can be a custom waveform. *Level* parameter specifies the magnitude of the power P in watts. Two columns correspond to two pulses. The length of each pulse is specified with *Duration*. *MFactor* and *AFactor* are two factors to define the growth of the new pulses. For example, after the first two pulses defined by *Level* and *Duration*, the magnitude of the new pulses P' will be $P' = P * (MFactor) + (AFactor)$. *Total Duration time* defines how long you wish to run the analysis. The present resistance of the micro-radiator being tested can be viewed at anytime in the top graph window so that the user can monitor the progress of the experiment while it is being run, and stop and restart the experiment at any time.

The system is also designed to have a data compression function to reduce data file sizes. The *Sensitivity* specifies which changes in power, resistance or photodiode signal will merit the data being written to file. If these quantities change by less than that specified by *Sensitivity*, data is not stored. The *Max. Power* threshold is used as a safety precaution to protect the polysilicon resistor being damaged by excessive heating. The *Alpha* value is the TCR of polysilicon; it is used to approximately calculate the temperature of the polysilicon as a reference. *Notes or Comments* will be written to the first line of the data file. The button *Data File* is used to open or create a new data file for an analysis. The button *Start Analysis* is used to start an analysis. The check boxes *Stop Analysis* and *Freeze Display* are designed for the user to stop analysis or freeze display at any stage of the experiment.

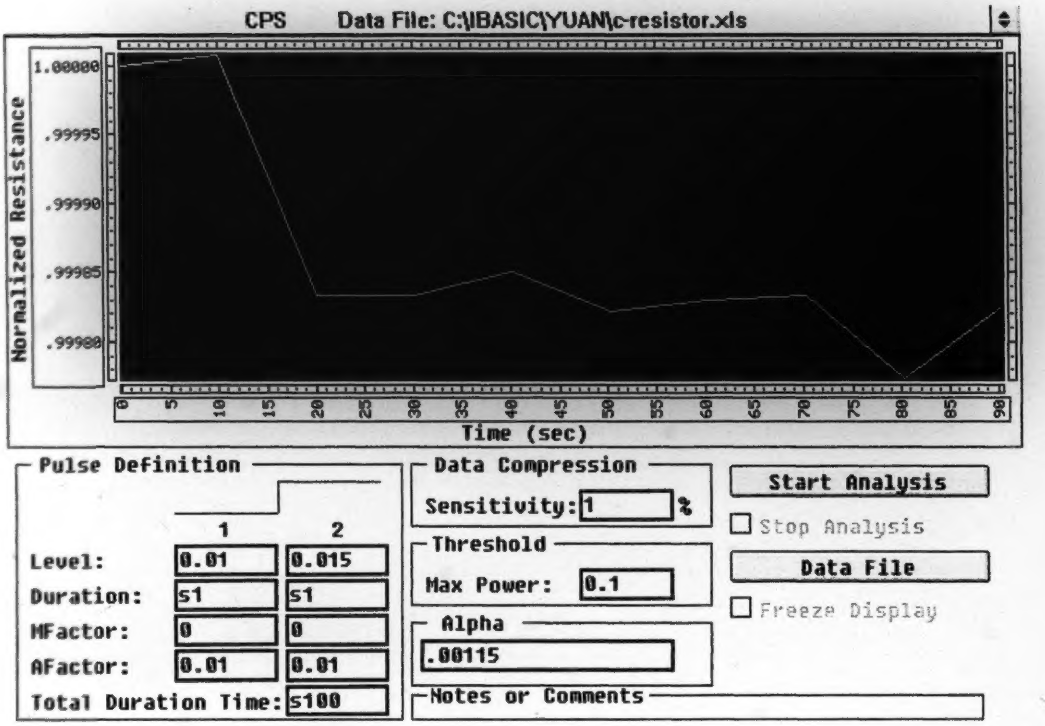

Data File: C:\IBASIC\YUAN\c-resistor.xls

	1	2
Level:	0.01	0.015
Duration:	s1	s1
MFactor:	0	0
AFactor:	0.01	0.01

Total Duration Time: s100

Sensitivity: 1 %

Max Power: 0.1

Alpha: .00115

Figure B.1 Constant power supply unit user interface

B.2 Experiment control system flow chart

The experimental control system is built with a convergent loop algorithm. A simplified flow chart of the program is shown in Figure B.2. The Source Measure Unit (SMU) supplies current *(I)* and simultaneously measures voltage (*V*). The Digital Multimeter (DMM) measures the output of the photodiode *(Ip)*. The program sets up the SMU and DMM at the beginning of the program and a small current I_0 is sent by the SMU to the micro-radiator and the voltage across the micro-radiator is measured to calculate the room temperature resistance of the micro-radiator R_0. Then the current *(I)* required to heat the micro-radiator to the specified power (P_{set}) is then calculated and send to the micro-radiator with the voltage *(V)* being measured at the same time:

$$I = \sqrt{P_{set} / R_0} \tag{B.1}$$

The updated power *(P)* and resistance *(R)* are calculated by:

$$P = I \cdot V \quad \text{and} \quad R = V / I \tag{B.2}$$

Then some judgment needs to be made to see if the total duration time has expired or if the power is too high. Then the changes of power, resistance and photodetector signal are calculated and if the change of any parameter is bigger than the sensitivity, the data are recorded in the data file. If the power doesn't exceed the maximum power, the new current *I'* will be calculated according to the updated resistance and sent to the micro-radiator, starting the loop again:

$$I' = \sqrt{P_{set} / R} \tag{B.3}$$

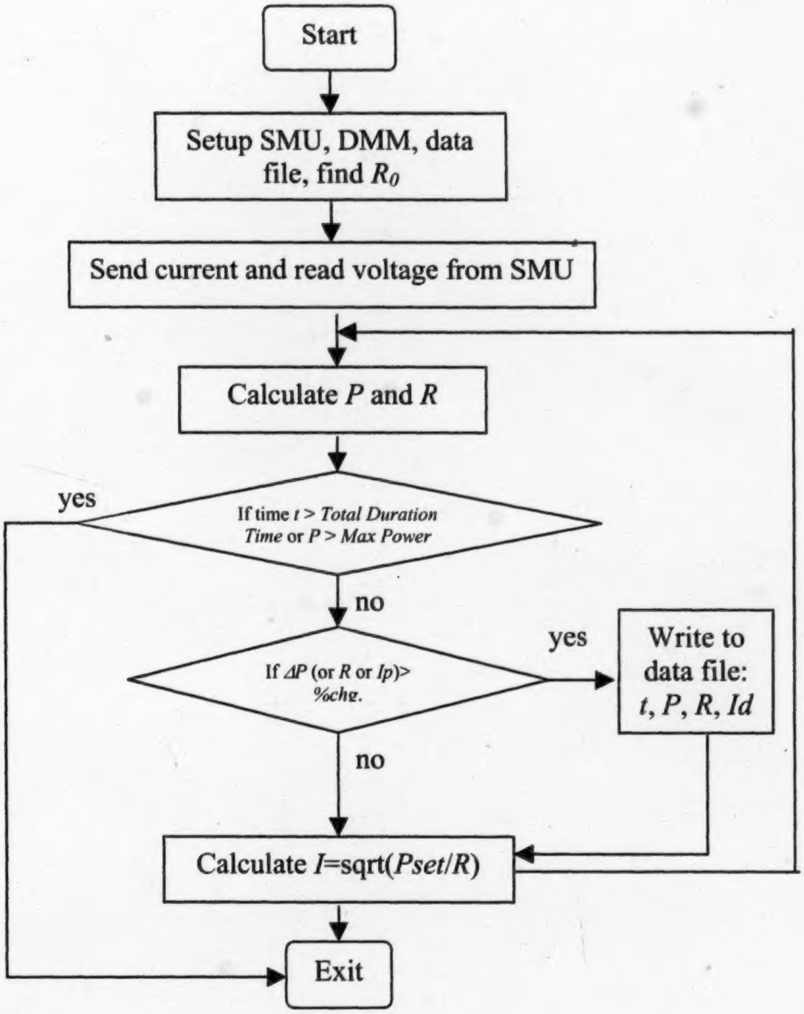
Start
Setup SMU, DMM, data file, find R_0
Send current and read voltage from SMU
Calculate P and R
yes
If time t > Total Duration Time or P > Max Power
no
yes
If ΔP (or R or Ip)> %chg.
Write to data file: t, P, R, Id
no
Calculate I=sqrt($Pset/R$)
Exit

Figure B.2 Simplified flow-chart of the digital constant power supply unit and data acquisition unit

B.3 Experimental control system program

```
10 !-----------------------------------------------------------------!
20 !-----------------------------------------------------------------!
30      REAL Vpoly,Ipoly,Rpoly,Pset,Psetold,Rpolyold,Vpolyold,Ipolyold,Rinit,Plotmax
40      REAL Inittime,Oldtime,Newtime,Savetime,Pulsestart,Pulsetime,Plottime
50      REAL Tim1,Tim2,Tim3,Fac1,Fac2,Plu1,Plu2,Seni,Sen,Thre,Rtem,Alph,Idold,Id
60      REAL Rpolyroom,Atem,Atemold,Runningave
61      REAL Psetsign,Psetoldsign
70      DIM Temp$[50]
80      DIM File$[50]
90      DIM Notes$[256]
100     REAL Rplot(1:8640),Timevalue(1:8640)
110     INTEGER Acount,Acountupper,Rsetflag,Stopflag,Stopdis,Errnum,Thresflag
120     File$=""
130     Errnum=0
140     Thresflag=0
150     Stopflag=0
160     GOSUB Makepanel
170     ON EVENT @Astart,"ACTIVATED" GOSUB Mainstart
180     ON EVENT @Dfile,"ACTIVATED" GOSUB Datafile
190     ON ERROR GOTO Errorhandler
200     LOOP
210     END LOOP
220 !-----------------------------------------------------------------!
230 ! If specified file does not exist, it is created
240 !-----------------------------------------------------------------!
250 Errorhandler:!
260    IF ERRN=56 THEN
270       CREATE File$,1
280       ASSIGN @File TO File$;FORMAT ON
290    END IF
300    IF ERRN=32 AND Errnum=0 THEN
310       Errnum=1
320       DIALOG "WARNING","Error in numerical data"
330    END IF
340    RETURN
350 !-----------------------------------------------------------------!
360 Mainstart:!
370    STATUS @Lev1;RETURN("VALUE":Lev1$)
380    STATUS @Lev2;RETURN("VALUE":Lev2$)
390    STATUS @Tim1;RETURN("VALUE":Tim1$)
400    STATUS @Tim2;RETURN("VALUE":Tim2$)
410    STATUS @Fac1;RETURN("VALUE":Fac1$)
420    STATUS @Fac2;RETURN("VALUE":Fac2$)
430    STATUS @Add1;RETURN("VALUE":Add1$)
440    STATUS @Add2;RETURN("VALUE":Add2$)
450    STATUS @Tim3;RETURN("VALUE":Tim3$)
460    STATUS @Sen1;RETURN("VALUE":Sen1$)
470    STATUS @Thres;RETURN("VALUE":Thres$)
480    STATUS @Notes;RETURN("VALUE":Notes$)
481    STATUS @Alphe;RETURN("VALUE":Alpha$)
490    !
500    IF Lev1$="" OR Lev2$="" OR Tim1$="" OR Tim2$="" OR Fac1$="" OR Fac2$="" OR Add1$=""
OR Add2$="" OR Tim3$="" OR Sen1$="" OR Thres$="" OR File$="" THEN
501       DIALOG "WARNING","All necessary data not available"
520    ELSE
530       Errnum=0
540       Lev1=VAL(Lev1$)
550       IF Lev1=0 THEN
560          Lev1=2.5E-5
570       END IF
580       Lev2=VAL(Lev2$)
590       IF Lev2=0 THEN
600          Lev2=2.5E-5
610       END IF
620  !
630       IF Tim1$[1;1]="s" THEN
```

```
640           Tim1=VAL(Tim1$[2;8])
650        END IF
660        IF Tim1$[1;1]="m" THEN
670           Tim1=VAL(Tim1$[2;8])*60
680        END IF
690        IF Tim1$[1;1]="h" THEN
700           Tim1=VAL(Tim1$[2;8])*3600
710        END IF
720        IF Tim1$[1;1]="d" THEN
730           Tim1=VAL(Tim1$[2;8])*86400
740        END IF
750  !
760        IF Tim2$[1;1]="s" THEN
770           Tim2=VAL(Tim2$[2;8])
780        END IF
790        IF Tim2$[1;1]="m" THEN
800           Tim2=VAL(Tim2$[2;8])*60
810        END IF
820        IF Tim2$[1;1]="h" THEN
830           Tim2=VAL(Tim2$[2;8])*3600
840        END IF
850        IF Tim2$[1;1]="d" THEN
860           Tim2=VAL(Tim2$[2;8])*86400
870        END IF
880  !
890        IF Tim3$[1;1]="s" THEN
900           Tim3=VAL(Tim3$[2;8])
910        END IF
920        IF Tim3$[1;1]="m" THEN
930           Tim3=VAL(Tim3$[2;8])*60.
940        END IF
950        IF Tim3$[1;1]="h" THEN
960           Tim3=VAL(Tim3$[2;8])*3600.
970        END IF
980        IF Tim3$[1;1]="d" THEN
990           Tim3=VAL(Tim3$[2;8])*86400
1000       END IF
1010 !
1020       Fac1=VAL(Fac1$)
1030       Fac2=VAL(Fac2$)
1040       Plu1=VAL(Add1$)
1050       Plu2=VAL(Add2$)
1060       Seni=VAL(Sen1$)
1070       Thre=VAL(Thres$)
1071       Rtemp$="25"
1080       Rtem=25.
1081       IF Alpha$="" THEN
1082          Alpha$="0.00115"
1083          Alph=.00115
1084       ELSE
1090          Alph=VAL(Alpha$)
1091       END IF
1100       IF Errnum=1 THEN
1110          RETURN
1120       END IF
1130 !
1140       CONTROL @Astart;SET("SENSITIVE":0)
1150       CONTROL @Astop;SET("SENSITIVE":1)
1151       CONTROL @Dstop;SET("SENSITIVE":1)
1160       GOSUB Constantpower
1170       IF Stopflag=0 THEN
1180          IF Thresflag=0 THEN
1190             DIALOG "INFORMATION","Analysis Complete"
1200          ELSE
1210             DIALOG "INFORMATION","Terminated: Max Power Exceeded"
1220          END IF
1230       ELSE
1240          DIALOG "INFORMATION","Terminated: Stopped By User"
1250       END IF
1260       CONTROL @Astart;SET("SENSITIVE":1)
```

```
1270      CONTROL @Astop;SET("VALUE":0)
1280      CONTROL @Astop;SET("SENSITIVE":0)
1281      CONTROL @Dstop;SET("VALUE":0)
1282      CONTROL @Dstop;SET("SENSITIVE":0)
1290   END IF
1300   RETURN
1310 !----------------------------------------------------------------!
1320 !----------------------------------------------------------------!
1330 ! Define datafile Subroutine
1340 !----------------------------------------------------------------!
1350 Datafile:!
1360 Msg$="Select A Data File"
1370 DIALOG "FILE",Msg$;SET("PATTERN":"*.XLS"),RETURN("SELECTION":File$)
1380 CONTROL @Mainpanel;SET("TITLE":"CPS        Data File: "&File$)
1390 RETURN
1400 !----------------------------------------------------------------!
1410 ! Define Main Panel Subroutine
1420 !----------------------------------------------------------------!
1430 Makepanel:!
1440 ASSIGN @Mainpanel TO WIDGET "PANEL";SET("TITLE":"CPS")
1450 !
1460 !
1470 ! 1) Definition of Plotting Area
1480 ASSIGN @Plot TO WIDGET "XY GRAPH";SET("VISIBLE":0),PARENT @Mainpanel
1490    CONTROL @Plot;SET("TRACE BACKGROUND":0)
1500    CONTROL @Plot;SET("X":0)
1510    CONTROL @Plot;SET("Y":0)
1520    CONTROL @Plot;SET("HEIGHT":260)
1530    CONTROL @Plot;SET("WIDTH":640)
1540 !  CONTROL @Plot;SET("TRACE COUNT":1)
1550    CONTROL @Plot;SET("CURRENT AXIS":"X","AXIS LABEL":"Time (sec)")
1560    CONTROL @Plot;SET("AUTOSCALE":1)
1570    CONTROL @Plot;SET("CURRENT AXIS":"Y","AXIS LABEL":"Normalized Resistance")
1580    CONTROL @Plot;SET("AUTOSCALE":1)
1590    CONTROL @Plot;SET("CURRENT TRACE":1)
1600    CONTROL @Plot;SET("VISIBLE":1)
1610 !
1620 !-----------------------------------------------------------------
1630 ! 2) Definition of pulse Definition panel
1640 ASSIGN @Pulse TO WIDGET "PANEL";PARENT @Mainpanel
1650     CONTROL @Pulse;SET("VISIBLE":0)
1660     CONTROL @Pulse;SET("X":5)
1670     CONTROL @Pulse;SET("Y":270)
1680     CONTROL @Pulse;SET("HEIGHT":185)
1690     CONTROL @Pulse;SET("WIDTH":245)
1700     CONTROL @Pulse;SET("BORDER":1)
1710     CONTROL @Pulse;SET("VISIBLE":1)
1720 ASSIGN @Plabel TO WIDGET "LABEL";PARENT @Mainpanel
1730     CONTROL @Plabel;SET("VISIBLE":0)
1740     CONTROL @Plabel;SET("X":15)
1750     CONTROL @Plabel;SET("Y":260)
1760     CONTROL @Plabel;SET("HEIGHT":20)
1770     CONTROL @Plabel;SET("WIDTH":140)
1780     CONTROL @Plabel;SET("BORDER":0)
1790     CONTROL @Plabel;SET("VALUE":"Pulse Definition")
1800     CONTROL @Plabel;SET("JUSTIFICATION":"CENTER")
1810     CONTROL @Plabel;SET("VISIBLE":1)
1820 ASSIGN @Pheader TO WIDGET "LABEL";PARENT @Pulse
1830     CONTROL @Pheader;SET("VISIBLE":0)
1840     CONTROL @Pheader;SET("X":100)
1850     CONTROL @Pheader;SET("Y":30)
1860     CONTROL @Pheader;SET("HEIGHT":20)
1870     CONTROL @Pheader;SET("WIDTH":120)
1880     CONTROL @Pheader;SET("BORDER":0)
1890     CONTROL @Pheader;SET("VALUE":"   1       2")
1900     CONTROL @Pheader;SET("JUSTIFICATION":"LEFT")
1910     CONTROL @Pheader;SET("VISIBLE":1)
1920 !
1930 ! Draw diagram
1940 !
```

```
1950 ASSIGN @Pline1 TO WIDGET "LABEL";PARENT @Pulse
1960      CONTROL @Pline1;SET("X":100)
1970      CONTROL @Pline1;SET("Y":30)
1980      CONTROL @Pline1;SET("HEIGHT":1)
1990      CONTROL @Pline1;SET("WIDTH":65)
2000      CONTROL @Pline1;SET("BORDER":1)
2010      CONTROL @Pline1;SET("VALUE":" ")
2020      CONTROL @Pline1;SET("VISIBLE":1)
2030 ASSIGN @Pline2 TO WIDGET "LABEL";PARENT @Pulse
2040      CONTROL @Pline2;SET("X":165)
2050      CONTROL @Pline2;SET("Y":10)
2060      CONTROL @Pline2;SET("HEIGHT":20)
2070      CONTROL @Pline2;SET("WIDTH":1)
2080      CONTROL @Pline2;SET("BORDER":1)
2090      CONTROL @Pline2;SET("VALUE":" ")
2100      CONTROL @Pline2;SET("VISIBLE":1)
2110 ASSIGN @Pline3 TO WIDGET "LABEL";PARENT @Pulse
2120      CONTROL @Pline3;SET("X":165)
2130      CONTROL @Pline3;SET("Y":10)
2140      CONTROL @Pline3;SET("HEIGHT":1)
2150      CONTROL @Pline3;SET("WIDTH":65)
2160      CONTROL @Pline3;SET("BORDER":1)
2170      CONTROL @Pline3;SET("VALUE":" ")
2180      CONTROL @Pline3;SET("VISIBLE":1)
2190 !
2200 ASSIGN @Plevel TO WIDGET "LABEL";PARENT @Pulse
2210      CONTROL @Plevel;SET("VISIBLE":0)
2220      CONTROL @Plevel;SET("X":5)
2230      CONTROL @Plevel;SET("Y":50)
2240      CONTROL @Plevel;SET("HEIGHT":20)
2250      CONTROL @Plevel;SET("WIDTH":80)
2260      CONTROL @Plevel;SET("BORDER":0)
2270      CONTROL @Plevel;SET("VALUE":"Level:")
2280      CONTROL @Plevel;SET("JUSTIFICATION":"LEFT")
2290      CONTROL @Plevel;SET("VISIBLE":1)
2300 ASSIGN @Pdtime TO WIDGET "LABEL";PARENT @Pulse
2310      CONTROL @Pdtime;SET("VISIBLE":0)
2320      CONTROL @Pdtime;SET("X":5)
2330      CONTROL @Pdtime;SET("Y":72)
2340      CONTROL @Pdtime;SET("HEIGHT":20)
2350      CONTROL @Pdtime;SET("WIDTH":80)
2360      CONTROL @Pdtime;SET("BORDER":0)
2370      CONTROL @Pdtime;SET("VALUE":"Duration:")
2380      CONTROL @Pdtime;SET("JUSTIFICATION":"LEFT")
2390      CONTROL @Pdtime;SET("VISIBLE":1)
2400 ASSIGN @Pmfac TO WIDGET "LABEL";PARENT @Pulse
2410      CONTROL @Pmfac;SET("VISIBLE":0)
2420      CONTROL @Pmfac;SET("X":5)
2430      CONTROL @Pmfac;SET("Y":94)
2440      CONTROL @Pmfac;SET("HEIGHT":20)
2450      CONTROL @Pmfac;SET("WIDTH":80)
2460      CONTROL @Pmfac;SET("BORDER":0)
2470      CONTROL @Pmfac;SET("VALUE":"MFactor:")
2480      CONTROL @Pmfac;SET("JUSTIFICATION":"LEFT")
2490      CONTROL @Pmfac;SET("VISIBLE":1)
2500 ASSIGN @Pafac TO WIDGET "LABEL";PARENT @Pulse
2510      CONTROL @Pafac;SET("VISIBLE":0)
2520      CONTROL @Pafac;SET("X":5)
2530      CONTROL @Pafac;SET("Y":116)
2540      CONTROL @Pafac;SET("HEIGHT":20)
2550      CONTROL @Pafac;SET("WIDTH":80)
2560      CONTROL @Pafac;SET("BORDER":0)
2570      CONTROL @Pafac;SET("VALUE":"AFactor:")
2580      CONTROL @Pafac;SET("JUSTIFICATION":"LEFT")
2590      CONTROL @Pafac;SET("VISIBLE":1)
2600 ASSIGN @Pttime TO WIDGET "LABEL";PARENT @Pulse
2610      CONTROL @Pttime;SET("VISIBLE":0)
2620      CONTROL @Pttime;SET("X":5)
2630      CONTROL @Pttime;SET("Y":138)
2640      CONTROL @Pttime;SET("HEIGHT":20)
```

```
2650     CONTROL @Pttime;SET("WIDTH":165)
2660     CONTROL @Pttime;SET("BORDER":0)
2670     CONTROL @Pttime;SET("VALUE":"Total Duration Time:")
2680     CONTROL @Pttime;SET("JUSTIFICATION":"LEFT")
2690     CONTROL @Pttime;SET("VISIBLE":1)
2700 ASSIGN @Pequ TO WIDGET "LABEL";PARENT @Pulse
2710     CONTROL @Pequ;SET("VISIBLE":0)
2720     CONTROL @Pequ;SET("X":22)
2730     CONTROL @Pequ;SET("Y":160)
2740     CONTROL @Pequ;SET("HEIGHT":20)
2750     CONTROL @Pequ;SET("WIDTH":220)
2760     CONTROL @Pequ;SET("BORDER":0)
2770     CONTROL @Pequ;SET("VALUE":"P=P'*(Mfactor)+(Afactor)")
2780     CONTROL @Pequ;SET("JUSTIFICATION":"LEFT")
2790     CONTROL @Pequ;SET("VISIBLE":1)
2800 !
2810 !
2820 ! 2b) Definition of Pulse Definition Edit boxes
2830 ASSIGN @Lev1 TO WIDGET "STRING";PARENT @Pulse
2840     CONTROL @Lev1;SET("VISIBLE":0)
2850     CONTROL @Lev1;SET("X":100)
2860     CONTROL @Lev1;SET("Y":50)
2870     CONTROL @Lev1;SET("HEIGHT":20)
2880     CONTROL @Lev1;SET("WIDTH":65)
2890     CONTROL @Lev1;SET("BORDER":1)
2900     CONTROL @Lev1;SET("VISIBLE":1)
2910 ASSIGN @Lev2 TO WIDGET "STRING";PARENT @Pulse
2920     CONTROL @Lev2;SET("VISIBLE":0)
2930     CONTROL @Lev2;SET("X":170)
2940     CONTROL @Lev2;SET("Y":50)
2950     CONTROL @Lev2;SET("HEIGHT":20)
2960     CONTROL @Lev2;SET("WIDTH":65)
2970     CONTROL @Lev2;SET("BORDER":1)
2980     CONTROL @Lev2;SET("VISIBLE":1)
2990 ASSIGN @Tim1 TO WIDGET "STRING";PARENT @Pulse
3000     CONTROL @Tim1;SET("VISIBLE":0)
3010     CONTROL @Tim1;SET("X":100)
3020     CONTROL @Tim1;SET("Y":72)
3030     CONTROL @Tim1;SET("HEIGHT":20)
3040     CONTROL @Tim1;SET("WIDTH":65)
3050     CONTROL @Tim1;SET("BORDER":1)
3060     CONTROL @Tim1;SET("VISIBLE":1)
3070 ASSIGN @Tim2 TO WIDGET "STRING";PARENT @Pulse
3080     CONTROL @Tim2;SET("VISIBLE":0)
3090     CONTROL @Tim2;SET("X":170)
3100     CONTROL @Tim2;SET("Y":72)
3110     CONTROL @Tim2;SET("HEIGHT":20)
3120     CONTROL @Tim2;SET("WIDTH":65)
3130     CONTROL @Tim2;SET("BORDER":1)
3140     CONTROL @Tim2;SET("VISIBLE":1)
3150 ASSIGN @Fac1 TO WIDGET "STRING";PARENT @Pulse
3160     CONTROL @Fac1;SET("VISIBLE":0)
3170     CONTROL @Fac1;SET("X":100)
3180     CONTROL @Fac1;SET("Y":94)
3190     CONTROL @Fac1;SET("HEIGHT":20)
3200     CONTROL @Fac1;SET("WIDTH":65)
3210     CONTROL @Fac1;SET("BORDER":1)
3220     CONTROL @Fac1;SET("VISIBLE":1)
3230 ASSIGN @Fac2 TO WIDGET "STRING";PARENT @Pulse
3240     CONTROL @Fac2;SET("VISIBLE":0)
3250     CONTROL @Fac2;SET("X":170)
3260     CONTROL @Fac2;SET("Y":94)
3270     CONTROL @Fac2;SET("HEIGHT":20)
3280     CONTROL @Fac2;SET("WIDTH":65)
3290     CONTROL @Fac2;SET("BORDER":1)
3300     CONTROL @Fac2;SET("VISIBLE":1)
3310 ASSIGN @Add1 TO WIDGET "STRING";PARENT @Pulse
3320     CONTROL @Add1;SET("VISIBLE":0)
3330     CONTROL @Add1;SET("X":100)
3340     CONTROL @Add1;SET("Y":116)
```

```
3350     CONTROL @Add1;SET("HEIGHT":20)
3360     CONTROL @Add1;SET("WIDTH":65)
3370     CONTROL @Add1;SET("BORDER":1)
3380     CONTROL @Add1;SET("VISIBLE":1)
3390 ASSIGN @Add2 TO WIDGET "STRING";PARENT @Pulse
3400     CONTROL @Add2;SET("VISIBLE":0)
3410     CONTROL @Add2;SET("X":170)
3420     CONTROL @Add2;SET("Y":116)
3430     CONTROL @Add2;SET("HEIGHT":20)
3440     CONTROL @Add2;SET("WIDTH":65)
3450     CONTROL @Add2;SET("BORDER":1)
3460     CONTROL @Add2;SET("VISIBLE":1)
3470 ASSIGN @Tim3 TO WIDGET "STRING";PARENT @Pulse
3480     CONTROL @Tim3;SET("VISIBLE":0)
3490     CONTROL @Tim3;SET("X":170)
3500     CONTROL @Tim3;SET("Y":138)
3510     CONTROL @Tim3;SET("HEIGHT":20)
3520     CONTROL @Tim3;SET("WIDTH":65)
3530     CONTROL @Tim3;SET("BORDER":1)
3540     CONTROL @Tim3;SET("VISIBLE":1)
3550 !
3560 !-------------------------------------------------------------------
3570 ! 3) Definition of Date compression panel
3580 ASSIGN @Dcompress TO WIDGET "PANEL";PARENT @Mainpanel
3590     CONTROL @Dcompress;SET("VISIBLE":0)
3600     CONTROL @Dcompress;SET("X":255)
3610     CONTROL @Dcompress;SET("Y":270)
3620     CONTROL @Dcompress;SET("HEIGHT":40)
3630     CONTROL @Dcompress;SET("WIDTH":190)
3640     CONTROL @Dcompress;SET("BORDER":1)
3650     CONTROL @Dcompress;SET("VISIBLE":1)
3660 ASSIGN @Dlabel TO WIDGET "LABEL";PARENT @Mainpanel
3670     CONTROL @Dlabel;SET("VISIBLE":0)
3680     CONTROL @Dlabel;SET("X":265)
3690     CONTROL @Dlabel;SET("Y":260)
3700     CONTROL @Dlabel;SET("HEIGHT":20)
3710     CONTROL @Dlabel;SET("WIDTH":140)
3720     CONTROL @Dlabel;SET("BORDER":0)
3730     CONTROL @Dlabel;SET("VALUE":"Data Compression")
3740     CONTROL @Dlabel;SET("JUSTIFICATION":"CENTER")
3750     CONTROL @Dlabel;SET("VISIBLE":1)
3760 ASSIGN @Dsensitive TO WIDGET "LABEL";PARENT @Dcompress
3770     CONTROL @Dsensitive;SET("VISIBLE":0)
3780     CONTROL @Dsensitive;SET("X":5)
3790     CONTROL @Dsensitive;SET("Y":15)
3800     CONTROL @Dsensitive;SET("HEIGHT":20)
3810     CONTROL @Dsensitive;SET("WIDTH":190)
3820     CONTROL @Dsensitive;SET("BORDER":0)
3830     CONTROL @Dsensitive;SET("VALUE":"Sensitivity:         %")
3840     CONTROL @Dsensitive;SET("JUSTIFICATION":"LEFT")
3850     CONTROL @Dsensitive;SET("VISIBLE":1)
3860 !
3870 !
3880 ! 3a) Definition of Data compression edit boxes
3890 ASSIGN @Sen1 TO WIDGET "STRING";PARENT @Dcompress
3900     CONTROL @Sen1;SET("VISIBLE":0)
3910     CONTROL @Sen1;SET("X":105)
3920     CONTROL @Sen1;SET("Y":15)
3930     CONTROL @Sen1;SET("HEIGHT":20)
3940     CONTROL @Sen1;SET("WIDTH":60)
3950     CONTROL @Sen1;SET("BORDER":1)
3960     CONTROL @Sen1;SET("VISIBLE":1)
3970 !
3980 !-------------------------------------------------------------------
3990 !
4000 ! 4) Definition of Threshold panel
4010 ASSIGN @Threshold TO WIDGET "PANEL";PARENT @Mainpanel
4020     CONTROL @Threshold;SET("VISIBLE":0)
4030     CONTROL @Threshold;SET("X":255)
4040     CONTROL @Threshold;SET("Y":320)
```

```
4050     CONTROL @Threshold;SET("HEIGHT":40)
4060     CONTROL @Threshold;SET("WIDTH":190)
4070     CONTROL @Threshold;SET("BORDER":1)
4080     CONTROL @Threshold;SET("VISIBLE":1)
4090 ASSIGN @Tlabel TO WIDGET "LABEL";PARENT @Mainpanel
4100     CONTROL @Tlabel;SET("VISIBLE":0)
4110     CONTROL @Tlabel;SET("X":265)
4120     CONTROL @Tlabel;SET("Y":310)
4130     CONTROL @Tlabel;SET("HEIGHT":20)
4140     CONTROL @Tlabel;SET("WIDTH":80)
4150     CONTROL @Tlabel;SET("BORDER":0)
4160     CONTROL @Tlabel;SET("VALUE":"Threshold")
4170     CONTROL @Tlabel;SET("JUSTIFICATION":"CENTER")
4180     CONTROL @Tlabel;SET("VISIBLE":1)
4190 ASSIGN @Maxp TO WIDGET "LABEL";PARENT @Threshold
4200     CONTROL @Maxp;SET("VISIBLE":0)
4210     CONTROL @Maxp;SET("X":5)
4220     CONTROL @Maxp;SET("Y":15)
4230     CONTROL @Maxp;SET("HEIGHT":20)
4240     CONTROL @Maxp;SET("WIDTH":120)
4250     CONTROL @Maxp;SET("BORDER":0)
4260     CONTROL @Maxp;SET("VALUE":"Max Power:")
4270     CONTROL @Maxp;SET("JUSTIFICATION":"LEFT")
4280     CONTROL @Maxp;SET("VISIBLE":1)
4290 !
4300 !
4310 ! 4a) Definition of Data compression edit boxes
4320 ASSIGN @Thres TO WIDGET "STRING";PARENT @Threshold
4330     CONTROL @Thres;SET("VISIBLE":0)
4340     CONTROL @Thres;SET("X":105)
4350     CONTROL @Thres;SET("Y":15)
4360     CONTROL @Thres;SET("HEIGHT":20)
4370     CONTROL @Thres;SET("WIDTH":60)
4380     CONTROL @Thres;SET("BORDER":1)
4390     CONTROL @Thres;SET("VISIBLE":1)
4400 !
4410 !
4420 ! 5) Definition of view panel apply and stop pushbuttons
4430 ASSIGN @Astart TO WIDGET "PUSHBUTTON";PARENT @Mainpanel
4440       CONTROL @Astart;SET("VISIBLE":0)
4450       CONTROL @Astart;SET("X":455)
4460       CONTROL @Astart;SET("Y":270)
4470       CONTROL @Astart;SET("HEIGHT":22)
4480       CONTROL @Astart;SET("WIDTH":165)
4490       CONTROL @Astart;SET("BORDER":0)
4500       CONTROL @Astart;SET("LABEL":"Start Analysis")
4510       CONTROL @Astart;SET("SENSITIVE":1)
4520       CONTROL @Astart;SET("VISIBLE":1)
4530 ASSIGN @Astop TO WIDGET "TOGGLEBUTTON";PARENT @Mainpanel
4540       CONTROL @Astop;SET("VISIBLE":0)
4550       CONTROL @Astop;SET("X":455)
4560       CONTROL @Astop;SET("Y":297)
4570       CONTROL @Astop;SET("HEIGHT":22)
4580       CONTROL @Astop;SET("WIDTH":165)
4590       CONTROL @Astop;SET("BORDER":0)
4600       CONTROL @Astop;SET("LABEL":"Stop Analysis")
4610       CONTROL @Astop;SET("VALUE":0)
4620       CONTROL @Astop;SET("SENSITIVE":0)
4630       CONTROL @Astop;SET("VISIBLE":1)
4641 ASSIGN @Dstop TO WIDGET "TOGGLEBUTTON";PARENT @Mainpanel
4642       CONTROL @Dstop;SET("VISIBLE":0)
4643       CONTROL @Dstop;SET("X":455)
4644       CONTROL @Dstop;SET("Y":350)
4645       CONTROL @Dstop;SET("HEIGHT":22)
4646       CONTROL @Dstop;SET("WIDTH":165)
4647       CONTROL @Dstop;SET("BORDER":0)
4648       CONTROL @Dstop;SET("LABEL":"Freeze Display")
4649       CONTROL @Dstop;SET("VALUE":0)
4650       CONTROL @Dstop;SET("SENSITIVE":0)
4651       CONTROL @Dstop;SET("VISIBLE":1)
```

```
4652 ASSIGN @Dfile TO WIDGET "PUSHBUTTON";PARENT @Mainpanel
4662      CONTROL @Dfile;SET("VISIBLE":0)
4672      CONTROL @Dfile;SET("X":455)
4682      CONTROL @Dfile;SET("Y":324)
4692      CONTROL @Dfile;SET("HEIGHT":22)
4702      CONTROL @Dfile;SET("WIDTH":165)
4712      CONTROL @Dfile;SET("BORDER":0)
4722      CONTROL @Dfile;SET("LABEL":"Data File")
4732      CONTROL @Dfile;SET("SENSITIVE":1)
4742      CONTROL @Dfile;SET("VISIBLE":1)
4752 !
4762 !
4772 ! 6) Definition of notes
4782 ASSIGN @Notest TO WIDGET "PANEL";PARENT @Mainpanel
4792      CONTROL @Notest;SET("VISIBLE":0)
4802      CONTROL @Notest;SET("X":255)
4812      CONTROL @Notest;SET("Y":415)
4822      CONTROL @Notest;SET("HEIGHT":40)
4832      CONTROL @Notest;SET("WIDTH":360)
4842      CONTROL @Notest;SET("BORDER":1)
4852      CONTROL @Notest;SET("VISIBLE":1)
4862 ASSIGN @Nlabel TO WIDGET "LABEL";PARENT @Mainpanel
4872      CONTROL @Nlabel;SET("VISIBLE":0)
4882      CONTROL @Nlabel;SET("X":265)
4892      CONTROL @Nlabel;SET("Y":405)
4902      CONTROL @Nlabel;SET("HEIGHT":20)
4912      CONTROL @Nlabel;SET("WIDTH":140)
4922      CONTROL @Nlabel;SET("BORDER":0)
4932      CONTROL @Nlabel;SET("VALUE":"Notes or Comments")
4942      CONTROL @Nlabel;SET("JUSTIFICATION":"CENTER")
4952      CONTROL @Nlabel;SET("VISIBLE":1)
4962 !
4972 !
4982 ! 6a) Definition of notes edit boxes
4992 ASSIGN @Notes TO WIDGET "STRING";PARENT @Notest
5002      CONTROL @Notes;SET("VISIBLE":0)
5012      CONTROL @Notes;SET("X":5)
5022      CONTROL @Notes;SET("Y":10)
5032      CONTROL @Notes;SET("HEIGHT":20)
5042      CONTROL @Notes;SET("WIDTH":345)
5052      CONTROL @Notes;SET("BORDER":1)
5062      CONTROL @Notes;SET("VISIBLE":1)
5072 !
5082 ! 7) Definition of Alpha
5092 ASSIGN @Alphaw TO WIDGET "PANEL";PARENT @Mainpanel
5102      CONTROL @Alphaw;SET("VISIBLE":0)
5112      CONTROL @Alphaw;SET("X":255)
5122      CONTROL @Alphaw;SET("Y":370)
5132      CONTROL @Alphaw;SET("HEIGHT":40)
5142      CONTROL @Alphaw;SET("WIDTH":190)
5152      CONTROL @Alphaw;SET("BORDER":1)
5162      CONTROL @Alphaw;SET("VISIBLE":1)
5172 ASSIGN @Alphal TO WIDGET "LABEL";PARENT @Mainpanel
5182      CONTROL @Alphal;SET("VISIBLE":0)
5192      CONTROL @Alphal;SET("X":265)
5202      CONTROL @Alphal;SET("Y":360)
5212      CONTROL @Alphal;SET("HEIGHT":20)
5222      CONTROL @Alphal;SET("WIDTH":60)
5232      CONTROL @Alphal;SET("BORDER":0)
5242      CONTROL @Alphal;SET("VALUE":"Alpha")
5252      CONTROL @Alphal;SET("JUSTIFICATION":"CENTER")
5262      CONTROL @Alphal;SET("VISIBLE":1)
5272 !
5282 !
5292 ! 7a) Definition of alpha edit boxes
5302 ASSIGN @Alphe TO WIDGET "STRING";PARENT @Alphaw
5312      CONTROL @Alphe;SET("VISIBLE":0)
5322      CONTROL @Alphe;SET("X":5)
5332      CONTROL @Alphe;SET("Y":10)
5342      CONTROL @Alphe;SET("HEIGHT":20)
```

```
5352     CONTROL @Alphe;SET("WIDTH":160)
5362     CONTROL @Alphe;SET("BORDER":1)
5372     CONTROL @Alphe;SET("VISIBLE":1)
5382     CONTROL @Alphe;SET("VALUE":".00115")
5392 !
5402 RETURN
5412 !
5422 !-------------------------------------------------------------------
5432 !-------------------------------------------------------------------
5442 !
5452 Constantpower:!
5462   !
5472   !
5482   ! Setup the Keithley
5492   ! ------------------
5502   REMOTE 716
5512   OUTPUT 716;"F1,0X"
5522   OUTPUT 716;"L110,0"
5532   OUTPUT 716;"P0X"                !filter 0
5542   OUTPUT 716;"S1X"                !med. sampling time
5552   OUTPUT 716;"R1X"
5562   OUTPUT 716;"G4,2,0X"
5563   !
5565   !RESET dmm
5566   REMOTE 722
5568   OUTPUT 722;"*RST"
5569   !
5572   ASSIGN @File TO File$;FORMAT ON
5582   !
5592   OUTPUT @File;Notes$
5602   OUTPUT @File;"Start Date and Time "&DATE$(TIMEDATE)&" "&TIME$(TIMEDATE)
5612   OUTPUT @File;"Finsh Date and Time "&DATE$(TIMEDATE+Tim3)&" "&TIME$(TIMEDATE+Tim3)
5622   OUTPUT @File;"P1 inital = "&Lev1$&" W"
5632   OUTPUT @File;"P1 lenght = "&Tim1$
5642   OUTPUT @File;"P1 = P1' * "&Fac1$&" + "&Add1$
5652   OUTPUT @File;"P2 inital = "&Lev2$&" W"
5662   OUTPUT @File;"P2 lenght = "&Tim2$
5672   OUTPUT @File;"P2 = P2' * "&Fac2$&" + "&Add2$
5682   OUTPUT @File;"Data compression senitivity = "&Sen1$&" %"
5692   OUTPUT @File;"Alpha = "&Alpha$&" ohms/'c"
5702   OUTPUT @File;"Room Tempure = "&Rtemp$&" 'c"
5712   OUTPUT @File;"Max power threshold = "&Thres$&" W"
5722   OUTPUT @File;"Total time = "&Tim3$
5732   OUTPUT @File;"Time is seconds",",Set power in Watts",",,Power realized in
Watts",",,,Resistance in ohms",",,,,Tempature",",,,,,Comments"
5742   !
5752   Pset=Lev1
5762   Psetlast=Lev1
5772   IF Fac2=0 THEN
5782      Lev2=Add2
5792   ELSE
5802      Lev2=(Lev2-Plu2)/Fac2
5812   END IF
5813   Psetsign=Pset/ABS(Pset)
5814   Pset=ABS(Pset)
5815   Psetlast=Pset
5816   Psetlastsign=Psetsign
5818   Psetold=Pset
5819   Psetoldsign=Psetsign
5822   !
5832   !----- Determine the initial values
5842   Ipolyinit=.0001
5852   Temp$="B"&VAL$(Ipolyinit)&",0,0"
5862   OUTPUT 716;Temp$
5872   OUTPUT 716;"N1X"
5882   OUTPUT 716;"H0X"
5892   ENTER 716;Meas$
5902   Vpoly=VAL(Meas$)
5912  Rpoly=Vpoly/Ipolyinit
5922  Rpolylast=Rpoly
```

```
5932  Rplot(1)=1
5942  Rpolyroom=Rpoly
5952  !
5962  IF Alph=0. THEN
5972     Ipoly=SQRT(Pset/Rpoly)*Psetsign  !first valid value of Ipoly
5982  ELSE
5992     Atem=((((Rpoly/Rpolyroom)-1)/Alph)+Rtem)
6002     Ipoly=SQRT(Pset/(Rpolyroom*(1+Alph*(Pset*(Atem/(Vpoly*Ipolyinit))-
Rtem))))*Psetsign
6012     Atemold=Atem
6022  END IF
6032  Temp$="B"&VAL$(Ipoly)&",0,0"
6042  !
6052  !
6062  !
6072  !----- Determine the starting time
6082  Newtime=0
6092  Oldtime=0
6102  Savetime=0
6112  Pulsetime=0
6122  Pulse=1
6132  Acount=2
6142  Acountupper=36+1
6152  Runningave=0.
6162  Rsetflag=1
6172  Stopflag=0
6182  Thresflag=0
6192  Timevalue(1)=0
6202  !
6212  IF Tim3/8640<10 THEN
6222     Plotmax=10                    !min 10 for plotmax
6232  ELSE
6242     Plotmax=Tim3/8640
6252  END IF
6262  !
6272  !
6282  Inittime=TIMEDATE
6292  Pulsestart=Inittime
6302  Plottime=Inittime
6303  !
6305  !dmm start value
6306  OUTPUT 722;"MEAS:VOLT:DC?"
6307  ENTER 722;Id
6308  !
6312  OUTPUT @File;Newtime,0,(Ipolyinit*Vpoly),Rpoly,Id,Atem,"Start"
6322  Ipolyold=Ipoly
6332  Vpolyold=Vpoly
6342  Rpolyold=Rpoly
6343  Idold=Id
6352  !
6362  !
6372 Keithleyloop:      !
6382  !
6392  ! Start the Constant Power Loop
6402  ! ----------------------------
6412  !
6422  OUTPUT 716;Temp$
6432  OUTPUT 716;"H0X"
6442  ENTER 716;Meas$
6443  !
6445  !dmm measurement
6446  OUTPUT 722;"MEAS:VOLT:DC?"
6447  ENTER 722;Id
6448  !
6452  Oldtime=Newtime
6462  Newtime=TIMEDATE-Inittime
6472  Pulsetime=TIMEDATE-Pulsestart
6482  Vpoly=VAL(Meas$)
6492  Rpoly=Vpoly/Ipoly
6502  !
```

```
6512  IF Rsetflag=1 THEN
6522     Rsetflag=0
6532     Rinit=Rpoly
6542  END IF
6552  IF ABS(Vpoly*Ipoly)>Thre THEN
6562     OUTPUT @File;Oldtime,Psetlast*Psetlastsign,(Vpolyold*Ipolyold),Rpolyold,Idold
6572     OUTPUT @File;Newtime,Pset*Psetsign,(Vpoly*Ipoly),Rpoly,Id,"Max Power exceeded:
Analysis terminated!"
6582     Thresflag=1
6592     GOTO Thresdone
6602  END IF
6603  !
6617  !
6622  ! Determine if power has changed by user given percent
6623  Sen=Seni/100
6632  IF ABS((Psetlast-Vpoly*Ipoly)/Psetlast)>Sen OR ABS((Rpolylast-Rpoly)/Rpolylast)>Sen
OR ABS((Idold-Id)/Idold)>Sen OR Psetsign<>Psetoldsign THEN
6642     IF NOT (Savetime=Oldtime) THEN
6652        OUTPUT
@File;Oldtime,Psetlast*Psetlastsign,(Vpolyold*Ipolyold)*Psetlastsign,Rpolyold,Idold
6662     END IF
6672     Rpolylast=Rpoly
6682     Savetime=Newtime
6692     Psetlast=Pset
6693     Psetlastsign=Psetsign
6694    !
6696    !REMOTE 722
6697    !OUTPUT 722;"MEAS:VOLT:DC?"
6698    !ENTER 722;Id
6699    !LOCAL 722
6702     OUTPUT @File;Newtime,Pset*Psetsign,(Vpoly*Ipoly)*Psetsign,Rpoly,Id
6712  END IF
6722  !
6732  Rpolyold=Rpoly
6742  Vpolyold=Vpoly
6752  Ipolyold=Ipoly
6762  Idold=Id
6772  !
6782  Ipoly=SQRT(Pset/Rpoly)*Psetsign
6792  IF Pulse=1 AND Pulsetime>Tim1 THEN
6802     Pulse=2
6812     Psetold=Pset
6813     Psetoldsign=Psetsign
6822     Pset=Lev2*Fac2+Plu2
6823     Psetsign=Pset/ABS(Pset)
6824     Pset=ABS(Pset)
6832     IF Pset<.0001 THEN
6842        Pset=.0001
6852     END IF
6862     Lev2=Pset*Psetsign
6872     Pulsestart=TIMEDATE-(Pulsetime-Tim1)
6882     Pulsetime=0
6892     IF Alph=0 THEN
6902        Ipoly=SQRT(Pset/Rpoly)*Psetsign  !first valid value of Ipoly
6912     ELSE
6922        Atem=((((Rpoly/Rpolyroom)-1)/Alph)+Rtem)
6932        Ipoly=SQRT(Pset/(Rpolyroom*(1+Alph*(Pset*(Atem/(Vpoly*Ipolyold))-
Rtem))))*Psetsign
6942        IF ABS((Atemold-Atem)/Atemold)*100>Seni THEN
6952           OUTPUT
@File;Newtime,Psetold*Psetoldsign,(Vpoly*Ipolyold)*Psetoldsign,Rpoly,Id,Atem
6962           Atemold=Atem
6972        END IF
6982     END IF
6992  END IF
7002  IF Pulse=2 AND Pulsetime>Tim2 THEN
7012     Pulse=1
7022     Psetold=Pset
7023     Psetoldsign=Psetsign
7032     Pset=Lev1*Fac1+Plu1
```

```
7033      Psetsign=Pset/ABS(Pset)
7034      Pset=ABS(Pset)
7042      IF Pset<.0001 THEN
7052         Pset=.0001
7062      END IF
7072      Lev1=Pset*Psetsign
7082      Pulsestart=TIMEDATE-(Pulsetime-Tim2)
7092      Pulsetime=0
7102      IF Alph=0 THEN
7112         Ipoly=SQRT(Pset/Rpoly)*Psetsign  !first valid value of Ipoly
7122      ELSE
7132         Atem=((((Rpoly/Rpolyroom)-1)/Alph)+Rtem)
7142         Ipoly=SQRT(Pset/(Rpolyroom*(1+Alph*(Pset*(Atem/(Vpoly*Ipolyold))-
Rtem))))*Psetsign
7152         IF ABS((Atemold-Atem)/Atemold)*100>Seni THEN
7162            OUTPUT
@File;Newtime,Psetold*Psetoldsign,(Vpoly*Ipolyold)*Psetoldsign,Rpoly,Id,Atem
7172            Atemold=Atem
7182         END IF
7192      END IF
7202   END IF
7212   !
7222   Temp$="B"&VAL$(Ipoly)&",0,0"
7232   !
7242   IF TIMEDATE-Plottime>=Plotmax THEN
7252      Plottime=TIMEDATE
7262      Rplot(Acount)=Rpoly/Rinit
7272      Timevalue(Acount)=Newtime
7273      STATUS @Dstop;RETURN("VALUE":Stopdis)
7274      IF Stopdis=0 THEN
7282         CONTROL @Plot;SET("POINT CAPACITY":Acount)
7292         CONTROL @Plot;SET("X DATA":Timevalue(*))
7302         CONTROL @Plot;SET("Y DATA":Rplot(*))
7303      END IF
7312      Runningave=Runningave+Rplot(Acount)
7322      Acount=Acount+1
7332      IF Acount>Acountupper THEN
7342         Rplot(Acount-36)=Runningave/36.
7352         Runningave=0.
7362         Acountupper=Acountupper+1
7372         Acount=Acountupper-36+1
7382      END IF
7392   END IF
7402   STATUS @Astop;RETURN("VALUE":Stopflag)
7412   IF Stopflag=1 THEN
7422      OUTPUT @File;Oldtime,Psetlast,(Vpolyold*Ipolyold),Rpolyold,Idold
7432      OUTPUT @File;Newtime,Pset,(Vpoly*Ipoly),Rpoly,Id,"Analysis terminated by User"
7442      GOTO Thresdone
7452   END IF
7462   IF Newtime>Tim3 THEN
7472      GOTO Keithleydone
7482   END IF
7492   GOTO Keithleyloop
7502   !
7512 Keithleydone: !
7522   OUTPUT @File;Newtime,Pset,(Vpolyold*Ipolyold),Rpolyold,Idold,"end"
7532   !
7542 Thresdone: !
7552   OUTPUT 716;"N0X"
7562 LOCAL 716
7563 LOCAL 722
7582      CONTROL @Plot;SET("POINT CAPACITY":Acount-1)
7592      CONTROL @Plot;SET("X DATA":Timevalue(*))
7602      CONTROL @Plot;SET("Y DATA":Rplot(*))
7603 RETURN
7612 END
```

Appendix C

Automated pressure measurement system program

This is a typical source code to measure the pressure by the input power change when the photodetector output is constrained at a certain value. Different micro-radiator may require different calibration equations for a better accuracy.

```
10 !--------------------------------------------------------------!
20 !--------------------------------------------------------------!
30 REAL Pd,Pd1,R,Ipolyinit,Vpoly,Rpoly,Pinit,P,P1,Ra,Ra1,Pres,Pres1
31 REAL Dif,Ipoly
40 DIM Temp$[50]
45 !Pop-up questions:
50 INPUT "PHOTODETECTOR SIGNAL PD=? (uA)",Pd
60 Pd1=Pd
70 INPUT "READY TO MEASURE PRESSURE?",R$
80 IF R$="N" THEN
90 PRINT "ONCE YOU'RE READY, RUN AGAIN"
100 END IF
110 IF R$="Y" OR R$="" THEN
120 PRINT "PLEASE WAIT ..."
130 END IF
140 !SETUP KEITHLEY AND DMM
150 REMOTE 716
160 OUTPUT 716;"F1,0X"
170 OUTPUT 716;"L110,0"
180 OUTPUT 716;"P0X"
190 OUTPUT 716;"S1X"
200 OUTPUT 716;"R1X"
210 OUTPUT 716;"G4,2,0X"
220 !RESET DMM
230 REMOTE 722
240 OUTPUT 722;"*RST"
250 !Measure room temperature resistance
260 Ipolyinit=.0001
270 Temp$="B"&VAL$(Ipolyinit)&",0,0"
280 OUTPUT 716;Temp$
290 OUTPUT 716;"N1X"
300 OUTPUT 716;"H0X"
310 ENTER 716;Meas$
320 Vpoly=VAL(Meas$)
330 Rpoly=Vpoly/Ipolyinit
335 !Initial heating power
340 Pinit=.005
350 Ipoly=SQRT(Pinit/Rpoly)
360 Temp$="B"&VAL$(Ipoly)&",0,0"
370 OUTPUT 716;Temp$
380 OUTPUT 716;"H0X"
390 ENTER 716;Meas$
400 Vpoly=VAL(Meas$)
410 P=Ipoly*Vpoly
```

```
420 OUTPUT 722;"MEAS:VOLT:DC?"
430 ENTER 722;Ra1
440 Dif=ABS(Ra1+Pd1)
450 Ra=ABS(Ra1)
455 !Check difference, use big step if difference is big
460 IF Dif<=.1 THEN
465 ! Check if getting close to the constant value
470 IF Dif<=.05 THEN
480 P1=P*1000
490 !Pres=-.0843*P1*P1*P1*P1+8.6107*P1*P1*P1-216.99*P1*P1+2143.9*P1-7213
500 IF P1>=33.89 THEN
510 !Pres1=.0014*P1*P1*P1*P1*P1*P1-
.1942*P1*P1*P1*P1*P1+10.772*P1*P1*P1*P1
520 !Pres=Pres1-298.94*P1*P1*P1+4319.6*P1*P1-30304*P1+80195
531 Pres=-.0843*P1*P1*P1*P1+8.6107*P1*P1*P1-216.99*P1*P1+2143.9*P1-7213
532 GOTO 572
534 END IF
542 IF P1<33.89 THEN
552 Pres=.0143*P1*P1*P1*P1-.4553*P1*P1*P1+7.858*P1*P1-31.748*P1-21.043
562 END IF
572 PRINT "POWER=",P1
582 PRINT "PRESSRE=",Pres
592 GOTO 802
602 END IF
612 IF Ra>Pd1 THEN
622 Ipoly=Ipoly-1.E-6
632 GOTO 360
642 END IF
652 IF Ra<Pd1 THEN
662 Ipoly=Ipoly+1.E-6
672 GOTO 360
682 END IF
692 END IF
702 IF Dif>.1 THEN
712 IF Ra>Pd1 THEN
722 Ipoly=Ipoly-1.E-5
732 GOTO 360
742 END IF
752 IF Ra<Pd1 THEN
762 Ipoly=Ipoly+1.E-5
772 GOTO 360
782 END IF
792 END IF
802 OUTPUT 716;"N0X"
810 ! reset SMU and DMM
812 LOCAL 716
822 LOCAL 722
832 END
```

Appendix D

ANSYS Input File

This is the input file for building the numerical model in ANSYS to simulate the temperature profile of micro-radiator. The data are directly extracted from L-Edit.

```
/title, CMOS Micro-radiator
/units, si
/prep7
!
k,1,147.50, 160.00
k,2, 159.00, 160.00
k,3, 159.00, 150.00
k,4, 152.50, 150.00
k,5, 61.00, 60.00
k,6, 61.00, 70.00
k,7, 67.50, 70.00
k,8, 72.50, 60.00
k,9, 142.50, 65.00
k,10, 147.50, 65.00
k,11, 137.50, 60.00
k,12, 152.50, 60.00
k,13, 122.50, 65.00
k,14, 127.50, 65.00
k,15, 117.50, 60.00
k,16, 132.50, 60.00
k,17, 102.50, 65.00
k,18, 107.50, 65.00
k,19, 97.50,60.00
k,20, 112.50, 60.00
k,21, 82.50, 65.00
k,22, 87.50, 65.00
k,23, 77.50, 60.00
k,24, 92.50, 60.00
k,25, 127.50, 160.00
k,26, 142.50, 160.00
k,27, 132.50, 155.00
k,28, 137.50, 155.00
k,29,107.50, 160.00
k,30, 122.50, 160.00
k,31, 112.50, 155.00
k,32, 117.50, 155.00
k,33, 87.50, 160.00
k,34, 102.50, 160.00
k,35, 92.50, 155.00
k,36, 97.50, 155.00
k,37,67.50, 160.00
```

```
k,38, 82.50, 160.00
k,39, 72.50, 155.00
k,40, 77.50, 155.00
k,41, 50.00, 170.00
k,42, 155.00, 170.00
k,43, 208.00, 220.00
k,44,  0.00,  0.00
k,46,  0.00, 12.00
k,47, 50.00, 65.00
k,48, 220.00, 220.00
k,50, 170.00, 155.00
k,51, 220.00, 202.00
k,52, 170.00, 50.00
k,53, 65.00, 50.00
k,54, 18.00,  0.00
k,55, 147.50, 165.00
k,56, 156.50, 165.00
k,57, 72.50, 55.00
k,58, 63.50, 55.00
k,59, 220.00, 211.00
k,60, 214.00, 220.00
k,61,  9.00,  0.00
k,62,  0.00,  6.00
k,63, 0.0, 220.0
k,64,220.0,0.0
!
l,1, 2
l, 3, 2
l, 4, 3
l, 5, 6
l, 6, 7
l, 5, 8
l, 9, 10
l, 11, 12
l, 13, 14
l, 15, 16
l, 17, 18
l, 19, 20
l, 21, 22
l, 23, 24
l, 25, 26
l,27, 28
l,29, 30
l,31, 32
l,33, 34
l,35, 36
l,37, 38
l,39, 40
l,10, 1
l,12, 4
```

```
l,19, 36
l,17, 34
l,23, 40
l,21, 38
l,18, 29
l,20, 31
l,14, 25
l,16, 27
l,15, 32
l,13, 30
l,11, 28
l,9, 26
l,22, 33
l,24, 35
l,7, 37
l,8, 39
l,41, 42
l,42, 43
l,46, 47
l,47, 41
l,50, 51
l,52, 50
l,53, 52
l,54, 53
l,1,55
l,55, 56
l,57, 8
l,58, 57
l,3,59
l,56, 60
l,61, 58
l,62, 6
l,44,61
l,61,54
l,44,62
l,62,46
l,48,60
l,60,43
l,48,59
l,59,51
!
a, 1, 2, 3, 4, 12, 11, 28, 27, 16, 15, 32, 30, 13, 14, 25, 26, 9, 10
a, 30, 32, 31, 20, 19, 36, 35, 24, 23, 40, 38, 21, 22, 33, 34, 17, 18, 29
a, 38, 40, 39, 8, 5, 6, 7, 37
a, 44, 61, 58, 57, 8, 5, 6, 62
a, 48, 59, 3, 2, 1, 55, 56, 60
a, 62, 46, 47, 41, 42, 43, 60, 56, 55, 1, 10, 9, 26, 37, 7, 6
a, 25, 14, 13, 30
a, 29, 18, 17, 34
a, 33, 22, 21, 38
```

```
a, 61, 54, 53, 52, 50, 51, 59, 3, 4, 12, 11, 28, 27, 16, 8, 57, 58
a, 15, 32, 31, 20
a, 19, 36, 35, 24
a, 23, 40, 39, 8
a, 63,46,47,41,42,43
a,54,53,52,50,51,64
!
aadd, 1, 2, 3
aadd, 6, 7, 8, 9
aadd, 10, 11, 12, 13
aglue, all
!
MP, KXX, 1, 34
MP, DENS, 1, 2320
MP, C, 1, 700
!
MP, KXX, 2, 1.4
MP, DENS, 2, 2190
MP, C, 2, 1400
!
MP, KXX, 3, 237
MP, DENS, 3, 2700
MP, C, 3, 896
!
MP,KXX,4,0.025
MP,DENS,4,1.21
MP,C,4,1010
!
/eof
```